

Doctoral Dissertation (Censored)
博士論文 (要約)

Phase space structure in the Milky Way disc
(天の川銀河円盤の位相空間構造)

A Dissertation Submitted for the Degree of Doctor of Philosophy
December 2023
令和5年12月博士(理学)申請

Department of Astronomy, Graduate School of Science
The University of Tokyo
東京大学大学院理学系研究科天文学専攻

Tetsuro Asano
朝野 哲郎

ABSTRACT

The astrometry data from the European Space Agency’s *Gaia* mission revealed the detailed phase-space distribution of the stars in the Milky Way (MW) disc. The phase space maps of disc stars exhibit a wealth of substructures, which are considered to be related to the bar, spiral arms and external perturbations due to dwarf galaxies, but their exact origins are still in debate. In this thesis, we comprehensively investigate the relations between the phase-space substructures and internal and external perturbations on the MW disc using high-resolution N -body simulations. From the comparison between the phase-space maps in the N -body models and those in the *Gaia* data, we investigate the dynamical structure of the MW disc and its time evolution.

In Chapter 3, we focus on the velocity-space substructures such as the Hercules stream. We analyse an N -body simulation of an isolated MW-like barred spiral galaxy performed by Fujii et al. (2019). In the final snapshot of the simulation, we find a Hercules-like stream at $(R, \phi) = (8 \text{ kpc}, 20^\circ)$, where R and ϕ are the distance from the galactic centre and the angle with respect to the bar’s major axis, respectively. From our orbital frequency analysis, we identify multiple, especially higher-order resonances. Our results suggest that the Hercules stream is dominated by the 4:1 and 5:1 outer Lindblad and corotation resonances of the bar. A combination of such resonances forms the trimodal structure of the Hercules stream. From the relation between resonances and ridges in R - v_ϕ space, our model favoured a slow pattern speed of the MW bar ($40\text{--}45 \text{ km s}^{-1} \text{ kpc}^{-1}$).

In Chapter 4, we focus on the time evolution and spatial variation of the velocity-space distribution. We quantitatively evaluate the similarities of the velocity-space distributions in the N -body model and that of the solar neighbourhood, using Kullback-Leibler divergence (KLD), an indicator to measure the similarity between two distributions. The KLD oscillates with time, which indicates the velocity-space distribution at a fixed position is not always similar to that of the solar neighbourhood. Some locations in the simulated galactic disc show velocity-space distributions with small KLDs (high similarities) more frequently than others. One of them is located at $(R, \phi) = (8.2 \text{ kpc}, 30^\circ)$, which is similar to the observationally estimated position of the Sun in the MW disc. The detection frequency is higher in the inter-arm regions than in the arm regions because spiral arms disturb the velocity-space substructures due to the bar resonances. In the velocity maps with small KLDs, we identify the velocity-space substructures, which consist of particles trapped in bar resonances.

In Chapter 5, we investigate the breathing motion of the MW disc. Theoretical models of spiral arms suggest that the spiral arms provoke a vertical bulk motion in disc stars. By analysing the breathing motion, a coherent asymmetric vertical motion around the mid-plane of the MW disc, with the *Gaia* data, we find that a compressing breathing motion presents along the Local arm. On the other hand, with the isolated N -body model, we find that the transient and dynamic spiral arms induce compressing breathing motions when the arms are in the growth phase. The observed clear alignment of the compressing breathing motion with the Local arm is similar to what is seen in the growth phase of the simulated spiral arms. Hence, this result suggests that the Local arm’s compressing breathing motion can be explained by the Local arm being in the growth phase of a transient and dynamic spiral arm.

In Chapter 6, we analyse a newly performed N -body simulation of a MW-like disc galaxy perturbed by a Sagittarius dwarf-like satellite. The external perturbation by the dwarf galaxy causes two structural changes in the galactic disc: bending oscillation and tidally induced spiral arms. Both of them form characteristic substructures in the phase-space distribution of the disc particles. In the vertical position (z) versus vertical velocity (v_z) space, we observe one-arm and two-arm phase spirals associated with the bending and breathing oscillations, respectively. The Fourier and spectral analysis reveals that the bending mode is directly excited by the dwarf’s external perturbation, whereas the breathing mode is excited by tidally induced spiral arms. The bending mode decays more rapidly than the breathing mode, and the decay time scale of the bending mode increases with R , whereas that of the breathing mode exhibits weaker dependence on R . This difference in decay time scales results in the transition of the dominant mode from the bending mode to the breathing mode, and the transition of the dominant mode propagates from the inner galaxy to the outer galaxy.

The distribution of disc stars in the 6D phase space results from various perturbations, forming a complex structure that is challenging to understand comprehensively. Nevertheless, each perturbation

forms substructures with characteristic geometries and scales, allowing us to study them individually by extracting lower-dimensional spaces. This thesis focuses on the local velocity space, the breathing map and the vertical position versus vertical velocity map. By comparing these phase space maps in the *Gaia* data and those in the N -body simulations, we provide physical insights into the dynamical properties of the bar, spiral arms and external perturbations.

ACKNOWLEDGEMENTS

I would like to express my deepest gratitude to my supervisor, Michiko Fujii, for her support throughout my graduate studies and research journey. Her guidance, encouragement and patience have been invaluable to me. It is a great honour for me to be recognised as the first student to receive a PhD under her supervision here at the University of Tokyo.

My heartfelt thanks to my co-authors and collaborators, Junichi Baba, Simon Portegies Zwart, Jeroen Bédorf, Elena Sellentin, Daisuke Kawata and Victor Debattista. Their insightful comments and suggestions have significantly enriched this work. I am also particularly grateful for the discussions I held with many individuals, especially Kohei Hattori, Pau Ramos, Teresa Antoja, Rimpei Chiba, Eugene Vasiliev and Junichiro Makino, which have greatly enhanced my research.

I would like to thank my thesis committee members Fumi Egusa, Eiichiro Kokubo, Mamoru Doi, Masashi Chiba and Naoteru Gouda for their valuable comments and suggestions.

My time spent at Hongo was enriched by my colleagues and friends. I would like to thank the current and former members of the Department of Astronomy, especially Rikako Ishimoto, Keiya Hirashima, Makoto Ando, Daisuke Taniguchi, Naoto Yoshinari and Junya Arita, who had many scientific and non-scientific discussions with me.

My journey in astronomy and astrophysics began at the Astronomical Institute of Tohoku University. I am grateful to all the professors at the Institute, with special thanks to Tadayuki Kodama and Masafumi Noguchi, for teaching me the basics of galactic astronomy and galactic dynamics.

My stay at the Leiden Observatory was enhanced by interacting with many remarkable individuals who helped make my four months in Leiden both fruitful and enjoyable. I am particularly indebted to Simon Portegies Zwart, Martijn Wilhelm, Shuo Huang, Veronica Saz Ulibarrena, Anthony Brown, Koen Kuijken, Takayuki Muto and Jinyi Liu.

I would like to express my sincere appreciation for the support I received from the Japan Society for the Promotion of Science (JSPS) Research Fellowships for Young Scientists, the JSPS Overseas Challenge Program for Young Researchers and The University of Tokyo International Graduate Program for Excellence in Earth-Space Science. The financial backing provided by the Grant-in-Aid for JSPS Fellows (Number JP22J11943) significantly contributed to the successful completion of this work.

This research used computational resources of Cygnus and HA-PACS provided by Multidisciplinary Cooperative Research Program in Center for Computational Sciences, University of Tsukuba, Piz Daint at the Swiss National Supercomputing Centre and Little Green Machine II. In this research work, we used the “mdx: a platform for building data-empowered society”.

This work has made use of data from the European Space Agency (ESA) mission *Gaia* (<https://www.cosmos.esa.int/gaia>), processed by the *Gaia* Data Processing and Analysis Consortium (DPAC, <https://www.cosmos.esa.int/web/gaia/dpac/consortium>). Funding for the DPAC has been provided by national institutions, in particular the institutions participating in the *Gaia* Multilateral Agreement.

The English of the acknowledgements and some paragraphs in the main part of the thesis were polished by DeepL and ChatGPT.

This thesis was typeset using the typographical look-and-feel CLASSICTHESIS (<https://bitbucket.org/amiede/classicthesis/>) developed by André Miede and Ivo Pletikosić.

Most of my research code, papers and this thesis, were written using the vim text editor. In this regard, I must express my gratitude to the late Bram Moolenaar (1961—2023) for his lifelong commitment to the development of this superior text editor.

PUBLICATIONS

This thesis has used the materials of the following publications.

- Chapter 3 is based on [Asano et al. \(2020\)](#), “Trimodal structure of Hercules stream explained by originating from bar resonances”, *Monthly Notices of the Royal Astronomical Society (MNRAS)* 499, 2416.
- Chapter 4 is based on [Asano et al. \(2022\)](#), “Impact of bar resonances in the velocity-space distribution of the solar neighbourhood stars in a self-consistent N-body Galactic disc simulation”, *MNRAS* 514, 460.
- Chapter 5 is based on [Asano et al. \(2024\)](#), “Growing Local arm inferred by the breathing motion”, *MNRAS Letters* 529, L7.

CONTENTS

I THESIS

1	INTRODUCTION	3
1.1	Structure of the Milky Way	3
1.1.1	Milky Way as a disc galaxy	3
1.1.2	Rotation curve and dark matter halo	5
1.1.3	Bulge/bar	7
1.1.4	Spiral arms	8
1.1.5	Other components	9
1.2	Space astrometry	11
1.3	Theoretical backgrounds	13
1.3.1	Angle-action variables	13
1.3.2	Resonances	15
1.4	Phase space structures of the disc stars	17
1.4.1	Velocity-space substructures	19
1.4.2	The phase spiral	20
1.5	Theoretical and numerical modelling of galaxies	26
1.6	This thesis	27
1.6.1	Objective of this thesis	27
1.6.2	Structure of this thesis	27
2	<i>N</i> -BODY SIMULATIONS AND GAIA DATA	29
2.1	Isolated model	29
2.1.1	Initial condition and simulation	29
2.1.2	Structures of the disc and bulge	30
2.2	Perturbed model	34
2.3	Gaia data	34
3	HERCULES STREAM	37
3.1	Introduction	37
3.2	<i>N</i> -body model	38
3.2.1	Distribution of simulated stars in velocity space	39
3.2.2	Orbit analysis and identification of resonantly trapped stars	40
3.3	Results for Gaia	44
3.3.1	The origin of the Hercules stream from resonances	44
3.3.2	The Milky Way's bar pattern speed	46
3.4	Summary	48
4	TIME EVOLUTION AND SPATIAL VARIATION OF THE VELOCITY-SPACE SUBSTRUCTURES	49
4.1	Introduction	49
4.2	Data and analysis	49
4.2.1	<i>N</i> -body model	49
4.2.2	Analysis of the <i>Gaia</i> data	49
4.2.3	Kullback-Leibler divergence	49
4.3	Results	50
4.3.1	Time evolution of the KLDs	50
4.3.2	Angle with respect to the bar and spirals	51
4.4	Discussions	56
4.5	Summary	58
5	GROWING LOCAL ARM INFERRED BY THE BREATHING MOTION	61
5.1	Introduction	61
5.2	The breathing motion in the Milky Way disc	61
5.3	Breathing motion in an <i>N</i> -body simulation	63
5.3.1	Breathing motion in an <i>N</i> -body simulation	63
5.3.2	Time evolution of spiral arms and breathing mode	65

5.4	Discussion and Conclusion	65
6	BENDING AND BREATHING MOTIONS OF THE GALACTIC DISC INDUCED BY DWARF GALAXIES	67
7	SUMMARY AND CONCLUSIONS	69
7.1	Summary	69
7.2	The Future	70
7.2.1	Combined effects of the internal and external perturbations	70
7.2.2	NIR astrometry surveys	71
7.2.3	Chemodynamica of the Milky Way disc	71
 II APPENDICES		
A	ISOLATED MILKY WAY MODELS IN FUJII ET AL. (2019)	75
B	SHAPES OF THE RESONANTLY TRAPPED ORBITS	79
C	LOCATION OF SPIRAL ARM	85
c.1	Azimuths of spiral arms	85
c.2	Radii of spiral arms	85
D	SELECTION EFFECTS ON THE BREATHING MOTION	89

LIST OF FIGURES

Figure 1.1	Optical image of the MW obtained by the <i>Gaia</i> satellite	4
Figure 1.2	Herschel’s MW map	5
Figure 1.3	Oort (1958)’s MW map traced by the 21-cm line	6
Figure 1.4	Rotation curve of the MW	7
Figure 1.5	Infrared image of the MW obtained by the <i>COBE</i> satellite	8
Figure 1.6	Spiral arms of the MW	9
Figure 1.7	Artists’ concepts of the MW	10
Figure 1.8	Spatial coverage of the <i>Hipparcos</i> data	12
Figure 1.9	Spatial coverage of the <i>Gaia</i> DR3 astrometric sample	14
Figure 1.10	Spatial coverage of the <i>Gaia</i> DR3 radial velocity sample	14
Figure 1.11	Mapping from action space to velocity space	16
Figure 1.12	The orbital frequencies as functions of the galactocentric radius	17
Figure 1.13	Velocity-space distribution of the solar neighbourhood stars	18
Figure 1.14	Velocity-space distribution in an axisymmetric model	18
Figure 1.15	Velocity map from the <i>Hipparcos</i> data	19
Figure 1.16	Velocity-space distribution in a barred galaxy model	20
Figure 1.17	The phase spiral in the <i>Gaia</i> DR3 data	21
Figure 1.18	Schematic illustration of phase mixing	22
Figure 1.19	Phase spiral for the <i>Gaia</i> DR3 sample split by R_g and θ_ϕ	23
Figure 1.20	Schematic illustration of the bending motion	24
Figure 1.21	Schematic illustration of the breathing motion	25
Figure 2.1	Time evolution of the disc structure in the isolated model	31
Figure 2.2	The rotation curves of the N -body model and the MW	32
Figure 2.3	Time evolution of the bar pattern speed and bar amplitude	33
Figure 3.1	Radial and angular velocity-space distribution of stars within 0.2 kpc from the Sun	38
Figure 3.2	2D-histogram in v_R versus v_ϕ space at various positions in the disc at 10 Gyr	39
Figure 3.3	Distribution of simulation particles in velocity space around $(R, \phi) = (8 \text{ kpc}, 20^\circ)$	40
Figure 3.4	Orbital frequency ratios for the particles within 0.2 kpc from $(R, \phi) = (8 \text{ kpc}, 20^\circ)$	41
Figure 3.5	Examples of the orbits trapped in the bar resonances	43
Figure 3.6	Resonantly trapped orbits in a single frame	44
Figure 3.7	Resonantly trapped particles in velocity space	45
Figure 3.8	The orbital frequencies as functions of the galactocentric radius R	46
Figure 3.9	Phase-space structures in the R versus v_ϕ space	47
Figure 4.1	Face-on view of the galactic disc	50
Figure 4.2	Time evolution of the bar’s pattern speed and amplitude	51
Figure 4.3	Time evolution of the KLD	52
Figure 4.4	Histogram of the KLD in the snapshot at $t = 10 \text{ Gyr}$	53
Figure 4.5	Positions where the velocity maps match that of the solar neighbourhood	54
Figure 4.6	Histograms of the angles where the KLD of velocity distribution is less than 0.2	54
Figure 4.7	Histograms of the angles where the KLD of velocity distribution is less than 0.2 (Dependence on the spiral amplitude)	55
Figure 4.8	Same as Fig. 4.7 but now for the angle with respect to the spirals $(\phi - \phi_2)$	56
Figure 4.9	Velocity-space distribution for the particles within 200 pc from $(R, \phi) = (8 \text{ kpc}, 15^\circ)$ at $t = 9.29 \text{ Gyr}$	57
Figure 4.10	Same as Fig. 4.9 but for the particles within 200 pc from $(R, \phi) = (8.5 \text{ kpc}, 50^\circ)$ at $t = 8.97 \text{ Gyr}$	58
Figure 4.11	Residual maps of the simulated and observed \hat{v}_R - \hat{v}_ϕ space distributions	59
Figure 5.1	Face-on breathing map from the <i>Gaia</i> data	62
Figure 5.2	Face-on breathing map from the N -body model	63
Figure 5.3	Time evolution of a spiral arm and the associated breathing motion	64
Figure A.1	Disc and bulge properties of MWa5B and comparison with observations	76

Figure A.2	Same as Fig. A.1 but for MWb6B.	77
Figure A.3	Same as Fig. A.1 but for MWc7B.	77
Figure B.1	Orbital shapes of the particles trapped in the 2:1 OLR	80
Figure B.2	Same as Fig. B.1 but for the 3:1 OLR.	81
Figure B.3	Same as Fig. B.1 but for the 4:1 OLR.	82
Figure B.4	Same as Fig. B.1 but for the 5:1 OLR.	83
Figure C.1	Phase angles of the Fourier decomposition for the disc surface density	86
Figure C.2	Definition of the arm and inter-arm radii	87
Figure D.1	Selection function for the <i>Gaia</i> DR3 radial velocity sample at $60^\circ \leq l \leq 75^\circ$	89
Figure D.2	Face-on maps of the breathing velocity for the particles at $ z > 0.1, 0.2, 0.3$ and 0.4 kpc	90

LIST OF TABLES

Table 1.1	Comparison between the <i>Hipparcos</i> and <i>Gaia</i> catalogues.	13
Table 2.1	Initial condition parameters for the isolated model	30
Table 2.2	Assumed parameters for the solar position and motion	35
Table A.1	Initial condition parameters for the MW models	75
Table A.2	χ^2 for Σ , σ_R , K_z , v_{los} and σ_{los}	76

LISTINGS

Listing 2.1	ADQL query to select the <i>Gaia</i> DR3 samples with high quality astrometric solutions and small parallax errors.	34
-------------	---	----

ACRONYMS

ADQL	Astronomical Data Query Language
BP	boxy/peanut
BP/RP	Blue and Red Photometers
BRAVA	Bulge Radial Velocity Assay
COBE	Cosmic Background Explorer
CR	corotation resonance
DF	distribution function
DFT	discrete Fourier transform
DM	dark matter
DR	Data Release
DR1	<i>Gaia</i> Data Release 1
DR2	<i>Gaia</i> Data Release 2
EDR3	<i>Gaia</i> Early Data Release 3
DR3	<i>Gaia</i> Data Release 3
ESA	European Space Agency

GLIMPSE	Galactic Legacy Infrared Midplane Survey Extraordinaire
GPU	graphics processing unit
GRAPE	GRAvity Pipe
ILR	inner Lindblad resonance
IR	infrared
<i>JASMINE</i>	Japan Astrometry Satellite Mission for INfrared Exploration
KLD	Kullback-Leibler divergence
LMC	Large Magellanic Cloud
LSR	local standard of rest
MW	Milky Way
M2M	Made-to-Measure
NIR	near-infrared
OLR	outer Lindblad resonance
PFS	Prime Focus Spectrograph
RGB	red giant branch
RVS	Radial-Velocity Spectrometer
SCF	self-consistent field
SMC	Small Magellanic Cloud
VLBI	very long base-line interferometry
2MASS	Two Micron All Sky Survey

Part I

THESIS

INTRODUCTION

1.1 STRUCTURE OF THE MILKY WAY

1.1.1 *Milky Way as a disc galaxy*

The Milky Way (MW) has fascinated us throughout human history. Fig. 1.1 displays an all-sky image of the MW obtained by the *Gaia* satellite. It is a portrait of our home galaxy as seen from the solar system. Although we cannot observe our galaxy from the outside, we know that it is a barred spiral galaxy. This section provides a brief history of our understanding of the MW's structure and summarises our current knowledge. Throughout this section, we refer to the following books and papers: Binney & Merrifield (1998), Binney & Tremaine (2008), Bland-Hawthorn & Gerhard (2016), Sofue (2017a), Sofue et al. (2018) and van der Kruit (2019).

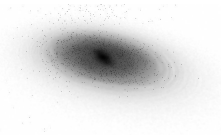
William Herschel was a pioneer in mapping the MW based on scientific observations and measurements (Herschel 1785). He estimated the shape of the MW by counting the number of stars at over 600 different directions in the sky assisted by his sister Caroline. The number count is proportional to D^3 , where D is the distance to the edge. This estimation relied on the following assumptions: (1) stars are uniformly distributed in the MW, (2) all stars have the same intrinsic luminosity and (3) the telescope is powerful enough to see through the MW to its edge. Fig. 1.2 presents the estimated map of the MW, which corresponds to the edge-on slice of the MW disc. The large star near the centre of the map indicates the position of the Sun. It is surprising that Herschel could estimate the flat disc-like shape of the MW with such a simple method and rough assumptions although he mapped the Sun at the wrong place.

Jacobus Kapteyn used a method similar to that of Herschel but more sophisticated one (Kapteyn 1922) to make the map of the MW.¹ His MW model is represented by a ellipsoid whose radius and axis ratios are ~ 8 kpc and 5:1, respectively. Although the size is smaller than the actual size of the MW, the model successfully reproduces the trend that the density of stars decreases from the inner to the outer Galaxy. The MW map generated by Kapteyn more closely resembles the modern understanding of the MW's structure compared to Herschel's, but like Herschel, he positioned the Sun near the Galactic centre.

Harlow Shapley studied the distribution of globular clusters (e.g. Shapley 1918a,b). He discovered that the globular clusters are not uniformly distributed in the sky and biased in the direction of the constellation of Sagittarius. The findings led him to the conclusion that the biased distribution is a result of the Sun being situated away from the Galactic centre. He also measured their distances using the period-luminosity relation of Cepheid variables discovered by Henrietta Leavitt (Leavitt & Pickering 1912). To explain this distribution, he proposed a model where the diameter of the MW's disc is 100 kpc, with the Sun positioned at a distance of 15 kpc from the Galactic centre. Shapley proposed a large MW model whereas Kapteyn proposed a small MW model. Both of their estimated sizes differ from the actual size of the MW due to difficulties in properly accounting for dust extinction. Later observations overcame this difficulty.

Bertil Lindblad and Jan Oort made significant contributions to our understanding of the structure of the MW through the analysis of the stellar kinematics. Lindblad measured line-of-sight velocities of globular clusters using the Doppler shifts of spectral lines. He found that the velocities were higher than the escape velocity predicted by Kapteyn's model, suggesting that the MW is larger and more massive than Kapteyn's model and more consistent with Shapley's model. He tried to model the MW in terms of stellar kinematics. Lindblad (1927) proposed the concept that the MW comprises an infinite number of subsystems. They can be roughly categorized into two classes. The first class exhibits almost no systematic rotation about the Galactic centre and has a spherical distribution supported by random motion. This class includes globular clusters. The second class forms a rotationally supported, flat, disc-like system. Most of the solar neighbourhood stars have small velocities with respect to the Sun. Lindblad inferred that these stars follow nearly circular orbits around the Galactic centre and have a flat disc distribution.

¹ Kapteyn's MW map is often referred to as the Kapteyn Universe because the conception that the MW is one of the galaxies distributed in the Universe was not established and the MW was thought to be the entire Universe when Kapteyn made the map.



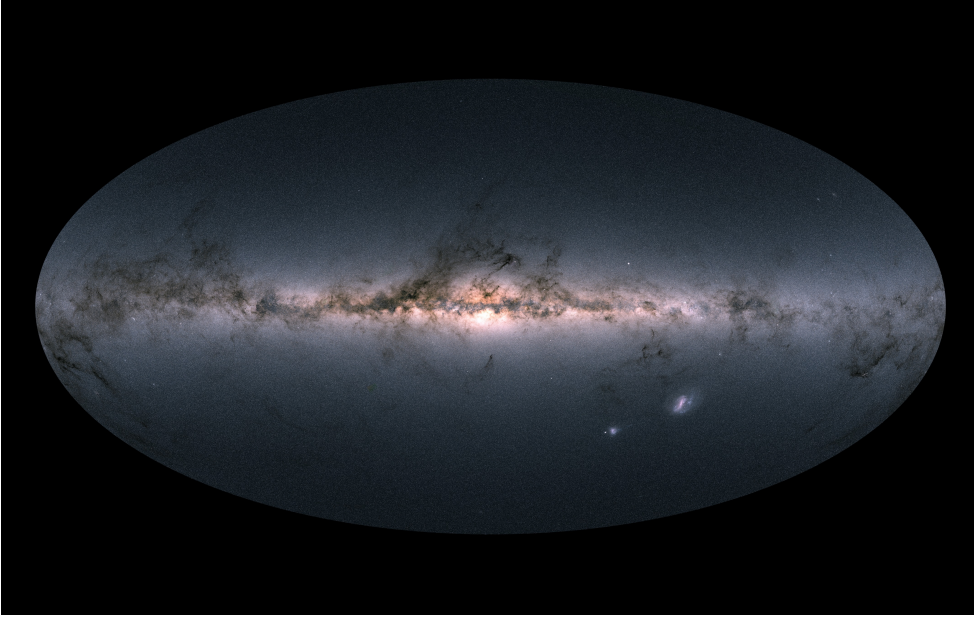


Figure 1.1: Optical image of the MW obtained by the *Gaia* satellite. Credit: ESA/Gaia/DPAC.

By measuring their velocities relative to the mean motion of globular clusters, he estimated the circular velocity at the solar radius to be in the range of $200\text{--}300\text{ km s}^{-1}$.

Building upon Lindblad's work, [Oort \(1927, 1928\)](#) further developed the theory of the Galaxy rotation and derived a method to observationally estimate the dynamical parameters of the [MW](#). We define two functions of the Galactocentric radius R :

$$A(R) \equiv \frac{1}{2} \left(\frac{v_c}{R} - \frac{dv_c}{dR} \right) = -\frac{1}{2} R \frac{d\Omega}{dR}, \quad (1.1a)$$

$$B(R) \equiv -\frac{1}{2} \left(\frac{v_c}{R} + \frac{dv_c}{dR} \right) = -\left(\Omega + \frac{1}{2} R \frac{d\Omega}{dR} \right), \quad (1.1b)$$

where $v_c(R)$ and $\Omega(R) = v_c(R)/R$ are the circular velocity and frequency, respectively. The values of A and B at the solar radius R_0 are called the Oort constants and can be measured observationally. When we observe a star with a circular orbit at R , its line-of-sight and tangential velocities relative to the local standard of rest ([LSR](#)) can be written as:

$$v_{\text{los}} = [\Omega(R) - \Omega(R_0)] R_0 \sin l, \quad (1.2a)$$

$$v_t = [\Omega(R) - \Omega(R_0)] R_0 \cos l - \Omega(R) d, \quad (1.2b)$$

where l and d are the star's Galactic longitude and distance from the Sun, respectively. Here we assume d is sufficiently smaller than R and R_0 . See Fig. 4.7 in [Sofue \(2017a\)](#) for the geometric interpretation of the equations. Expanding Equations (1.2) to the first order in $R - R_0$, they may be written

$$v_{\text{los}} \simeq \left. \frac{d\Omega}{dR} \right|_{R_0} (R - R_0) R_0 \sin l \simeq A d \sin 2l, \quad (1.3a)$$

$$v_t \simeq \left. \frac{d\Omega}{dR} \right|_{R_0} (R - R_0) R_0 \cos l - \Omega(R_0) d \simeq A(\cos 2l + B) d. \quad (1.3b)$$

The conversion from the second to third terms is facilitated by the approximation of $R - R_0 \simeq -d \cos l$. We can estimate the Oort constants by measuring the line-of-sight velocities and proper motions of the solar neighbourhood stars. The Oort constants are related to the circular frequency and the epicycle frequency by

$$\Omega(R_0) = \frac{v_c(R_0)}{R_0} = A - B, \quad (1.4)$$

$$\kappa^2(R_0) = -4B(A - B). \quad (1.5)$$

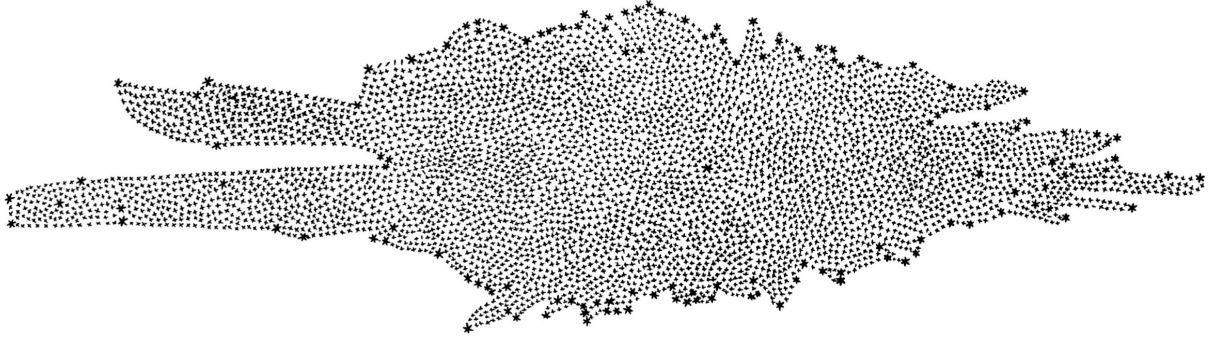


Figure 1.2: Herschel's [MW](#) map. The large star near the centre of the map indicates the position of the Sun. This figure is made from a copy of [Herschel \(1785\)](#) available at <https://www.jstor.org/stable/106755>.

Analysing the motion of solar neighbourhood stars, [Oort \(1927, 1928\)](#) obtained the values of $(A, B) = (19, -24) \text{ km s}^{-1} \text{ kpc}^{-1}$ ([van der Kruit 2019](#)). They lead to $\Omega(R_0) \sim 43 \text{ km s}^{-1} \text{ kpc}^{-1}$ and $\kappa(R_0)/\Omega(R_0) \sim 1.5$, indicating that the [MW](#) exhibits differential rotation.² A recent estimation of the Oort constants based on the *Gaia* data are $(A, B) = (15.3, -11.9) \text{ km s}^{-1} \text{ kpc}^{-1}$ ([Bovy 2017](#)). If the circular velocity is independently given, we can derive R_0 from the Equation (1.4). [Oort \(1927\)](#) obtained the value of $R_0 = 6.3 \pm 2 \text{ kpc}$, by assuming $v_c(R_0) = 272 \text{ km s}^{-1}$, which was derived from the analysis of the high-velocity (with respect to the Sun) stars.

One reason why both Kapteyn and Shapley obtained incorrect [MW](#) images is that they did not properly account for dust extinction. Radio observations are more useful than optical observations for mapping the [MW](#) over a wide range, as radiation at the radio wavelengths is less affected by the dust extinction. Oort significantly contributed to radio astronomy as well. He promoted a project aimed at detecting the 21-cm emission lines from H I (neutral atomic hydrogen) gas predicted by Hendrik van de Hulst. The 21-cm line is useful not only because they are almost unaffected by the dust but also because the line-of-sight velocity can be measured by the Doppler shift, so we can simultaneously obtain the density and kinematic information. The prediction was finally confirmed by [Christiansen & Hindman \(1951\)](#), [Ewen & Purcell \(1951\)](#) and [Muller & Oort \(1951\)](#). [Oort et al. \(1958\)](#) completed the H I map of the [MW](#). Fig. 1.3 shows the distribution of the H I gas in the [MW](#) disc obtained by [Oort et al. \(1958\)](#). It reveals a flat gas disc extending to large radii. Another notable feature in this figure is the spiral structure traced by the narrow dense gas regions.

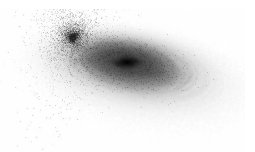
1.1.2 Rotation curve and dark matter halo

The H I and also CO emission lines are used to make the rotation curve of the [MW](#). Within the solar radius, the rotation curve can be obtained with the terminal velocity method. We obtain the maximum

² Epicycle frequency κ and the circular frequency are related by

$$\kappa^2 = R \frac{d\Omega^2}{dR} + 4\Omega^2.$$

The ratio of these two frequencies is within the range of $1 \leq \kappa/\Omega \leq 2$, where the lower and upper boundaries correspond to a Kepler motion and a rigid rotation (harmonic oscillator), respectively. In the case of flat rotation curves, $\kappa/\Omega = \sqrt{2}$.



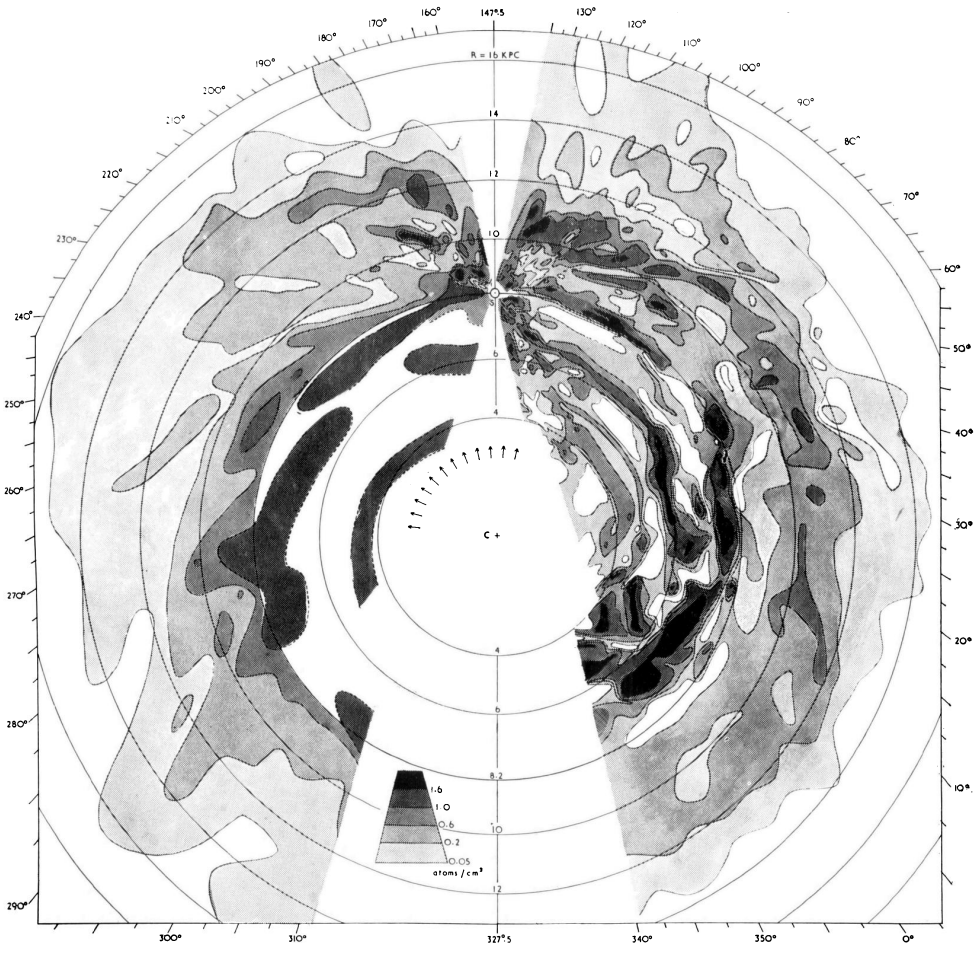


Figure 1.3: Oort's MW map traced by the 21-cm line. The figure is taken from Oort et al. (1958).

line-of-sight velocity for a given l ($-90^\circ \leq l \leq 90^\circ$), by differentiating Equation (1.2a) by d . The maximum velocity is given by

$$v_{\max} = v_c(R) - v_0 \sin l \quad \text{at} \quad R = R_0 \sin l, \quad (1.6)$$

where v_0 is a circular velocity at $R = R_0$. We obtain the rotation curve $v_c(R)$ measuring this maximum line-of-sight velocity (terminal velocity) for various l . For the outer Galaxy ($R > R_0$), the terminal velocity method cannot be applied. To obtain the circular velocity using the line-of-sight velocities, we need to estimate distances to gas clouds independently. Alternatively, we can derive the rotation velocity from the observations of line-of-sight velocities or proper motions of stellar and gaseous sources if their distances are given. The very long base-line interferometry (VLBI) observations of molecular masers associated with high-mass star-forming regions are useful for measuring circular velocity because they provide parallaxes, proper motions and radial velocities for distant sources (Reid et al. 2019; VERA Collaboration et al. 2020).

Fig. 1.4 shows the rotation curve of the MW. We plot the results from Sofue et al. (2009), Reid et al. (2019) and Eilers et al. (2019). All data are rescaled to $(R_0, v_0) = (8.2 \text{ kpc}, 233 \text{ km s}^{-1})$ for comparison. Sofue et al. (2009) collected circular velocities data measured with the terminal velocity method in the inner Galaxy and other methods in the both inner and outer Galaxy. Reid et al. (2019) measured circular velocities of molecular masers associated with high-mass star-forming regions observed with the VLBI technique. Eilers et al. (2019) estimated circular velocities of red giant stars from their kinematics. Between $R \sim 5 \text{ kpc}$ and $\sim 15 \text{ kpc}$, the rotation curve is almost flat as observed in external disc galaxies. At $R \gtrsim 20 \text{ kpc}$, the circular velocity slightly decreases with R in Eilers et al. (2019)'s data. As discussed in previous studies (e.g. Englmaier & Gerhard 1999; Fux 1999), we need to be careful about the implication of circular velocities derived with the terminal velocity method at $R \lesssim 5 \text{ kpc}$ because the bar induces strong non-circular motion. The dip at $R \sim 3 \text{ kpc}$ in the rotation curve of Sofue (2017b) is possibly related

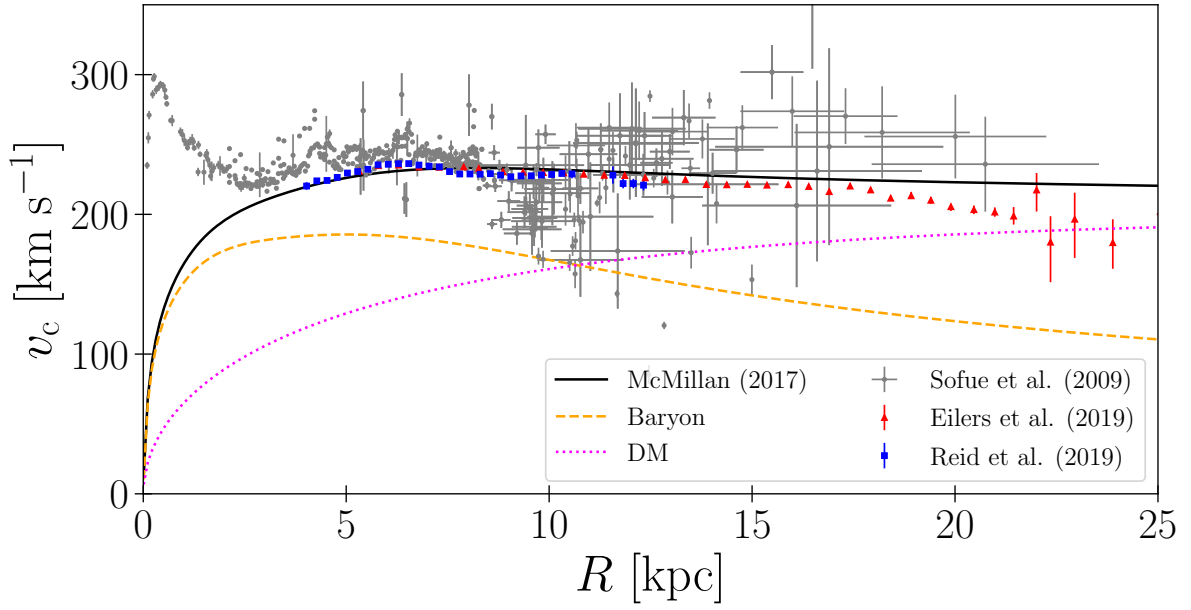


Figure 1.4: Rotation curve of the MW. Grey dots: the data compiled by Sofue et al. (2009). Blue squares: VLBI observations of masers in high-mass star-forming regions (Reid et al. 2019). Red triangles: kinematics of red giant stars (Eilers et al. 2019). The black line shows the rotation curve for the MW potential model of McMillan (2017). Orange and magenta lines are the circular velocities for baryonic (bulge, stellar disc and gas disc) and DM components, respectively. All data are rescaled to $(R_0, v_0) = (8.2 \text{ kpc}, 233 \text{ km s}^{-1})$.

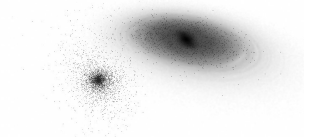
to the bar. In Fig. 1.4, the rotation curve for the MW model of McMillan (2017) is also plotted. The orange line indicates the circular velocity due to the baryonic components (bulge, stellar disc and gas disc). Their contribution is only $\sim 70\%$ of the observed value at $R = 10 \text{ kpc}$. If a spherical mass distribution is assumed, the circular velocity at R and the mass interior to R , $M(R)$, are related by

$$v_c^2(R) = \frac{GM(R)}{R}. \quad (1.7)$$

The mass of the baryonic components is only $\sim 50\%$ of the dynamically estimated mass within 10 kpc from the Galactic centre. This discrepancy between the visible mass and dynamical mass strongly indicates the existence of the dark matter (DM). Even if we release the assumption of the spherical mass distribution, the missing mass problem is not resolved (Binney & Tremaine 2008). It is worth noting that Oort already mentioned the missing mass in 1932 based on the analysis of the motion of the solar neighbourhood stars (Oort 1932). In our understanding today, the DM distributes spherically and extends far outside the disc. Recent observations suggest the virial radius and virial mass of the DM halo are $282 \pm 30 \text{ kpc}$ and $1.3 \pm 0.3 \times 10^{12} M_\odot$, respectively (Bland-Hawthorn & Gerhard 2016).

1.1.3 Bulge/bar

The MW has a bulge at its centre. Its morphology is distinguished from the disc as a vertically thicker component. This thick structure of the bulge in the MW was first reported by Okuda et al. (1977) who observed the central region of the MW at near-infrared (NIR) wavelengths using a balloon-borne telescope. Observations by the Cosmic Background Explorer (COBE) satellite revealed a more detailed structure of the bulge. Fig. 1.5 shows the infrared (IR) image of the MW obtained by the COBE. In the optical image (Fig. 1.1), light from the bulge is largely blocked by the dust. On the other hand, in the IR image, the bulge is clearly visible. In the figure, we find two striking features of the bulge. First, the bulge is not symmetric, and the left side ($l > 0$) is brighter and thicker than the right side ($l < 0$). This indicates that the bulge forms a bar and its near side is at $l > 0$. The second interesting feature is the non-ellipsoidal vertical structure called the boxy/peanut (BP) shape. BP bulges are typically seen in edge-on galaxies (e.g. Bureau & Freeman 1999). The origin of the BP bulge/bar is still in debate. One of the possible scenarios is that the BP structure is formed by the buckling instability. N -body simulations reproduced



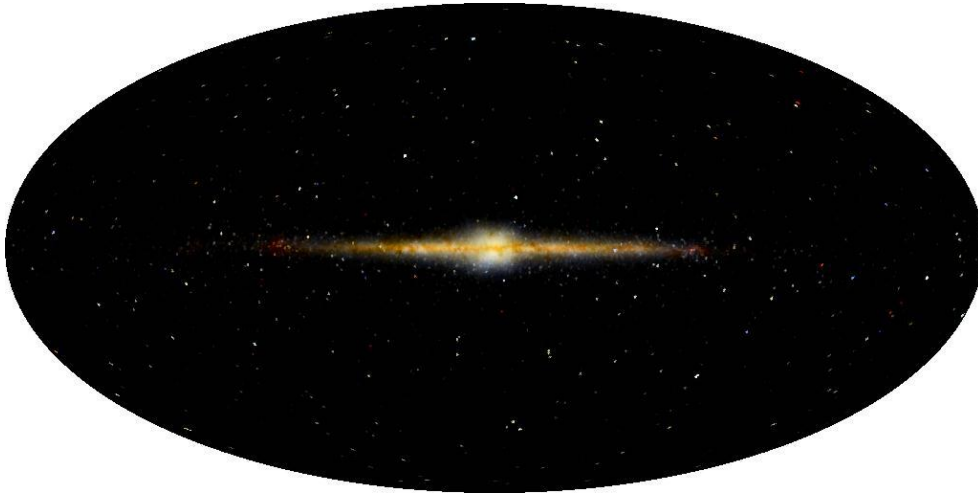


Figure 1.5: IR image of the MW obtained by the COBE satellite. Credit: E. L. Wright/UCLA, NASA/COBE Science Team.

BP bulges originating from bar buckling (e.g. Raha et al. 1991; Merritt & Sellwood 1994; Athanassoula 2005; Debattista et al. 2017, 2020; Khoperskov et al. 2019; Li et al. 2023b). Another scenario of the BP bulge formation is the vertical resonant effect (e.g. Combes & Sanders 1981; Combes et al. 1990; Friedli & Pfenniger 1990; Pfenniger 1990; Quillen 2002; Quillen et al. 2014; Sellwood & Gerhard 2020; Baba et al. 2022). Some bulge properties can be reasonably explained by bar buckling (Shen & Zheng 2020), but there is no critical evidence to prove the bar buckling scenario for the BP bulge in the MW. The symmetry of the bulge about the mid-plane implies that the buckling did not occur within at least a few Gyr (Li & Shen 2012).

The long bar is another bar in the MW disc. In contrast to the BP bulge/bar, the long bar is often referred to simply as the bar. It is characterised by a longer and thinner morphology than the BP bulge/bar. Its signature was reported as an overdensity of stars from $l = 0^\circ$ to $l \sim 28^\circ$ by Hammersley et al. (2000), and more evidently illustrated by the *Spitzer*/Galactic Legacy Infrared Midplane Survey Extraordinaire (GLIMPSE) survey data (Benjamin et al. 2005). Wegg et al. (2015) investigated the structure of the long bar using red clump giants. Based on their estimation, the half length of the long bar is 5.0 ± 0.2 kpc and the angle between its major axis and the line connecting the Sun and the Galactic centre is $28\text{--}30^\circ$.

Observations of external galaxies suggest that there are at least two types of bulges: classical bulges and pseudo bulges. Classical bulges show properties similar to elliptical galaxies. They consist of old stellar populations and have spherical shapes dominated by the random motion of stars. On the other hand, pseudo bulges consist of relatively younger stellar populations and have rotation-dominated disc-like structures. Since the MW bulge rotates, it is classified as a pseudo bulge. Observationally, it is unclear whether the MW has a classical bulge (Bland-Hawthorn & Gerhard 2016). Shen et al. (2010) showed that N -body models with classical bulges whose mass is less than $\sim 8\%$ of the disc mass reproduce the observed bulge kinematics.

1.1.4 Spiral arms

Spiral arms are another prominent non-axisymmetric feature in the MW disc. They are commonly visible structures in disc galaxies. In the local Universe, $\sim 80\%$ of the disc galaxies have spiral arms (Willett et al. 2013). Even in the distant Universe, galaxies with spiral arms are discovered (e.g. Tsukui & Iguchi 2021). William Morgan first identified spiral arms of the MW. He intensively worked on spectroscopic studies of young OB stars, and developed a stellar classification system known as the MK system (Morgan et al. 1943) along with Philip Keenan and Edith Kellman. Using this classification system, he determined absolute magnitudes of OB stars and their distances. By measuring distances to groups of OB stars (OB associations) in H II regions detected by H α emission lines, Morgan discovered that OB stars and H II regions distribute in a spiral structure (Morgan et al. 1952, 1953).

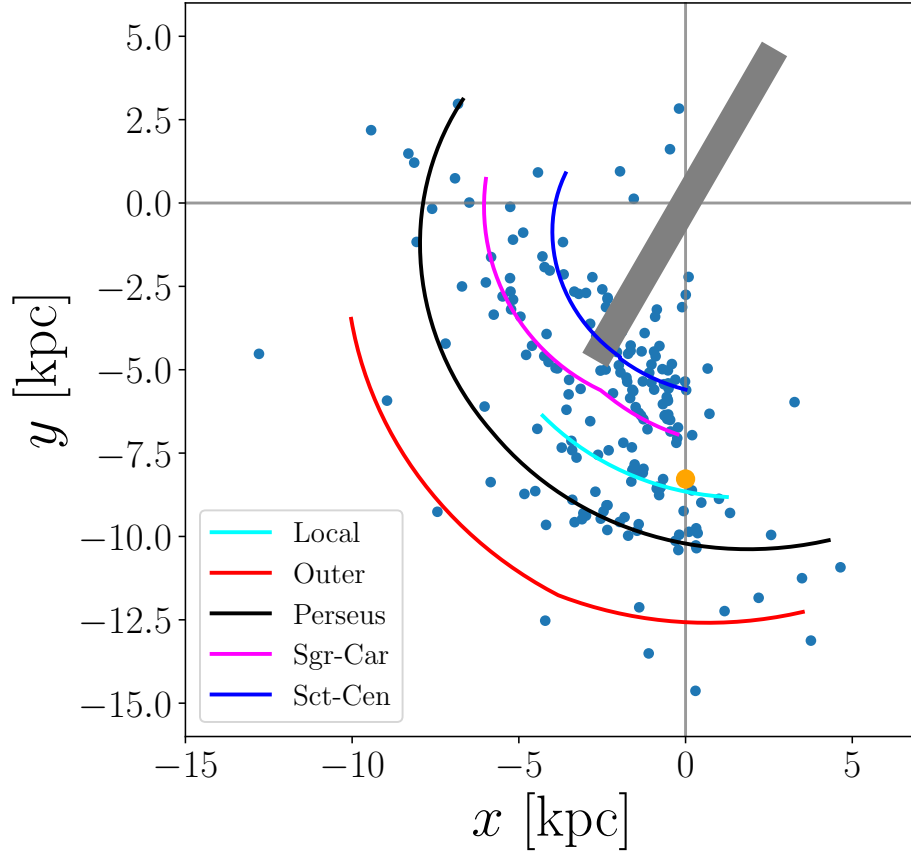


Figure 1.6: Spiral arms of the MW suggested by the VLBI observations of molecular masers. Blue points show locations of high-mass star-forming regions. Cyan, red, black, magenta and blue lines indicate the positions of the Local arm, Outer arm, Perseus arm, Sagittarius-Carina arm and Scutum-Centaurus arm, respectively. The grey rectangle indicates the location of the long bar (Wegg et al. 2015). The orange dot indicates the position of the Sun.

Spiral arms have been studied with various tracers (Vallée 2017; Shen & Zheng 2020), but there are still debates about the number of arms and their locations. Observations of young massive protostars and OB stars associated with H II regions suggest that the MW is a four-arm spiral galaxy (e.g. Georgelin & Georgelin 1976; Lumsden et al. 2013; Urquhart et al. 2014). Observations of neutral hydrogen (e.g. Nakanishi & Sofue 2016), high-mass star-forming regions (Reid et al. 2014, 2019; VERA Collaboration et al. 2020) and classical Cepheids (Dambis et al. 2015; Skowron et al. 2019) also support the four-arm spiral model. The VLBI is one of the most powerful tools to study the spiral structure of the MW. It can measure trigonometric parallaxes of molecular masers associated with young massive stars and provide accurate distances to them (Reid et al. 2014, 2019; VERA Collaboration et al. 2020). Fig. 1.6 shows the locations of the high-mass star-forming regions whose distances are determined through VLBI parallax measurements. We have used the data compiled by Reid et al. (2019). The lines in the figure indicate the locations of the four major arms (Outer arm, Perseus arm, Sagittarius-Carina arm and Scutum-Centaurus arm) and the Local arm estimated with fitting to the logarithmic spirals. The Sun is located between two major arms: the Perseus arm and the Sagittarius-Carina arm, and beside the Local arm.

While observations of gaseous tracers and young stars support the four-major-arm model, observations of old stars at IR wavelengths favour a two-arm model (e.g. Drimmel 2000; Benjamin et al. 2005; Churchwell et al. 2009). Benjamin et al. (2005) and Churchwell et al. (2009) measured the number density of the sources in *Spitzer*/GLIMPSE surveys as a function of the Galactic longitude in $-70^\circ \lesssim l \lesssim 70^\circ$. They found the excesses of the stellar density around the tangencies of the Scutum-Centaurus arm, Norma arm and the 3-kpc arm. On the other hand, such a density excess is not found around the tangency of the Sagittarius arm. They concluded that the MW has two major arms: the Scutum-Centaurus arm and the Perseus

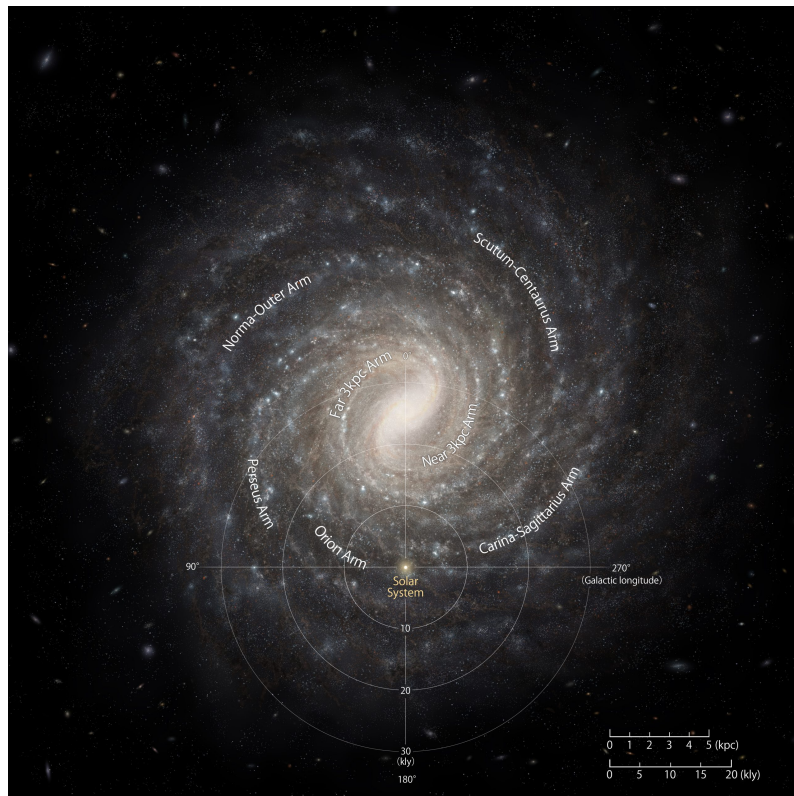
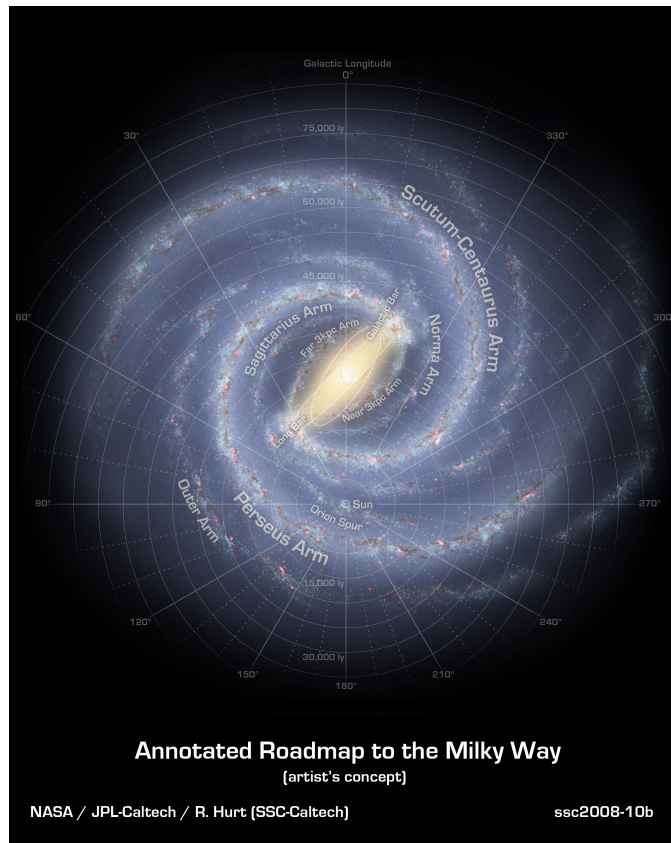


Figure 1.7: Artists' concepts of the [MW](#). *Top*: Model with two major arms. Credit: NASA/JPL-Caltech/R. Hurt *Bottom*: Model with four major arms. Credit: NAOJ, Hiroyuki NAKANISHI and Yoshiaki SOFUE, M. J. Reid et al, Baba et al.

arm. The top panel of Fig. 1.7 shows an artist's concept of the MW based on the two-arm model. This image refers to the results of observations by the *Spitzer* satellite and other observations at radio, IR and optical wavelengths (Churchwell et al. 2009). For comparison, we show a concept image for the four-arm model in the bottom panel of Fig. 1.7. This image is based on the radio observations of neutral hydrogen (Nakanishi & Sofue 2016), the VLBI observations of the high-mass star-forming regions (Reid et al. 2019) and *N*-body/hydrodynamical simulations of a MW-like galaxy (Baba et al. 2017).

1.1.5 Other components

Thin disc and thick disc

The MW has two disc components. The first one is the thin disc, which consists of kinematically cold, young, metal-rich stars. The scale height of the thin disc is ~ 300 pc. The second component is the thick disc, whose scale height is ~ 1 kpc. Stars in the thick disc are kinematically hot, old and metal-poor. In the solar neighbourhood, $\sim 4\%$ of stars belong to the thick disc (Bland-Hawthorn & Gerhard 2016).

Stellar halo

The stellar halo is a spherical component surrounding the MW disc. It extends to ~ 150 kpc from the Galactic centre (Fukushima et al. 2019). The stellar halo contributes $\sim 1\%$ of the stellar mass in the MW. The stars in the halo are old and metal-poor, and a large fraction of them are considered to have originated from disrupted satellite galaxies and globular clusters.

Satellite galaxies

In the lower right-hand corner of Figure 1.1, we can see two of the largest satellite galaxies: Large Magellanic Cloud (LMC) and Small Magellanic Cloud (SMC). Many other satellite galaxies orbit around the MW disc, and the Sagittarius dwarf galaxy (Sgr) has the largest dynamical influence on the MW disc. It was originally discovered by Ibata et al. (1994) in the direction of the Galactic centre. Its distance from the Galactic centre is ~ 20 kpc (Vasiliev & Belokurov 2020). It is being disrupted tidally, and the stripped stars form a prominent stellar stream called the Sagittarius stream.

1.2 SPACE ASTROMETRY

Astrometry is one of the most fundamental and traditional branches of astronomy, which aims to precisely measure the positions and velocities of celestial objects. Astrometric data enable us to make a three-dimensional (3D) map of the MW and exploration of its dynamical structure through stellar kinematics. Annual parallax measurements provide the most accurate distances to nearby stars in the MW. Astrometric observations of stars were made using ground-based telescopes until the 1980s, but their precisions were limited due to atmospheric distortion. Therefore, space astrometry was required for more precise measurements.

In 1989, European Space Agency (ESA) launched *Hipparcos*, the first astrometry satellite. After 42 months of observation and data processing, the *Hipparcos* catalogue (ESA 1997; Perryman et al. 1997) was published in 1997. The *Hipparcos* catalogue contains astrometry data for 117,955 sources and the typical parallax uncertainty for bright sources with the *Hipparcos* magnitude $H_p < 9$ mag is 1 mas. From the data of the star mapper, which is equipment to determine the orientation of the satellite, the Tycho catalogue (Hoeg et al. 1997) was constructed. Although its astrometric accuracy is lower than that of the *Hipparcos* catalogue, it contains astrometric and photometric data for more than 1 million stars. Modifying the reduction of the same observation data as the Tycho catalogue, Høg et al. (2000) constructed the Tycho-2 catalogue, which contains positions, proper motions and photometry for 2,539,913 stars. Typical uncertainty in positions is 10–100 mas. Table 1.1 provides the source numbers and astrometry uncertainties of the *Hipparcos* and Tycho-2 catalogues. Fig. 1.8 shows the spatial distribution of the *Hipparcos* sources with relative parallax errors of less than 20%. The background is the artist's concept of the MW in the top panel of Fig. 1.7. From the precise astrometric data, detailed phase-space distributions of the solar neighbourhood stars were determined for the first time (e.g. Dehnen 1998, 1999b).



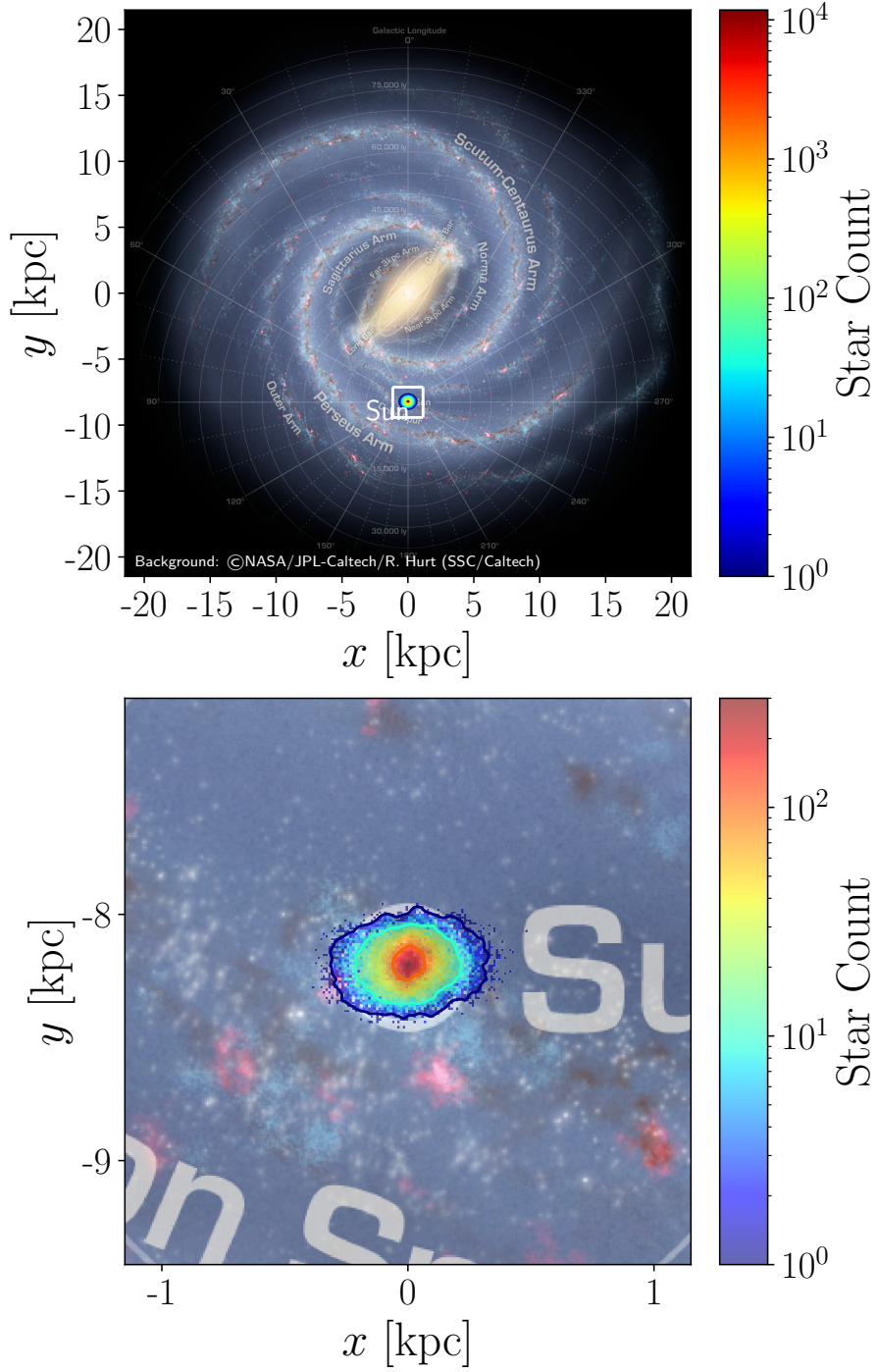


Figure 1.8: Spatial coverage of the *Hipparcos* data. *Top*: The number counts of the *Hipparcos* sources with relative parallax errors less than 20% are plotted on an artist's concept of the *MW* (credit: NASA/JPL-Caltech/R. Hurt). *Bottom*: Enlargement of the region enclosed by the white box in the top panel.

Table 1.1: Comparison between the *Hipparcos* and *Gaia* catalogues.

	<i>Hipparcos</i>		<i>Gaia</i>
	<i>Hipparcos</i>	Tycho-2	DR3
Number of sources			
Total	118,218	2,539,913	1,811,709,771
Astrometry sources	117,955	2 430 468	1,467,744,818
Radial velocity sources	—	—	33,812,183
Uncertainty	($H_p < 9$ mag)	(All stars)	($G < 15$ mag)
Parallax [mas]	1	—	0.02–0.03
Position [mas]	0.7	60	0.01–0.02
Proper motion [mas yr ⁻¹]	0.8	2.5	0.02–0.03

Gaia, the successor of *Hipparcos*, was adopted as one of the ESA’s Horizon 2000+ programmes in 2000. There are many technical updates in *Gaia*, which enable orders of magnitude improvements in the data quality and quantity (Perryman 2023). For instance, while the diameter of the *Hipparcos*’s primary mirror is 30 cm, the *Gaia*’s mirror size is $1.5 \times 0.5 \text{ m}^2$. The photomultiplier-based detector was replaced by the CCD arrays. Regarding the observation locations, *Hipparcos* is a geostationary transfer orbit of Earth, and *Gaia* is in an orbit around the second Sun-Earth Lagrange point L_2 . In addition to the astrometry instrument, other two types of instruments are installed in *Gaia*. Blue and Red Photometers (BP/RP) measure low-resolution spectra by fused-silica prisms. The BP/RP spectra are used to estimate stellar parameters such as the effective temperature, surface gravity and chemical composition. Radial-Velocity Spectrometer (RVS) is a high-resolution spectrometer designed to measure radial velocities of stars. Combining the 5D astrometry data and the radial velocity data, we can map stars in 6D phase space.

Gaia was launched in December 2013 (Gaia Collaboration et al. 2016a). After a six-month commissioning period, it started the five-year nominal science operation in July 2014. The *Gaia* Data Release 1 (DR1) catalogue was published in 2016 based on the first 14 months of the operation (Gaia Collaboration et al. 2016b). It contains positions (α , δ) and *Gaia* G-band magnitudes for 1,142,679,769 sources, and five-parameter astrometric solutions (α , δ , μ_α , μ_δ , ω) for 2,057,050 stars in common between the *Gaia* DR1, *Hipparcos* and Tycho-2 catalogues. The uncertainties of the position and the proper motion are ~ 0.3 mas and $\sim 0.06 \text{ mas yr}^{-1}$, respectively. For the 93,635 stars in common with the *Hipparcos* catalogue, the typical uncertainty for the parallax is 0.3 mas. Note that there is an additional systematic error of ~ 0.3 mas.

The *Gaia* Data Release 2 (DR2) catalogue (Gaia Collaboration et al. 2018a) was published in 2018 based on 22 months of observation. It contains the five-astrometric solution for 1,331,909,727 sources. The uncertainties of the parallax, position and proper motion are 0.02–0.04 mas, 0.02–0.04 mas and 0.07 mas yr^{-1} , respectively, for the sources brighter than $G = 15$ mag. In addition, the radial velocities obtained with the RVS are available for 7,224,631 sources. We can convert the five astrometric parameters and the radial velocity into the 6D phase-space coordinate. As described in Section 1.4, there are many important discoveries about the dynamical structure of the MW in this phase-space information.

The data obtained during the 34 months of observation were released in two parts: *Gaia* Early Data Release 3 (EDR3) (Gaia Collaboration et al. 2021) and *Gaia* Data Release 3 (DR3) (Gaia Collaboration et al. 2023a). The full astrometric solution is available for 1,467,744,818 sources, and the uncertainty of the parallax, position and proper motion for the stars with $G < 15$ mag are 0.02–0.03 mas, 0.01–0.02 mas and $0.02\text{--}0.03 \text{ mas yr}^{-1}$, respectively. The *Gaia* DR3 catalogue contains the radial velocity for 33,812,183 sources. Furthermore, it includes the astrophysical parameters such as the effective temperature, surface gravity and metallicity from BP/RP spectra and RVS spectra.

Although the nominal mission of *Gaia* was five years from 2014 to 2019, ESA’s Science Programme Committee decided the extension up to 2025. DR4 based on the 5.5 years of observation is planned to be released not before the end of 2025. The final data release based on all mission data is expected not before the end of 2030.

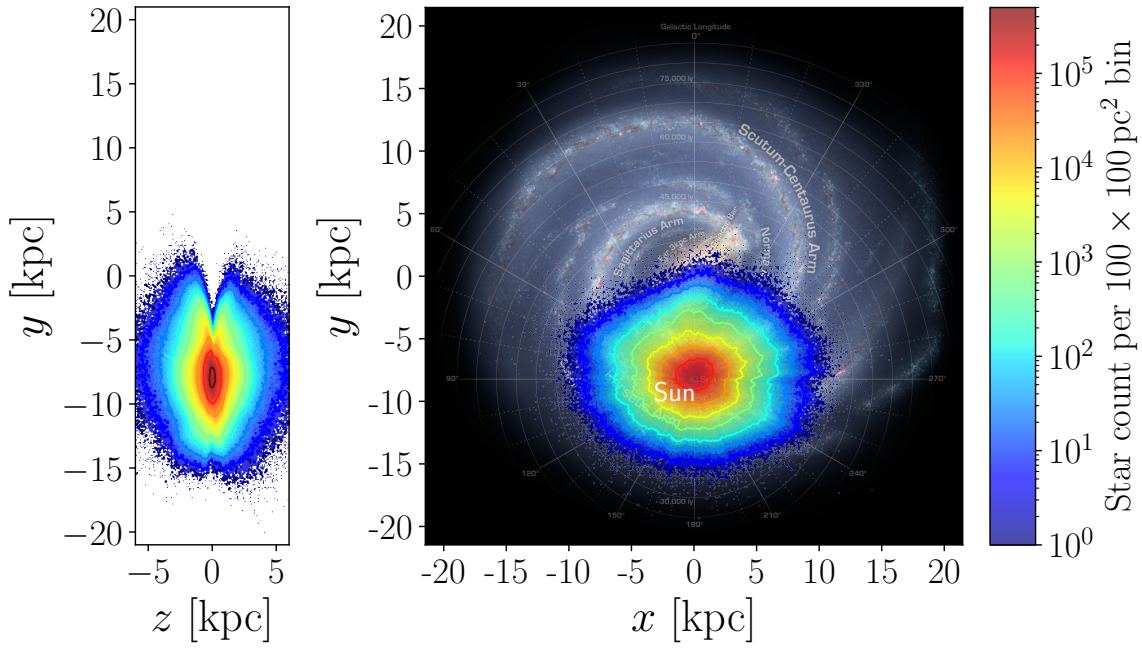


Figure 1.9: Spatial coverage of the *Gaia* data. The distribution of the *Gaia* DR3 sources with relative parallax errors of less than 20% is plotted in the y - z plane (left) and in the x - y plane (right).

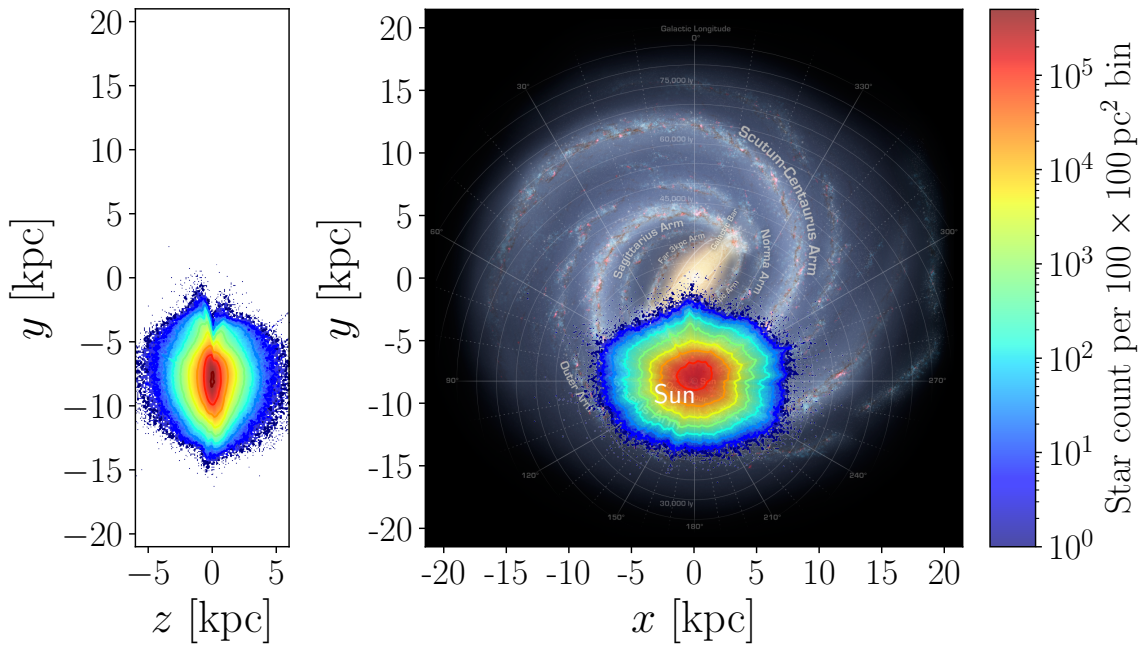


Figure 1.10: Spatial coverage of the *Gaia* DR3 radial velocity sample.

Fig. 1.9 shows the face-on and edge-on distribution of the *Gaia* DR3 sources with relative parallax errors less than 20%. As comparison with Fig. 1.8 indicates, the spatial coverage of the *Gaia* data is more than 100 times larger than that of the *Hipparcos*. The completeness roughly decreases with the distance from the Sun but is worse in the Galactic centre direction and around the mid-plane due to the dust extinction.

Fig. 1.10 shows the same plot for the *Gaia* DR3 radial velocity sample. In the *Gaia* DR3, radial velocities are available for 33,812,183 stars with $G_{\text{RVS}} < 14$ mag and with $3100 < T_{\text{eff}} < 14500$ K, where G_{RVS} and T_{eff} are the magnitude derived from the integration of the RVS spectra and the effective temperature, respectively. The typical uncertainty of the radial velocity for the bright stars is an order of a few km s^{-1} .

1.3 THEORETICAL BACKGROUNDS

1.3.1 Angle-action variables

We introduce a special set of canonical coordinates known as angle-action variables. Describing orbits with angle-action variables is useful both theoretically and practically (Binney & Tremaine 2008). One of the theoretical merits of the angle-action variables is that they can describe orbits in the mathematically simplest manner. We select three integrals of motion called actions $\mathbf{J} = (J_1, J_2, J_3)$ as momenta. Conjugated coordinates $\boldsymbol{\theta} = (\theta_1, \theta_2, \theta_3)$ are called angles. The conversion from generalized coordinates \mathbf{q} and generalized momenta \mathbf{p} to actions is formally given by the following equation.

$$J_i = \frac{1}{2\pi} \oint p_i dq_i \quad (1.8)$$

where the integral is taken over the orbit. Here, we assume that \mathbf{p} and \mathbf{q} are periodic functions of time. From the definition of an integral of motion, actions do not depend on time. Hamilton's equations for J_i lead to

$$\dot{J}_i = -\frac{\partial H}{\partial \theta_i} = 0, \quad (1.9)$$

where H is the Hamiltonian of the system. Equation (1.9) shows the Hamiltonian H does not depend of angles. Hence, the right-hand side of the Hamilton's equations for θ_i ,

$$\dot{\theta}_i = \frac{\partial H}{\partial J_i} \equiv \Omega_i(\mathbf{J}), \quad (1.10)$$

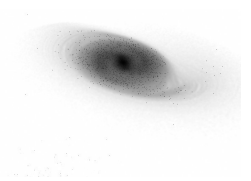
is constant. The solution is simply a linear function of time,

$$\theta_i = \Omega_i t + \theta_i(0). \quad (1.11)$$

where Ω_i is orbital frequency.

In axisymmetric systems, (J_R, J_ϕ, J_z) is a useful set of actions. Azimuthal action J_ϕ is identical to angular momentum L_z , and we can determine it as a product of galactocentric radius R and azimuthal velocity v_ϕ . On the other hand, there are no analytic expressions in conversion from phase-space coordinates to radial action J_R and vertical action J_z for general analytic potentials. Some methods for (approximately) computing actions are proposed. Examples of them are torus fitting (Kaasalainen & Binney 1994; McMillan & Binney 2008; Binney & McMillan 2011), adiabatic approximation (Binney 2010; Binney & McMillan 2011; Schönrich & Binney 2012) and Stäckel fudge (Binney 2012).

As a practical application of action variables in the analysis of stellar kinematics data, they can be used to characterise and classify orbits of stars. Trick et al. (2019) computed actions for stars in the *Gaia* DR2 dataset (Gaia Collaboration et al. 2018a), and identified overdensities and ridges in L_z - J_R space. Fig. 1.11, taken from Trick et al. (2019), shows the mapping of stars from action space to radial velocity (v_R) versus azimuthal velocity (v_ϕ) space. For the samples within 200 pc from the Sun, stars in the overdensities, called ridges, in action space correspond to overdensities (streams) in velocity space. On the other hand, for the samples between 200 pc and 600 pc, we can easily identify groups of stars that are concentrated in action space but are widely distributed in velocity space and do not form well-defined overdensities. Even if stars belong to the same orbital family, they may have significantly different velocities. Using actions, we can more easily identify kinematically associated groups of stars.



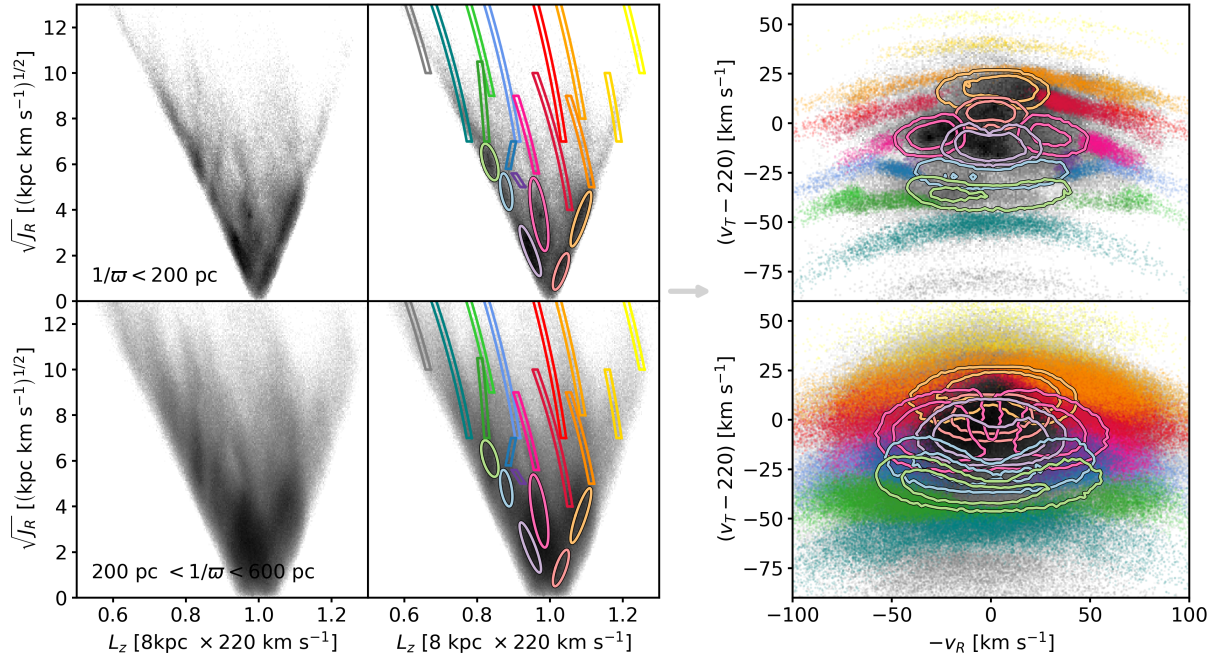


Figure 1.11: Mapping from action space to velocity space. The stars in overdensities in action space are mapped into velocity space. The colours of the dots in velocity space indicate that they are located in boxes of the same colour in action space. *Top*: *Gaia* DR2 samples within 200 pc from the Sun. *Bottom*: *Gaia* DR2 samples between 200 pc and 600 pc from the Sun. This figure is taken from [Trick et al. \(2019\)](#)

1.3.2 Resonances

This section briefly describe the concept of orbital resonances in disc galaxies. We refer to Section 3.3 of [Binney & Tremaine \(2008\)](#). We consider a nearly axisymmetric potential rotating with a constant pattern speed of Ω_b :

$$\Phi(R, \phi) = \Phi_0(R) + \Phi_1(R, \phi), \quad (1.12)$$

where (R, ϕ) are polar coordinates rotating with Ω_b and $|\Phi_1 / \Phi_0| \ll 1$. The Lagrangian and the Lagrange's equations in the potential are

$$L = \frac{1}{2} \dot{R}^2 + \frac{1}{2} [R(\dot{\phi} + \Omega_b)]^2 - \Phi(R, \phi), \quad (1.13)$$

$$\ddot{R} = R(\dot{\phi} + \Omega_b)^2 - \frac{\partial \Phi}{\partial R}, \quad (1.14)$$

$$\frac{d}{dt} [R^2(\dot{\phi} + \Omega_b)] = -\frac{\partial \Phi}{\partial \phi}, \quad (1.15)$$

We assume solutions for the Lagrange's equations are described as

$$R(t) = R_0 + R_1(t); \quad \phi(t) = \phi_0(t) + \phi_1(t). \quad (1.16)$$

where $|R_1 / R_0| \ll 1$, $|\phi_1 / \phi_0| \ll 1$, and R_0 is a constant. When we select Φ_1 written as

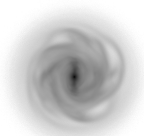
$$\Phi_1(R, \phi) = \Phi_b(R) \cos(m\phi) \quad (m \in \mathbb{N}), \quad (1.17)$$

we can analytically solve the equations under the first-order approximation. ϕ_0 is the azimuth for the circular orbit at $R = R_0$:

$$\phi_0 = (\Omega_0 - \Omega_b)t, \quad (1.18)$$

where

$$\Omega_0 \equiv \left[\sqrt{\frac{1}{R} \frac{d\Phi_0}{dR}} \right]_{R_0} \quad (1.19)$$



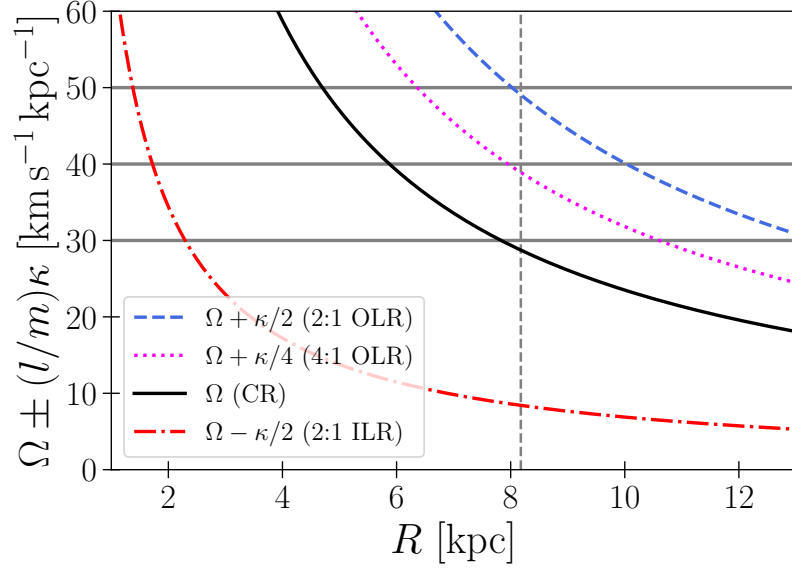


Figure 1.12: The orbital frequencies as functions of the galactocentric radius, R . The blue, magenta, black and red lines represent $\Omega \pm (l/m)\kappa$ for 2:1, 4:1 OLRs, CR and 2:1 ILR, respectively. The horizontal lines indicate the bar's pattern speeds of $\Omega_b = 30, 40$ and $50 \text{ km s}^{-1} \text{ kpc}^{-1}$. The vertical line represents the Sun's radius of $R \approx 8.2 \text{ kpc}$.

is the circular frequency evaluated at $R = R_0$. The solution for R_1 is

$$R_1(\phi_0) = C_1 \cos\left(\frac{\kappa_0 \phi_0}{\Omega_0 - \Omega_b} + \alpha\right) + C_2 \cos(m\phi_0), \quad (1.20)$$

where C_1 and α are constants, and

$$C_2 \equiv -\frac{1}{\Delta} \left[\frac{d\Phi_b}{dR} + \frac{2\Omega\Phi_b}{R(\Omega - \Omega_b)} \right]_{R_0}, \quad (1.21)$$

$$\Delta \equiv \kappa_0^2 - m^2(\Omega_0 - \Omega_b)^2, \quad (1.22)$$

$$\kappa_0^2 \equiv \left(R \frac{d\Omega^2}{dR} + 4\Omega^2 \right)_{R_0}. \quad (1.23)$$

R_1 is singular at

$$\Omega_0 = \Omega_b \quad (1.24)$$

and

$$m(\Omega_0 - \Omega_b) = \pm \kappa_0. \quad (1.25)$$

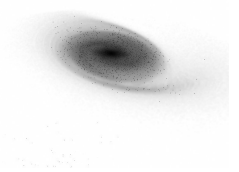
The first case is called corotation resonance (CR). The plus and minus signs in the second case are called inner Lindblad resonance (ILR) and outer Lindblad resonance (OLR), respectively. Generalizing the concept, this thesis and some literatures (e.g. Hattori et al. 2019) call $m:l$ Lindblad resonances as

$$m(\Omega_\phi - \Omega_b) = \pm l\Omega_R \quad (l \in \mathbb{N}), \quad (1.26)$$

where Ω_ϕ and Ω_R are orbital frequencies in radial and azimuthal directions, respectively. We rewrite Equation (1.26) as

$$\Omega_\phi \mp \frac{l}{m}\Omega_R = \Omega_b \quad (1.27)$$

The resonance radius is defined as R at which the left-hand side of Equation (1.27) is equal to the bar pattern speed. In Fig. 1.12, we plot the left-hand side of Equation (1.27) as functions of R for 2:1 OLR,



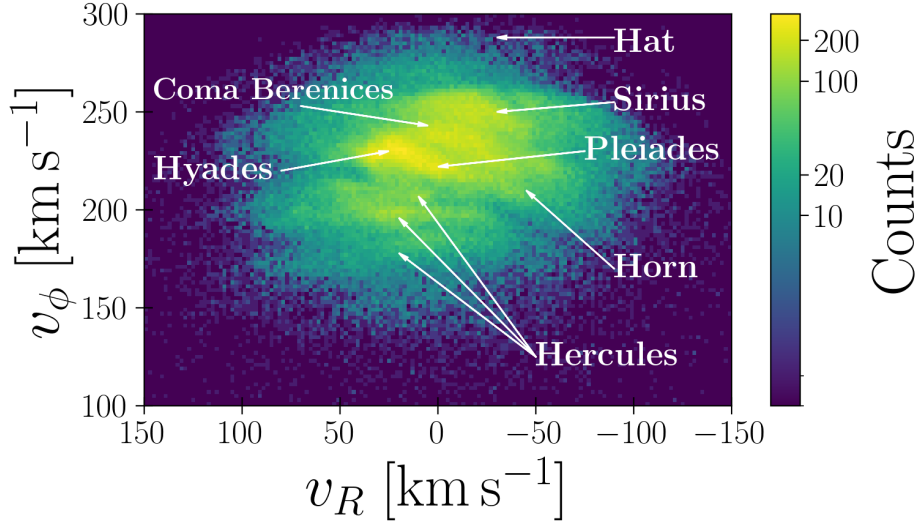


Figure 1.13: Velocity-space distribution of the solar neighbourhood stars. Radial and azimuthal velocity-space distribution of the stars within 200 pc of the Sun. The data are taken from the *Gaia* DR3 catalogue.

4:1 OLR, CR and 2:1 ILR. We assume a flat rotation curve of 235 km s^{-1} , and calculate orbital frequencies from Equation (1.19) and Equation (1.23) under the epicycle approximation. 2:1 OLR, 4:1 OLR and CR are located in the solar neighbourhood for the bar pattern speeds of $\Omega_b = 50, 40$ and $30 \text{ km s}^{-1} \text{ kpc}^{-1}$.

For orbits of which $m(\Omega_\phi - \Omega_b) \mp l\Omega_R$ are close to zero, they can librate around the resonant orbits in phase space. Such a phenomenon is called resonant trapping, and its well-known examples are trojans, which are orbiting around the Lagrange point L_4 or L_5 of the main object and are trapped in the CR.

1.4 PHASE SPACE STRUCTURES OF THE DISC STARS

We can illustrate the 6D phase-space distribution from the astrometry data. It provides valuable insights into the present, past and future dynamical state of the MW.

1.4.1 Velocity-space substructures

Fig. 1.13 shows the velocity-space distribution of the stars within 200 pc from the Sun. The horizontal and vertical axes represent the radial and azimuthal velocities, respectively, in the Galactocentric cylindrical coordinates. The data are taken from the *Gaia* DR3 catalogue (Gaia Collaboration et al. 2023a). Fig. 1.14 shows an example of the same velocity-space distribution in a static axisymmetric disc model. We sample the distribution from Dehnen (1999a)'s distribution function (DF) for a flat rotation curve of 220 km s^{-1} . The sampling was performed using the GALPY PYTHON package (Bovy 2015). While Fig. 1.14 exhibits a smooth distribution, Fig. 1.13 reveals multiple overdensities referred to as velocity-space substructures or moving groups. The presence of a significant number of stars within each substructure rules out Poisson noise as an explanation. These substructures are likely to originate from non-axisymmetric features such as the bar and spiral arms or disrupted star clusters. The arrows in Fig. 1.13 indicate the names and locations of the major substructures. The most prominent one is the Hercules stream located at $v_\phi \lesssim 200 \text{ km s}^{-1}$. It was originally identified as the Hercules moving group (ζ Herculis moving group) by Eggen (1958b) and was hypothesized to be a disrupted star cluster (Eggen 1958a). The *Hipparcos* data (ESA 1997; Perryman et al. 1997) has revealed that the moving group is a part of the large velocity-space substructure (Dehnen 1998). Fig. 1.15 shows the velocity-space distribution same as Fig. 1.13, but here we use the parallax, position and proper motion data from the *Hipparcos* catalogue. Note that the *Hipparcos* catalogue does not contain the radial velocity data, and therefore they are taken from the Pulkovo Compilation of Radial Velocities (Gontcharov 2006). We can clearly identify the Hercules stream, but its internal trimodal structure, which the *Gaia* data show, is not resolved due to the limited number of stars and the accuracy of the astrometry. The orange dots in Fig. 1.15 indicate the velocities of the 22 stars originally identified as the

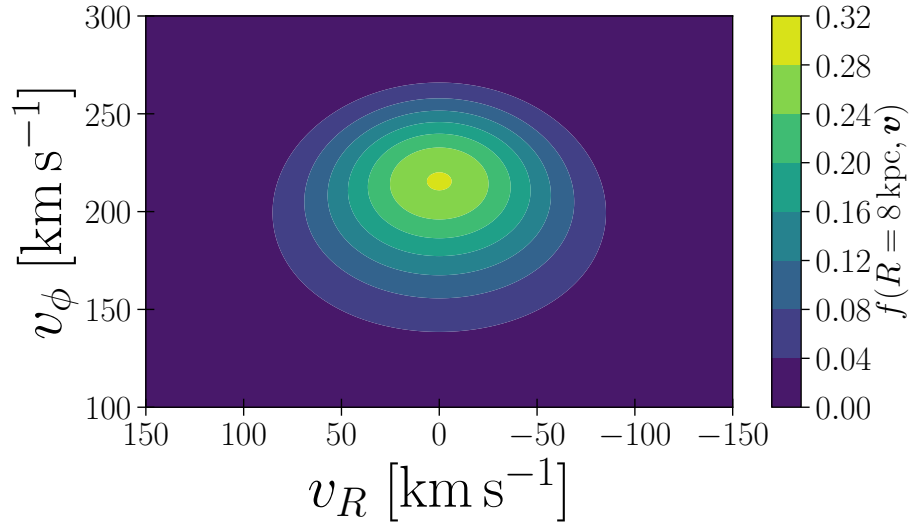


Figure 1.14: Velocity-space distribution of stars in an axisymmetric disc model.

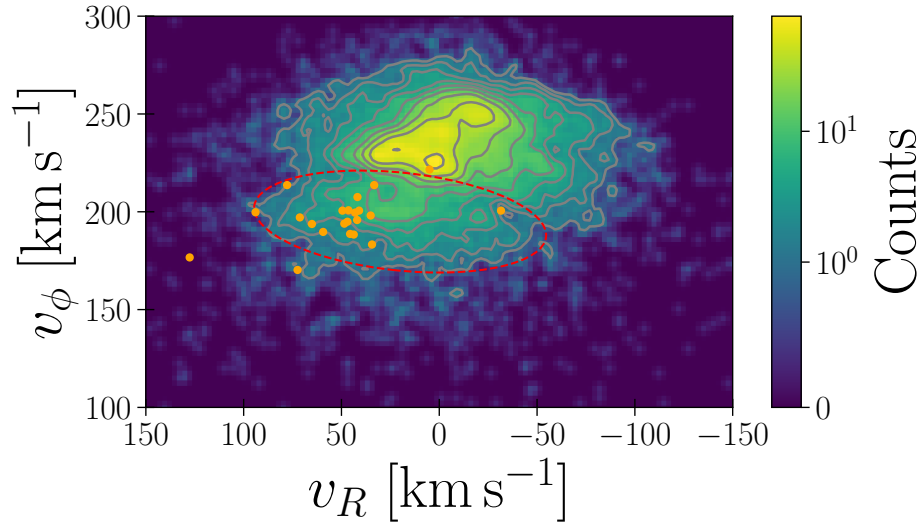
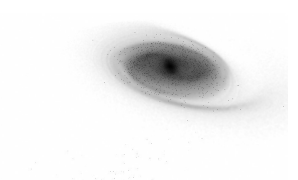


Figure 1.15: Velocity map from the *Hipparcos* data. Red ellipse indicates the location of the Hercules stream. Orange dots shows the velocities of the stars originally identified as the Hercules moving group in [Eggen \(1958b\)](#).



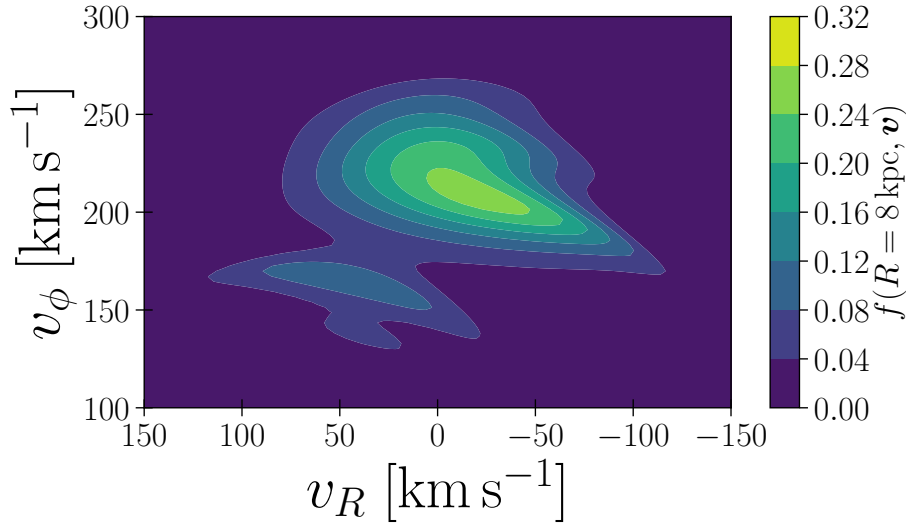


Figure 1.16: Velocity-space distribution in the Dehnen (2000)'s barred galaxy model.

members of the Hercules moving group in Eggen (1958b). To derive their velocities, we use astrometric and radial velocity data from the *Gaia* DR3 catalogue (Gaia Collaboration et al. 2023a) and other literatures (Latham et al. 2002; Gontcharov 2006; van Leeuwen 2007; Famaey et al. 2009; Jönsson et al. 2020).

The Hercules stream contains stars with a wide range of ages (Famaey et al. 2005), therefore non-axisymmetric dynamical structures rather than a disrupted star cluster can more reasonably explain its origin. Resonances of the Galactic bar provide a plausible explanation for the formation mechanism of the Hercules stream. Dehnen (2000) demonstrated that the bar's OLR forms the bimodality in the velocity-space distribution using a numerical simulation called the backward integration method. They integrated orbits of test particles backwards in time within a galactic potential with a slowly growing weak bar. The bar's amplitude is zero, and the potential is axisymmetric at $t = 0$. The amplitude increases slowly during $0 < t < t_1$ and is constant after $t = t_1$. In this process, when a particle orbits from a phase-space point $\mathbf{w}_2 = (\mathbf{x}_2, \mathbf{v}_2)$ at $t = t_2$ ($t_2 > t_1$) to \mathbf{w}_0 at $t = 0$, the collisionless Boltzmann equation ensures that the value of the DF, denoted as $f(\mathbf{w}_2, t_2)$, remains equal to $f(\mathbf{w}_0, 0)$. We cannot directly evaluate $f(\mathbf{w}_2, t_2)$, but $f(\mathbf{w}_0, 0)$ can be determined through analytical expressions of DFs for axisymmetric systems (e.g. Dehnen 1999a). Fig. 1.16 shows the velocity-space distribution generated with GALPY following the above procedure. We adopt the default model parameters of Dehnen (2000). The distribution is segmented into the main mode at $v_\phi \gtrsim 200 \text{ km s}^{-1}$ and the low- v_ϕ mode at $v_\phi \lesssim 200 \text{ km s}^{-1}$ corresponding to the Hercules stream.

Regarding bar resonances, the most important parameter is the pattern speed. It determines the radius where a resonance occurs if the background axisymmetric potential is given. If the Hercules stream originates from the OLR, its resonance radius is located inside the Sun's radial coordinate $R_0 \sim 8 \text{ kpc}$ and the corresponding pattern speed is $\Omega_b \gtrsim 50 \text{ km s}^{-1} \text{ kpc}^{-1}$ (Dehnen 1999b, 2000; Fux 2001; Minchev et al. 2007; Antoja et al. 2014). However, the recent direct and indirect measurements suggest the slower bar of $\Omega_b \lesssim 40 \text{ km s}^{-1} \text{ kpc}^{-1}$ (e.g. Portail et al. 2017; Bovy et al. 2019; Sanders et al. 2019; Binney 2020; Chiba et al. 2021; Kawata et al. 2021). If the slow bar case, the other resonances are located in the solar neighbourhood. The scenarios which explain the origin of the Hercules stream by the CR (e.g. Pérez-Villegas et al. 2017; Monari et al. 2019b; Binney 2020) and higher-order resonances such as 4:1 OLR (e.g. Monari et al. 2019a; Hunt & Bovy 2018) are proposed. Spiral arms and the combined effect of the bar and spiral arms can also form a Hercules-like stream (Hattori et al. 2019; Barros et al. 2020).

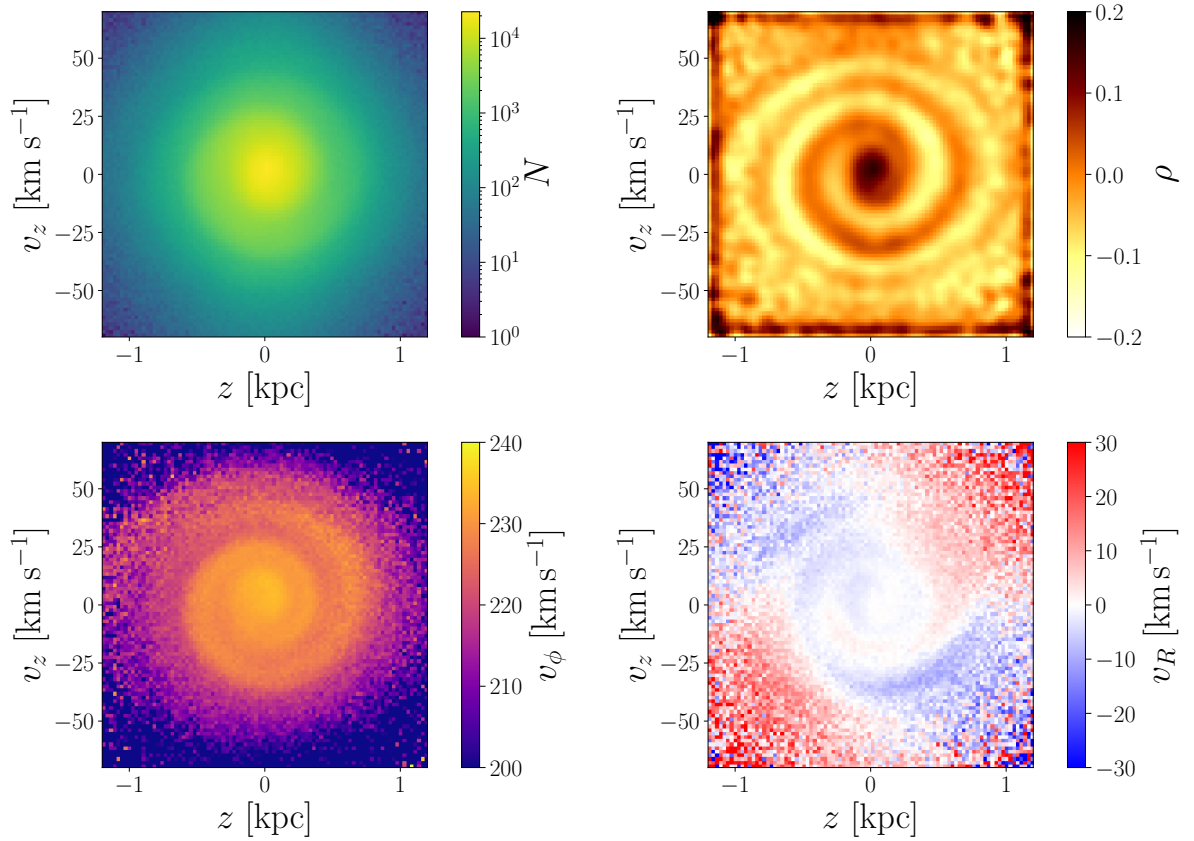


Figure 1.17: The phase spiral in the *Gaia* DR3 data. *Top left:* 2D histogram in the vertical position versus vertical velocity (z - v_z) space for the stars within 1 kpc from the Sun. *Top right:* The same map colour-coded by the overdensity. *Bottom left:* The same map colour-coded by the mean azimuthal velocity. *Bottom right:* The same map colour-coded by the mean radial velocity. The bin size is $0.027 \text{ kpc} \times 1.6 \text{ km s}^{-1}$.

1.4.2 The phase spiral

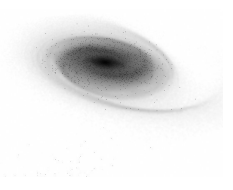
Antoja et al. (2018) discovered a phase-space structure known as the phase spiral³ in the *Gaia* DR2 data (Gaia Collaboration et al. 2018a). It is a spiral structure in the vertical position versus vertical velocity (z - v_z) space. Fig. 1.17 shows the z - v_z -space maps for the stars within 1 kpc from the Sun in the *Gaia* DR3 (Gaia Collaboration et al. 2023a) data. The top left and top right panels show the 2D histogram and local overdensity, respectively. The overdensity ρ is defined as $\rho(z, v_z) = \tilde{N}_{1.5}(z, v_z) / \tilde{N}_3(z, v_z) - 1$, where \tilde{N}_x represents the number count smoothed with a Gaussian filter of x -pixel width. Similar visualisation techniques have been employed in other studies (e.g. Laporte et al. 2019; Hunt et al. 2022; Antoja et al. 2023) to highlight spiral structure. The bottom left and bottom right panels are colour-coded by the mean azimuthal velocity and the mean radial velocity, respectively. The one-arm spiral structure is clearly observed in the top right and bottom left panels. The bottom right panel exhibits a spiral structure and a quadrupole pattern. The quadrupole pattern is due to the tilted velocity ellipsoid (Bland-Hawthorn et al. 2019).

A simple toy model gives us the physical implication of the phase spiral. Here, we modify examples in Section 4.10.2 of Binney & Tremaine (2008) and Tremaine (1999). We examine the phase-space trajectories of N particles oscillating independently in a 1D isothermal potential:

$$\Phi(z) = 2\sigma_0^2 \ln \cosh\left(\frac{z}{h}\right), \quad (1.28)$$

where $\sigma_0 = \sqrt{2\pi}h = 0.1$. Initially, the particles uniformly distributed within a circle area S , as shown in the top left panel of Fig. 1.18. The figure shows the time evolution of the distribution. Since the orbital

³ The phase spiral is alternatively referred to by various names such as phase-space spiral, phase snail and *Gaia* spiral. In this thesis, we use the “phase spiral” following Bland-Hawthorn & Tepper-García (2021).



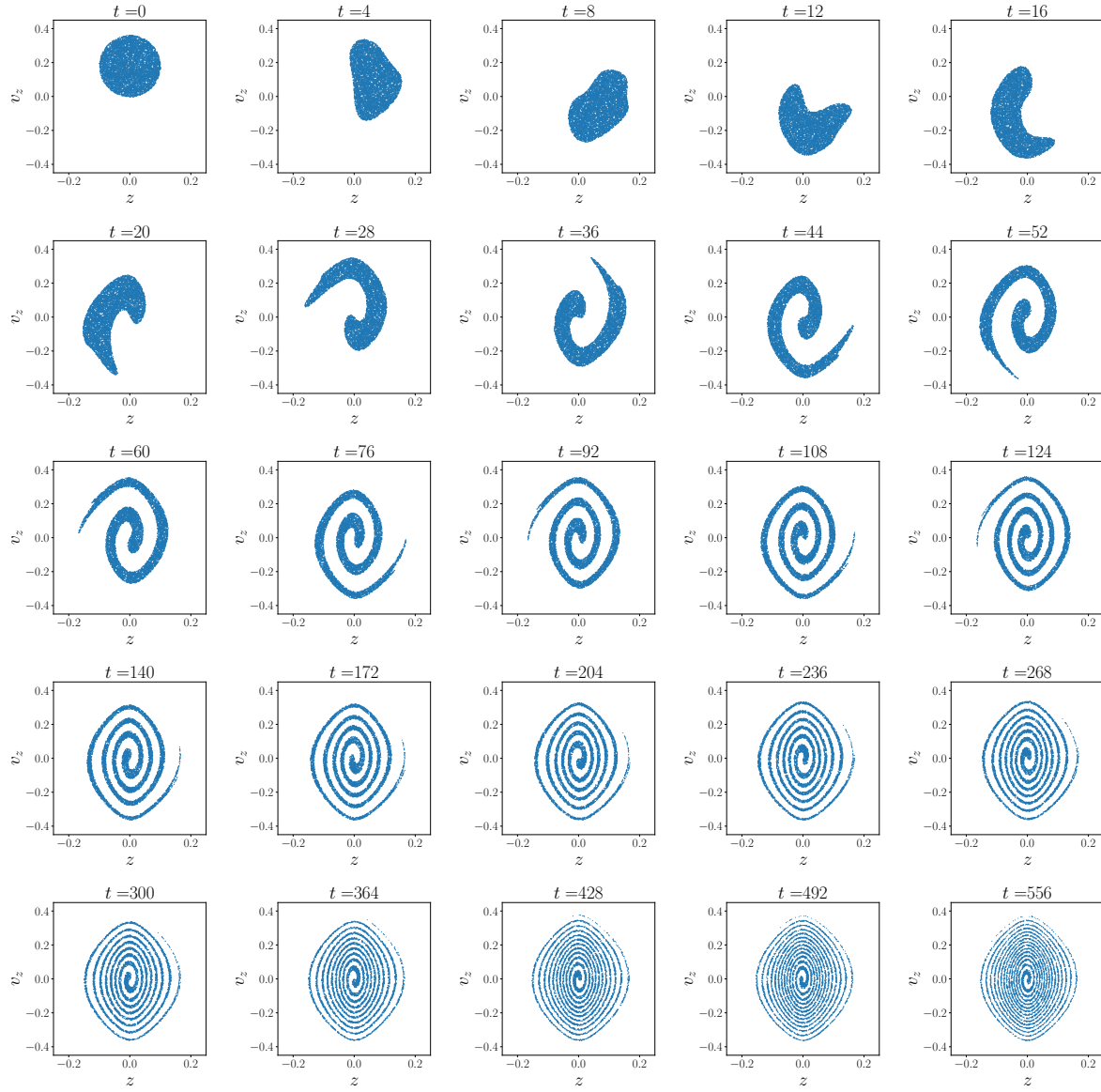


Figure 1.18: Schematic illustration of phase mixing.

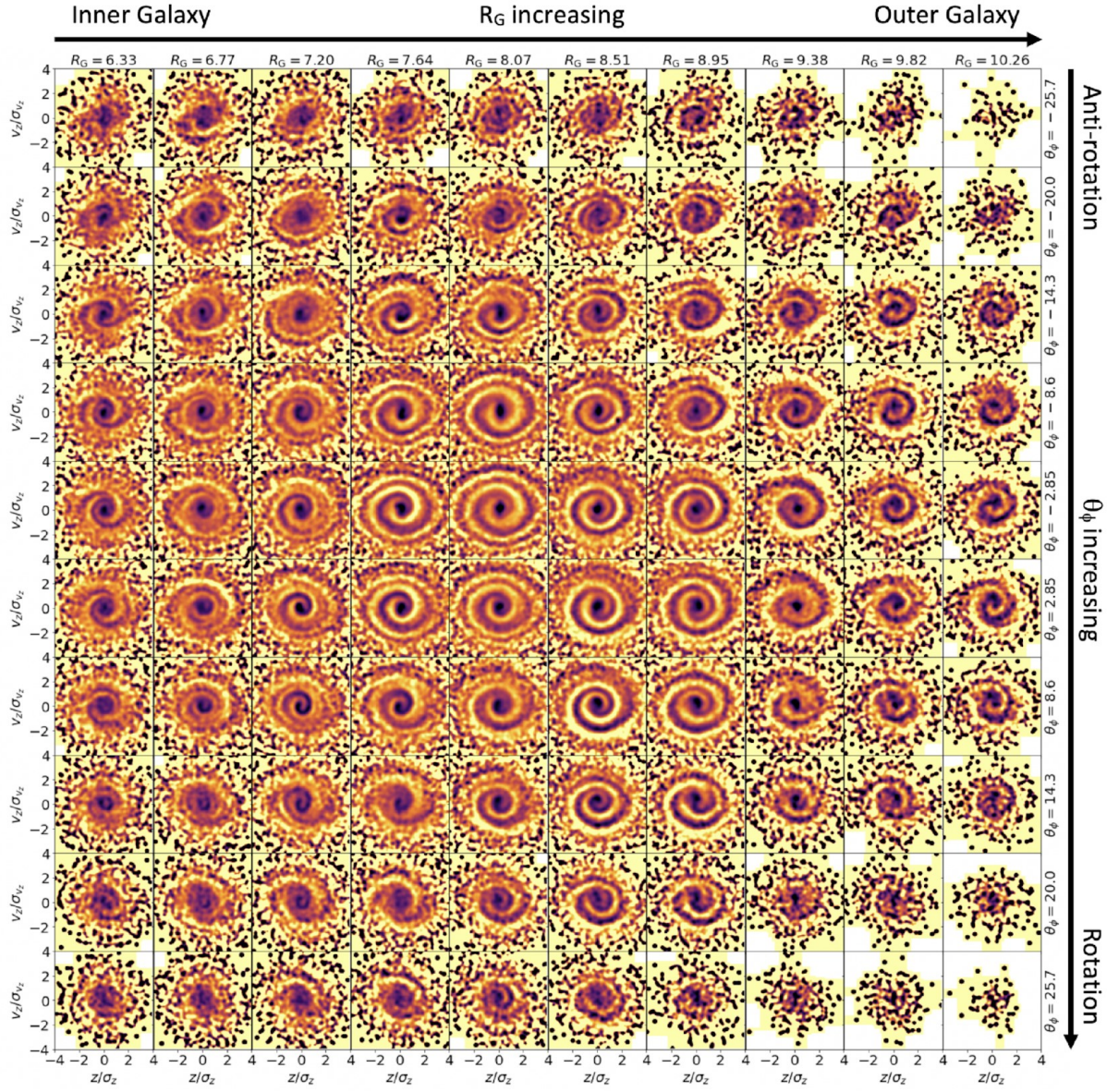
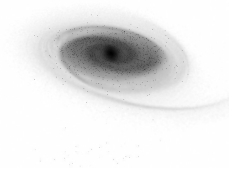


Figure 1.19: Phase spiral for the *Gaia* DR3 sample split by the guiding radius (R_g) and the azimuthal angle (θ_ϕ). This figure taken from [Hunt et al. \(2022\)](#).

period depends on the amplitude of the oscillation, the circle elongates with time and develops into a tightly wound spiral structure. The evolution of the system follows the collisionless Boltzmann equation, therefore the phase-space density f around each particle remains constant, i.e. $f = N/S$. However, the coarse-grained density \bar{f} decreases with time. As $t \rightarrow \infty$, the particles appear to smoothly distribute within an area S' in a coarse-grained view. $\bar{f} = N/S'$ is smaller than f since S' is larger than S . The physical process that involves a transition from a non-equilibrium state to a coarse-grained equilibrium like the above example is called phase mixing. The phase spiral in Fig. 1.17 represents a snapshot of incomplete phase mixing and indicates that something impulsively perturbed the Galactic disc recently ($\lesssim 1$ Gyr) and formed a non-equilibrium stellar distribution.

One of the candidates for the perturber is the Sagittarius dwarf galaxy (Sgr). It is the nearest and third heaviest satellite of the MW and has a significant impact on the dynamical evolution of the Galactic disc. Test particle simulations ([Antoja et al. 2018](#)), N -body simulations ([Laporte et al. 2019](#); [Bland-Hawthorn & Tepper-García 2021](#); [Hunt et al. 2021](#); [Bennett et al. 2022](#)) and analytical calculations ([Binney & Schönrich 2018](#); [Banik et al. 2022, 2023](#)) confirm that an external perturbation by a Sgr-like satellite excites the vertical oscillation of the disc and forms the phase spiral. Alternatively, bar buckling ([Khoperskov et al.](#)

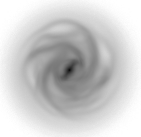


2019), a DM wake (Grand et al. 2023) and a cumulative effect of small disturbances by giant molecular clouds (Tremaine et al. 2023) are proposed for possible origins of the phase spiral.

Hunt et al. (2022) discovered another type of phase spirals. They split a solar neighbourhood sample in the *Gaia* DR3 (Gaia Collaboration et al. 2023a) by the guiding radius (R_g) and the azimuthal angle (θ_ϕ) and make the z - v_z map for each of the subsamples. Fig. 1.19 shows the z - v_z maps colour-coded by the overdensity, which is taken from Hunt et al. (2022). In the columns of $R_g \gtrsim 8$ kpc, we see one-arm phase spirals similar to the top right panel of Fig. 1.17. In the columns of $R_g \lesssim 7$ kpc, on the other hand, we see two-arm phase spirals. The one-arm and two-arm phase spirals are associated with the different oscillation modes called the bending and breathing modes. The bending (breathing) mode involves the one-arm (two-arm) phase spiral, and the south and north parts of the disc oscillate in the same (opposite) direction. Fig. 1.20 and Fig. 1.21 schematically illustrate the bending and breathing modes, respectively. We consider a 2D disc model with vertically (z direction) isothermal and horizontally (x direction) uniform distribution. We impose the following bending and breathing perturbations on the disc:

$$\Delta v_z(x) = \begin{cases} \Delta \cos(x) & \text{for bending mode,} \\ -2\Delta \tanh\left(\frac{z}{h}\right) \cos(x) & \text{for breathing mode,} \end{cases} \quad (1.29)$$

where the amplitude of the perturbation Δ is 0.1. We compute the evolution of the perturbed disc ignoring the self-gravity. Fig. 1.20 shows the time evolution of the disc for the bending mode. The panels in the left column show the density distribution in the edge-on view (x - z plane). The panels in the right column show the density distribution in z - v_z space at $x = 0$. The initial asymmetric velocity field evolves into the one-arm phase spiral in z - v_z space. Fig. 1.21 shows the same plots for the breathing mode. In this case, the velocity field symmetric about $z = 0$ evolves into the two-arm phase spiral in z - v_z space. The amplitudes of the vertical oscillations decrease with time due to vertical and horizontal phase mixing. In real galaxies and N -body models, Landau damping (Landau 1946) also contributes to the decay of the oscillations (Widrow et al. 2014).



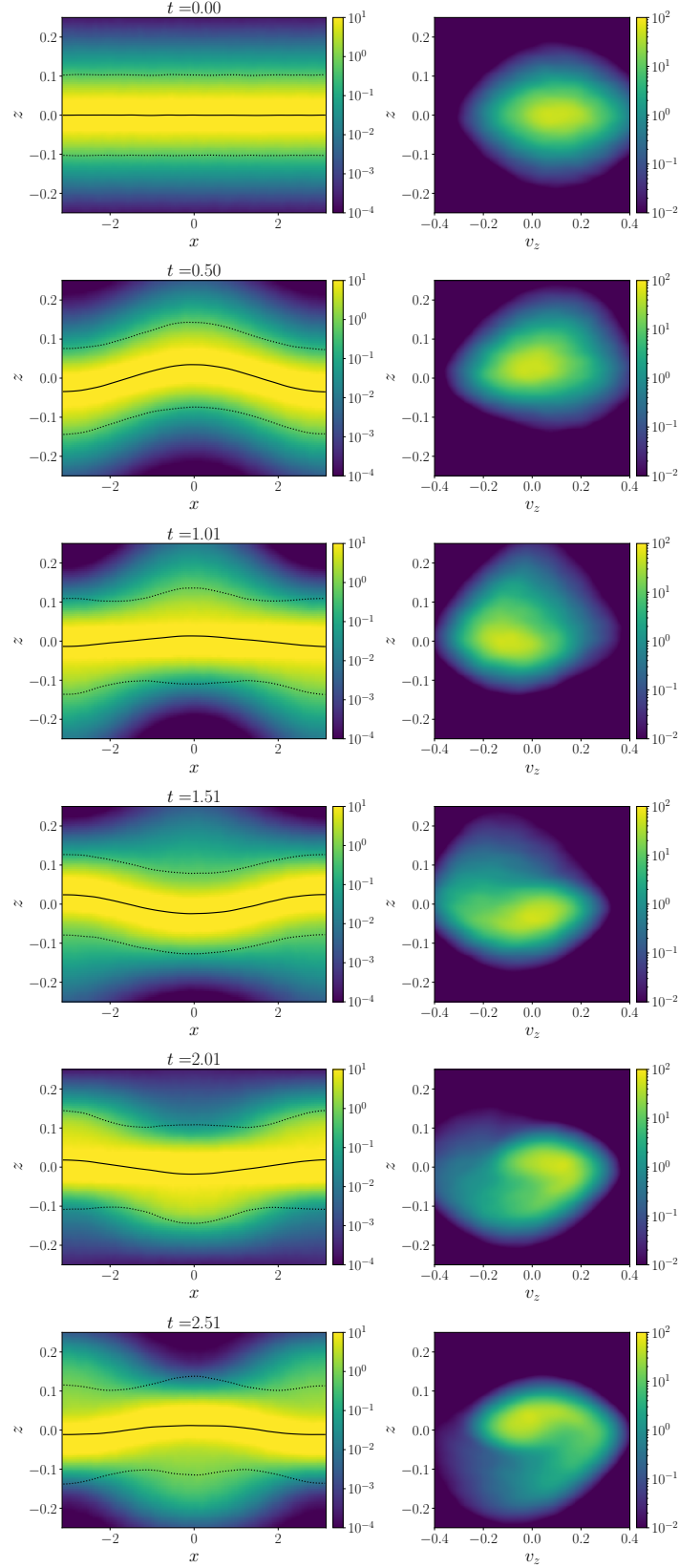
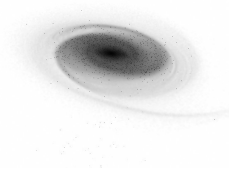


Figure 1.20: Schematic illustration of the bending motion. *Left*: Density distribution in edge-on view. The solid and dotted lines indicate \bar{z} and $\bar{z} \pm 3h_z$, respectively, where \bar{z} and h_z are the mean and standard deviation of z . *Right*: Density distribution in z - v_z space at $x = 0$.



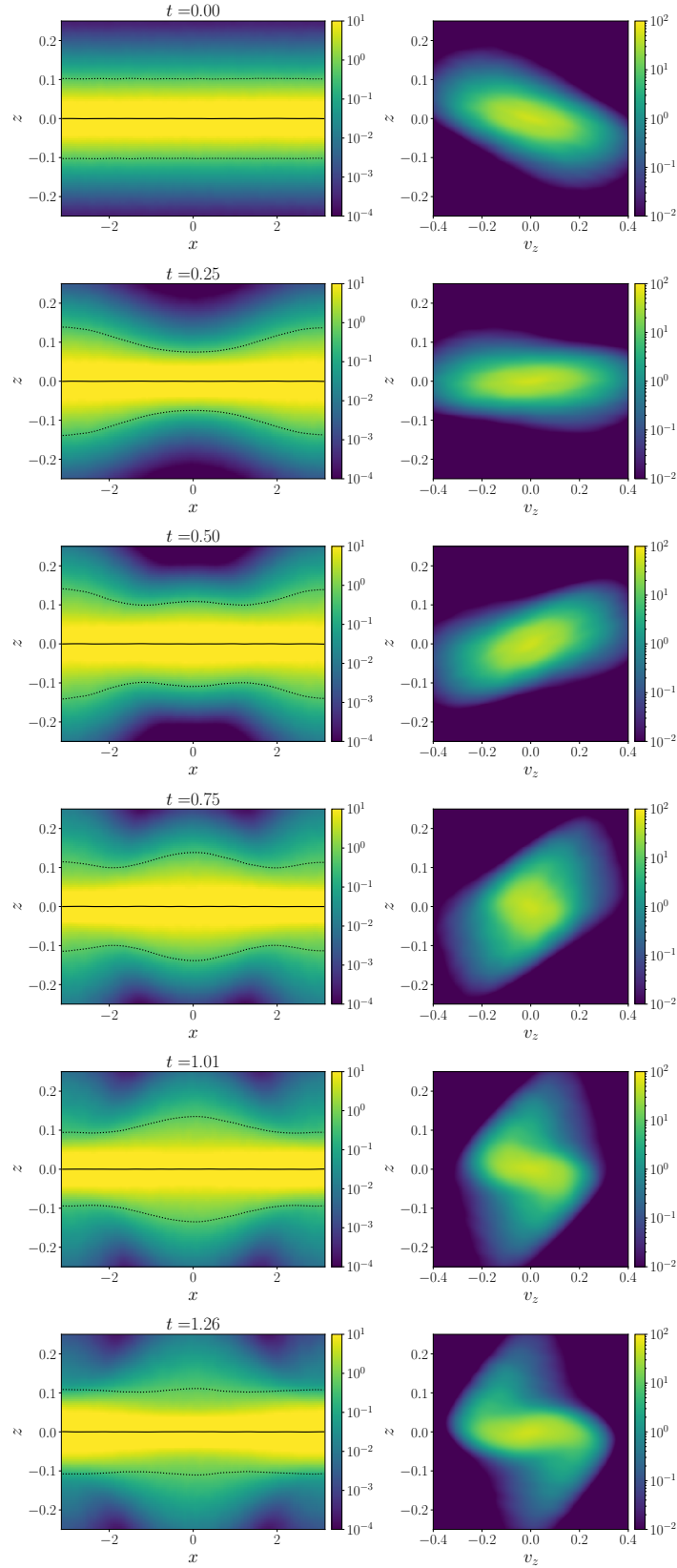


Figure 1.21: Same as Fig. 1.20, but for the breathing motion.

1.5 THEORETICAL AND NUMERICAL MODELLING OF GALAXIES

The observational data are insufficient to comprehensively understand the dynamical structure of the MW and its time evolution because they represent only a biased local snapshot of the Galaxy. As shown in Fig. 1.9, even the *Gaia* data do not provide full coverage of the MW, and the completeness almost exponentially decreases as a function of the heliocentric distance. Moreover, we face the limitation of not being able to directly trace the time evolution, as the timescale of the observations is significantly shorter than the dynamical timescale of the Galaxy. Therefore, it is essential to compare observational data with theoretical models to interpret the data and extract physical information about the dynamics of the MW.

Test particle simulations are the most commonly used tool for studies in galactic dynamics. In this approach, we numerically integrate equations of motion of test particles in given potentials. The potential is usually given as a sum of analytic functions. The advantage of this approach is that we can easily change potentials and initial conditions of the particles. The disadvantage is that we cannot consider the self-gravity of the particles and the self-consistent evolution of the potential itself. Thanks to the fine software packages for galactic dynamics such as GALPY (Bovy 2015) and AGAMA (Vasiliev 2019), we can easily perform test particle simulations and analyse the results today.

In the *Gaia* era, there have been many advancements in theoretical (analytical) studies of the dynamics of the MW. These include investigations into the resonant response of the Galactic disc to the decelerating bar (Chiba et al. 2021; Chiba & Schönrich 2021), the bar-DM halos interaction (Chiba & Schönrich 2022; Chiba 2023; Chiba & Kataria 2023; Hamilton et al. 2023), phase-space structure in the Galactic disc affected by bars resonances (Monari et al. 2017c; Binney 2018, 2020), DFs with bar/spiral arms (Monari et al. 2015, 2016a) and the response of the Galactic disc to external perturbations (Banik et al. 2022, 2023). These studies are based on mathematically formalised theories of dynamics such as Hamilton perturbation theory and linear response theory. Although we need to simplify systems in order to solve problems analytically, approximated solutions provide valuable insights into the physical behaviour of the system. Furthermore, perturbation theory is useful to analyse the stability of the system.

N -body simulations represent an *ab initio* approach to gravitational multibody problems in Newtonian mechanics. The advantage of this approach is that we can study the self-consistent evolution of the system. This approach involves numerical integrations of equations of motion of gravitationally interacting N particles. The equation of motion for the i -th particle is expressed as

$$\frac{d^2 \mathbf{x}_i}{dt^2} = \sum_{j=1, j \neq i}^N \frac{Gm_j}{|\mathbf{x}_j - \mathbf{x}_i|^3} (\mathbf{x}_j - \mathbf{x}_i), \quad (1.30)$$

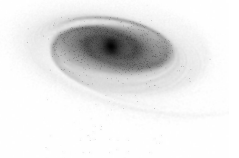
where \mathbf{x}_j and m_j are the position and mass of the j -th particle, respectively, and G is the gravitational constant. In naive implementations, the computational cost to evaluate the right hand side of Equation (1.30) is $\mathcal{O}(N)$, and we solve the equations for the N particles, hence the overall computational cost is $\mathcal{O}(N^2)$. The disadvantage of the N -body simulations is the high computational cost. Technological advances in both software and hardware have overcome this disadvantage.

We do not always need to calculate the force between each of the particle pairs. If a group of particles whose position and mass are (\mathbf{x}_j, m_j) ($j = 1 \dots N$) is sufficiently far from a position \mathbf{x} , i.e. the distance between \mathbf{x} and the centre of the group is sufficiently larger than the spatial extent of the group, we can approximately replace the cumulative force,

$$\mathbf{F}(\mathbf{x}) = \sum_{j=1}^N \frac{Gm_j}{|\mathbf{x}_j - \mathbf{x}|^3} (\mathbf{x}_j - \mathbf{x}), \quad (1.31)$$

by the gravitational force from the centre of mass,

$$\begin{aligned} \mathbf{F}'(\mathbf{x}) &= \frac{GM}{|\mathbf{X} - \mathbf{x}|^3} (\mathbf{X} - \mathbf{x}), \\ \mathbf{X} &= \frac{\sum_{j=1}^N m_j \mathbf{x}_j}{\sum_{j=1}^N m_j} \\ M &= \sum_{j=1}^N m_j \end{aligned} \quad (1.32)$$



Such an approximation is efficiently given by the tree-code developed by [Barnes & Hut \(1986\)](#). In this scheme, we divide the simulation box into a hierarchical tree structure. The root node represents the whole simulation box, and the root node is divided into eight equal boxes (child nodes). Each child node is further divided into eight nodes. This process is repeated if a node contains more than one particle. If a particle is sufficiently far from a node, we can approximate the cumulative force from the node by the gravitational force from the node's centre of mass. The tree-code reduces the computational cost from $\mathcal{O}(N^2)$ to $\mathcal{O}(N \log N)$. The tree-code can be applied to N -body simulations of collisionless systems. Since the lifetimes of typical disc galaxies such as the [MW](#) are much shorter than the relaxation time, galaxies are considered to be collisionless systems.⁴ Therefore, the tree-code is widely used in N -body simulations of galaxies.

GRAvity Pipe (GRAPE) was a major hardware breakthrough in N -body simulations ([Sugimoto et al. 1990](#); [Makino & Taiji 1998](#)). It is a special-purpose computer for accelerating gravitational force calculations in N -body simulations. Using a pipeline architecture, GRAPE achieved speedups of orders of magnitude compared with general-purpose computers of the time. Later, several generations of GRAPE series computers were developed and used for particle simulations in various fields of astrophysics.

In the 2000s, graphics processing units (GPUs) started to be used as accelerators of N -body simulations (e.g. [Portegies Zwart et al. 2007](#); [Hamada & Iitaka 2007](#); [Elsen et al. 2007](#)). Although GPUs were originally developed for graphics processing as the name represents, they can be used for non-graphic purposes because they are designed to perform many simple calculations in parallel. More recently, some studies (e.g. [Nakasato 2012](#); [Bédorf et al. 2012, 2014](#); [Miki & Umemura 2017](#)) used GPUs for the tree-code. For the simulations in this thesis, we have used BONSAI developed by [Bédorf et al. \(2012, 2014\)](#), which is currently one of the best GPU-based tree-codes. Another example of the GPU-based high-performance codes is GOTHIC ([Miki & Umemura 2017](#)).

Fast codes which work on highly parallel processors are important for two reasons. First, it enables us to perform large-scale simulations. To compare stellar distributions in observation data and those in simulations, high-resolution simulations with large numbers of particles are required. Second, fast codes enable us to perform fast parameter surveys. N -body systems evolve non-linearly, so we cannot predict final states directly from initial conditions. We need to try initial conditions with many different parameters to find the best ones to reproduce the target system. Fast codes are essential for efficient parameter surveys. In this thesis, we discuss the dynamical structure of the [MW](#) by qualitatively and quantitatively comparing the *Gaia* data and the billions of particle N -body simulations performed with the BONSAI code ([Bédorf et al. 2012, 2014](#)).

1.6 THIS THESIS

1.6.1 Objective of this thesis

The focus of this thesis is closely aligned with the field of galactic seismology (e.g. [Widrow et al. 2012](#); [Bland-Hawthorn & Tepper-García 2021](#); [Tepper-García et al. 2022](#); [García-Conde et al. 2023](#)), which is a subcategory within galactic dynamics that investigates the impacts of internal and external perturbations on galaxies. According to [Bland-Hawthorn & Tepper-García \(2021\)](#), the term was initially introduced by [Iye \(1985\)](#) as an analogy to asteroseismology. Early studies of galactic seismology involved the linear analysis of the stable and unstable modes in the galactic discs (e.g. [Iye 1978](#); [Aoki et al. 1979](#)). One of the goals of galactic seismology is to gain insights into the structure of galaxies by comparing observations with theoretical models. The astrometry data from *Gaia* provides us with a new opportunity to investigate the dynamical structure of the [MW](#) in terms of galactic seismology. Furthermore, we can perform high-resolution N -body simulations using the GPU-based codes to construct theoretical counterparts of the [MW](#). The overarching objective of this thesis is to provide insights into the structure of the [MW](#) and its time evolution by theoretically explaining the relations between phase space substructures in the Galactic disc and internal and external perturbations.

⁴ The relaxation time is estimated by

$$t_{\text{relax}} \simeq \frac{0.1N}{\ln N} t_{\text{cross}},$$

where N is the number of stars and t_{cross} is the crossing time ([Binney & Tremaine 2008](#)). Galaxies have $N \sim 10^{11}$ stars and the crossing time is $t_{\text{cross}} \sim 100$ Myr, hence $t_{\text{relax}} \sim 10^7$ Gyr. This is sufficiently longer than the age of the Universe.

1.6.2 Structure of this thesis

Chapter 2 describes two N -body simulations of MW-like galaxies. The first one is an isolated disc galaxy model performed by Fujii et al. (2019). The second one is a MW model perturbed by a Sgr-like satellite galaxy. Both simulations are performed with the BONSAI code (Bédorf et al. 2012, 2014). The selection and analysis of the *Gaia* data are also described in this chapter.

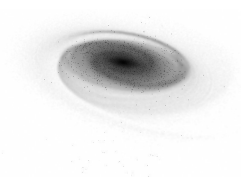
In Chapter 3, we investigate the origin of the substructures in the v_R - v_ϕ space distribution of the solar neighbourhood stars. We find a Hercules-like stream in the final snapshot of the isolated model. We clarify the relation between the substructure and bar resonances by analysing the orbital properties of the stars in the stream. We demonstrate that the R - v_ϕ ridges can be also explained by bar resonances. Finally, we estimate the bar's pattern speed in the MW from the relation between the ridges and resonances.

In Chapter 4, we investigate the time evolution and spatial variation of the velocity-space distribution. We use the Kullback-Leibler divergence (KLD) to quantitatively evaluate the similarities of the velocity-space distributions in the N -body model and that of the solar neighbourhood in the *Gaia* data. The KLD analysis shows that the velocity-space distribution evolves with time and that it is related to the bar evolution. We discuss where we frequently detect velocity-space distributions with small KLDs (high similarities) in the N -body model.

Chapter 5 focuses on spiral arms and the breathing motion induced by them. We evaluate the amplitude and direction of the breathing motion in the MW disc using the *Gaia* data. We find a compressing breathing motion along the Local arm. We investigate the time evolution of the breathing motion and its relation with the spiral arms in the isolated N -body model. Comparing the observed and simulated breathing motions, we discuss the evolution stages of the spiral arms in the MW.

In Chapter 6, we analyse the perturbed MW model. The external perturbation by the Sgr-like satellite excites the bending oscillation of the galactic disc and tidally induces spiral arms in the disc. We show that characteristic phase-space structures appear due to the two structural changes in the disc. Especially, the tidally induced spiral arms excite the strong breathing mode of the disc and form the two-arm phase spiral in the z - v_z space, whereas the bending mode directly excited by the dwarf's perturbation forms the one-arm phase spiral. We investigate the time evolution of the bending and breathing modes and their relation with the phase spiral.

Conclusions and future prospects are given in Chapter 7.



In this thesis, we use N -body models of isolated and perturbed MW-like disc galaxies. Here, we describe the details of the simulations and the general properties about the dynamical structures of the models.

2.1 ISOLATED MODEL

2.1.1 Initial condition and simulation

We use the isolated MW model MWa5B from Fujii et al. (2019), which is the fiducial model in their study. They selected this model as the fiducial model because it shows the best agreement with recent observations. In Appendix A, we show the disc and bulge properties of MWa5B and other models in Fujii et al. (2019) and describe their model selection method. This simulation stands out as one of the most highly resolved N -body simulations performed in prior research. The total number of the particles of this model is 5.1 billion. This large number of particles enables us to perform a direct comparison of simulation results with the *Gaia* data. An additional advantage of this model is the high time resolution of the particle data output. The snapshots of disc and bulge particles were stored every ~ 10 Myr. This temporal granularity allows for the direct reconstruction of individual star orbits from the snapshots.

Fujii et al. (2019) made the initial condition for the galaxy using GALACTICS (Kuijken & Dubinski 1995; Widrow & Dubinski 2005; Widrow et al. 2008). The model comprises DM halo, classical bulge and disc components. To prevent numerical heating of the disc, equal-mass particles of $\sim 175M_\odot$ were employed. The numbers of the particles for the halo, bulge and disc are 4.9 billion, 30 million and 208 million, respectively. Table 2.1 summarises the parameters for this model.

The DM halo follows Navarro-Frenk-White (NFW; Navarro et al. 1997) profile:

$$\rho_h(r) = \frac{\rho_{h0}}{(r/a_h)(1+r/a_h)^2}, \quad (2.1)$$

where a_h and ρ_{h0} are the scale radius and the characteristic density, respectively. a_h is set to 10 kpc. $\rho_{h,0}$ is determined through the characteristic velocity dispersion $\sigma_h = (4\pi G a_h^2 \rho_{h0})^{1/2} = 420 \text{ km s}^{-1}$ where G is the gravitational constant. The truncation parameter (Widrow & Dubinski 2005) is set to $\epsilon_h = 0.85$. This value results in an outer halo radius close to the MW' virial radius, $r_{\text{vir}} \sim 282 \pm 30 \text{ kpc}$ (Bland-Hawthorn & Gerhard 2016). The rotation fraction α_h dictates the spin of the halo. This parameter represents the fraction of particles rotating in the same direction as the disc. Thus, if α_h equals 0.5, the halo exhibits no rotation. Bars embedded in halos without spin significantly decelerate and become long due to angular momentum transfer from the bars to the halo (Athanasoulas 2002). In contrast, in a spinning halo, where angular momentum transfers are suppressed, bars become faster and shorter (Fujii et al. 2018, 2019). By tuning α_h , we can control the bar length and pattern speed. The chosen value of $\alpha_h = 0.8$ results in a pattern speed and bar length consistent with the observed values (Bland-Hawthorn & Gerhard 2016).

The classical bulge follows the Hernquist profile (Hernquist 1990):

$$\rho_b(r) = \frac{\rho_{b0}}{(r/a_b)(1+r/a_b)^3}. \quad (2.2)$$

The scale radius a_b and the characteristic velocity dispersion $\sigma_b = (4\pi G a_b^2 \rho_{b0})^{1/2}$ and the truncation parameter ϵ_b are set to 0.75 kpc and 330 km s^{-1} and 0.99, respectively. The rotation fraction α_b is set to 0.5, indicating that the classical bulge does not initially rotate.

The density distribution of the disc is given by a radially exponential and vertically isothermal profile:

$$\rho_d(R, z) = \rho_{d0} \exp\left(-\frac{R}{R_d}\right) \text{sech}^2\left(\frac{z}{z_d}\right). \quad (2.3)$$

The five parameters: scale radius R_d , the scale height z_d , the total mass M_d , the disc truncation radius R_{out} and the sharpness of truncation δR_{out} characterize the model. They are set to $R_d = 2.3 \text{ kpc}$, $z_d = 0.2 \text{ kpc}$,

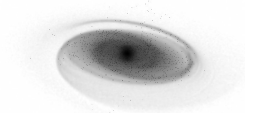


Table 2.1: Initial condition parameters for the isolated model

DM Halo	
Scale radius a_h	10 kpc
Characteristic velocity σ_h	420 km s ⁻¹
Truncation parameter ϵ_h	0.85
Rotation fraction α_h	0.8
Bulge	
Scale radius a_b	0.75 kpc
Characteristic velocity σ_b	330 km s ⁻¹
Truncation parameter ϵ_b	0.99
Rotation fraction α_b	0.5
Disc	
Scale radius R_d	2.3 kpc
Scale height z_d	0.2 kpc
Disc mass M_d	$3.61 \times 10^{10} M_\odot$
Disc truncation radius R_{out}	30 kpc
Sharpness of the truncation δR_{out}	0.8 kpc
Central velocity dispersion σ_{R0}	94 km s ⁻¹

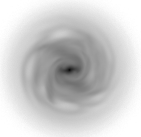
$M_d = 3.61 \times 10^{10} M_\odot$, $R_{out} = 30$ kpc and $\delta R_{out} = 0.8$ kpc, respectively. The radial velocity dispersion follows $\sigma_R(R)^2 = \sigma_{R0}^2 \exp(-R/R_d)$, with $\sigma_{R0} = 94$ km s⁻¹.

The simulations were performed using the parallel GPU tree-code, BONSAI (Bédorf et al. 2012, 2014) with a GPU cluster, Piz Daint computer at CSCS in Switzerland. The softening length was configured to 0.01 kpc, and the opening angle was set to 0.4. The shared time-step is set to 0.6 Myr. The simulation was performed for 10 Gyr, and the snapshots were recorded every ~ 10 Myr.

2.1.2 Structures of the disc and bulge

Fig. 2.1 shows the density distribution in the x - y , x - z and y - z planes for fifteen different snapshots. The density is shown in a logarithmic colour scale. The bar's major axis is aligned with the x -axis. The galaxy rotates clockwise in the x - y plane. The simulation starts from an axisymmetric disc without any structures. At $t \sim 2$ Gyr, a bar forms. At the almost same time spiral arms also appear. The spiral structure is most prominent at ~ 5 Gyr. After $t \sim 6$ Gyr, they become faint due to the dynamical heating of the disc. The simulation continues up to 10 Gyr. As can be seen in the side-on panels, the vertical structure of the bulge also evolves with time. The bulge is initially spherical. After the bar formation, the bulge gradually develops the BP shape. In this simulation, the bar does not show the buckling, and the vertical resonance forms the BP bulge.

In Fig. 2.2, the rotation curve of the model at $t = 10$ Gyr is presented. For comparison, we also plot the rotation curve model of the MW estimated by Sofue (2017b). The orange shaded band indicates the observationally estimated circular velocity range of $v_c = 238 \pm 15$ km s⁻¹ at the Sun's radius (Bland-Hawthorn & Gerhard 2016). The N -body model shows a flat rotation curve at $R \gtrsim 10$ kpc, and it is consistent with the observed rotation curve. At $R = 8$ kpc, the circular velocity is $v_c \sim 241$ km s⁻¹, which almost perfectly fits the observational estimation of the circular velocity at the Sun's radius in the MW. Although the rotation curve is less similar to that of the observation in the inner galaxy ($R \lesssim 5$ kpc) than in the outer galaxy, we do not discuss this difference in detail because the observed circular velocity in this region may be biased due to the non-circular gas motion induced by the bar (Fux 1999; Baba et al. 2010).



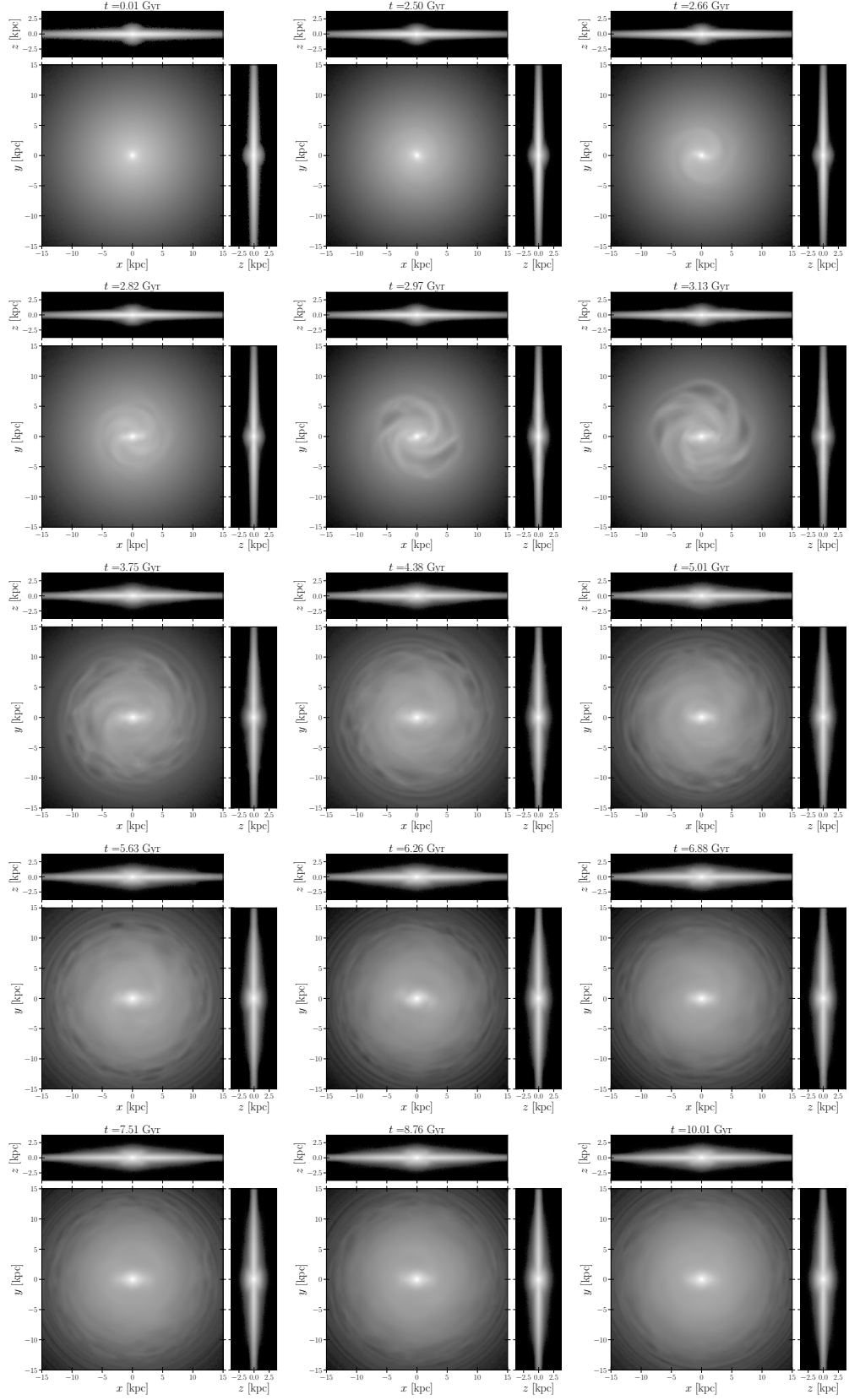
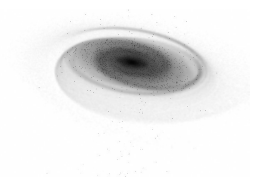


Figure 2.1: Time evolution of the galactic disc in the isolated model. The density distribution in the x - y , x - z and y - z planes are shown with logarithmic scale for the fifteen snapshots. The bar's major axis is aligned with the x -axis.



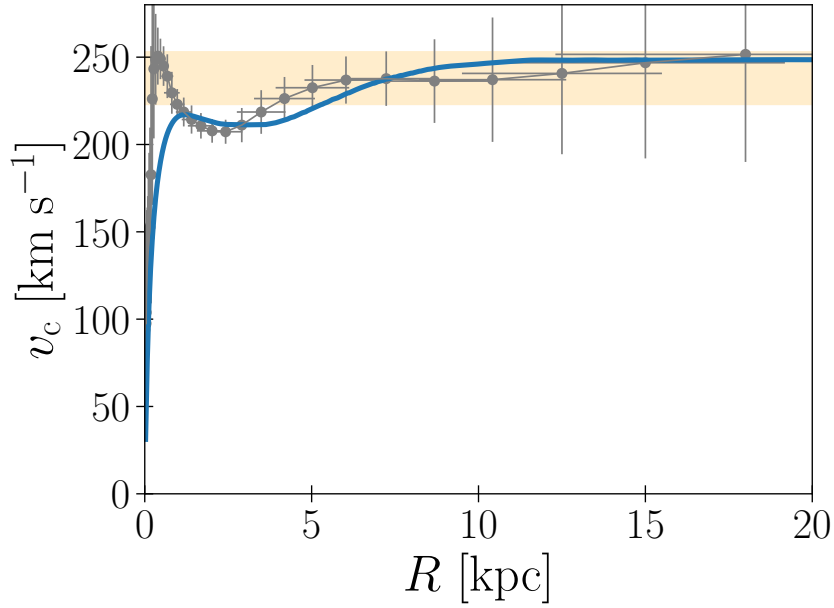


Figure 2.2: The rotation curves of the *N*-body model and the MW. The blue line shows the rotation curve of the *N*-body model at $t = 10$ Gyr. The grey dots show the MW’s rotation curve (Sofue 2017b). The orange shaded region indicates the observationally estimated circular velocity at the Sun’s radius (Bland-Hawthorn & Gerhard 2016).

We determine the bar’s pattern speed and amplitude using the Fourier decomposition as done in Fujii et al. (2019). We divide the galactic disc into annuli with a width of 1 kpc, and then Fourier decompose the surface density $\Sigma(R, \phi)$ in each annulus:

$$\frac{\Sigma(R, \phi)}{\Sigma_0(R)} = \sum_{m=-\infty}^{\infty} A_m(R) \exp\{im[\phi - \phi_m(R)]\}, \quad (2.4)$$

where $\Sigma_0(R)$, $A_m(R)$ and $\phi_m(R)$ are the azimuthally averaged surface density, amplitude and phase angle of the m -th Fourier mode, respectively. We define $\phi_2(R)$ averaged in $R < 3$ kpc as the angle of the bar in the snapshot (see also Fujii et al. 2019). The bar’s strength can be evaluated by the $m = 2$ Fourier amplitude, A_2 . Fig 2.3 shows the pattern speed and amplitude of the bar as functions of time. The pattern speed Ω_b is calculated as the difference of the bar angles between two consecutive snapshots. As bar amplitudes, we show $A_2(R)$ at $R = 1, 2$ and 3 kpc. The Fourier amplitude A_2 starts to increase at $t \sim 2.5$ Gyr, which corresponds to the bar formation time. The bar grows rapidly until $t \sim 3$ Gyr. From $t \sim 3$ Gyr to $t \sim 7$ Gyr, the amplitude oscillates with time, as the bar and the DM halo interact with each other (Okamoto et al. 2015; Chiba & Schönrich 2022). The strong oscillation at $R = 3$ kpc is possibly due to the influences of the spiral arms. This radius is close to the half length of the bar, and it is difficult to decouple the bar and spiral arms in the Fourier analysis. In this epoch, the bar’s pattern speed decreased from $\sim 60 \text{ km s}^{-1} \text{ kpc}^{-1}$ to $\sim 45 \text{ km s}^{-1} \text{ kpc}^{-1}$ due to the angular momentum transfer from the bar to the DM halo. After $t \sim 7$ Gyr, the bar’s pattern speed saturated at $\sim 45 \text{ km s}^{-1} \text{ kpc}^{-1}$. In this phase, the pattern speed still oscillates with time although the oscillation amplitude is smaller than that before $t \sim 7$ Gyr. This is mainly due to the bar-spiral interaction (Sellwood & Sparke 1988; Baba 2015; Hilmi et al. 2020).

In Chapter 3 and Chapter 4, we mainly use snapshots in later epochs ($t \gtrsim 8$ Gyr). In this epoch the spiral arms are already weak due to the dynamical heating of the disc, and we can focus on the perturbation of the bar. In other words, the influence of the spiral arms is underestimated. However, this underestimation does not significantly affect the conclusions of the two chapters dealing with the kinematics of stars in the solar neighbourhood, because the Sun is located in the inter-arm region of the major arms of the MW and the local stellar motion is not significantly affected by the spiral arms.

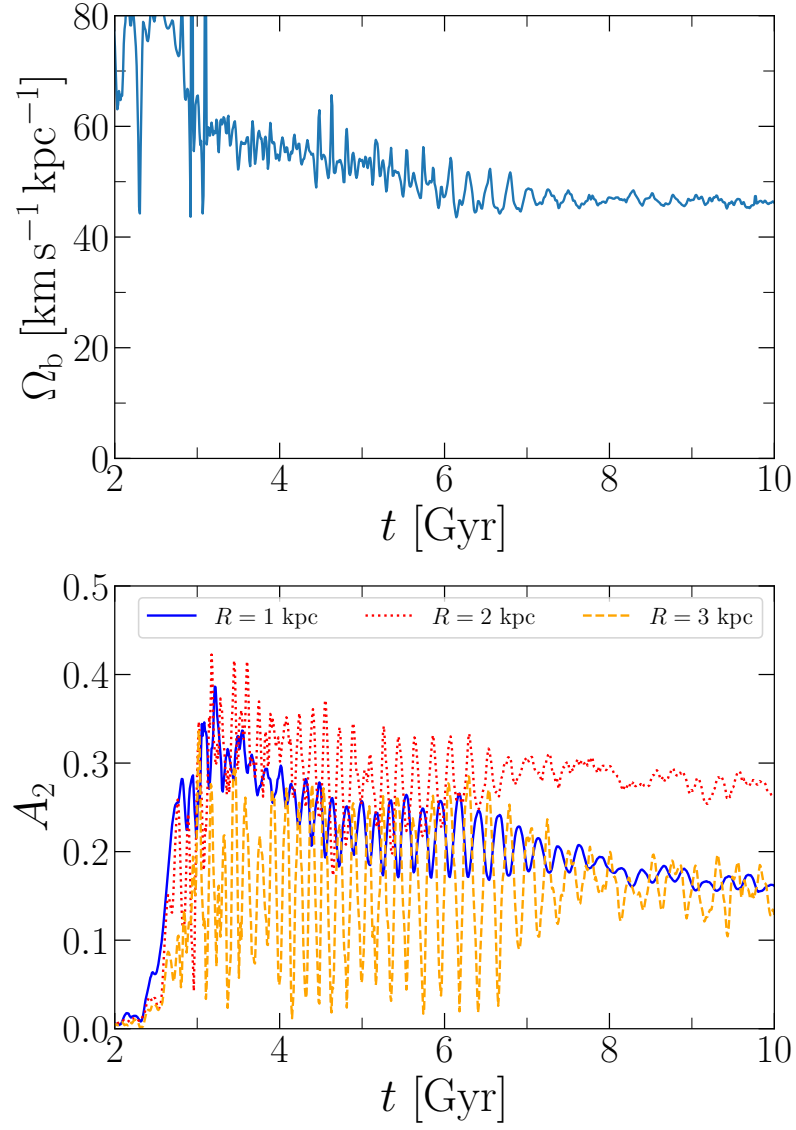
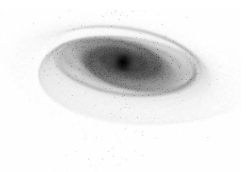


Figure 2.3: Time evolution of the bar. *Top:* Pattern speed. *Bottom:* Fourier amplitude $A_2(R)$ at $R = 1, 2$ and 3 kpc.



2.2 PERTURBED MODEL

本節については、5年以内に雑誌などで刊行予定のため、非公開。

2.3 GAIA DATA

We briefly describe the selection and analysis of the *Gaia* data. In this thesis, the primary dataset is selected from the *Gaia*'s latest data release, DR3 (Gaia Collaboration et al. 2023a). In Chapter 3 and Chapter 4 which focus on the velocity-space distribution of the solar neighbourhood stars, we use the data from the *Gaia* DR2 (Gaia Collaboration et al. 2018a) and EDR3 (Gaia Collaboration et al. 2021), respectively. The qualitative and quantitative differences between the previous and latest data releases do not affect the conclusions because the astrometric data quality and completeness are sufficiently high even in the previous data releases in the solar neighbourhood.

From the *Gaia* DR3 catalogue, we select the stars that meet the following criteria.

1. The relative error in parallax is less than 20%.
2. The renormalised unit weight error (ruwe) is less than 1.4.¹
3. The radial velocity is not null.
4. The parameters required for the zero-point correction of the parallax (Lindgren et al. 2021) are available.

Listing 2.1 shows the Astronomical Data Query Language (ADQL) query to retrieve the data in the *Gaia* ESA Archive.² Our resulting sample comprises 26,218,611 stars.

Listing 2.1: ADQL query to select the *Gaia* DR3 samples with high quality astrometric solutions and small parallax errors.

```
SELECT g.*
FROM gaiadr3.gaia_source AS g
WHERE (g.parallax_over_error > 5.)
AND (g.ruwe < 1.4)
AND (g.radial_velocity IS NOT NULL)
AND (g.phot_g_mean_mag IS NOT NULL)
AND (g.nu_eff_used_in_astrometry IS NOT NULL)
```

We use $1/\varpi$ as a distance to a star from the Sun, where ϖ is the zero-point-corrected parallax (Lindgren et al. 2021). We convert the heliocentric coordinate to the Galactocentric coordinate using `astropy.coordinates` from `ASTROPY PYTHON` package (Astropy Collaboration et al. 2013, 2018, 2022). Here, we assume the following values for the solar position and velocity: the distance of the Sun from the Galactic centre $R_0 = 8.277$ kpc (GRAVITY Collaboration et al. 2022), the vertical distance from the mid-plane $z_0 = 0.0208$ kpc (Bennett & Bovy 2019), the total tangential velocity with respect to the Galactic centre $v_{\phi,\odot} = 251.5$ km s⁻¹ (Reid & Brunthaler 2020; GRAVITY Collaboration et al. 2022) and the solar velocity with respect to the LSR ($U_\odot, V_\odot, W_\odot$) = (11.1, 12.24, 7.25) km s⁻¹ (Schönrich et al. 2010). The assumed parameters are summarized in Table 2.2.

¹ This quality cut is recommended to deal with spurious astrometric solutions (Gaia Collaboration et al. 2021; Fabricius et al. 2021).

² <https://gea.esac.esa.int/archive/>

Table 2.2: Assumed parameters for the solar position and motion

Parameters	Values	References
Distance from the Galactic centre R_0	8.277 kpc	(1)
Distance from the mid-plane z_0	0.0208 kpc	(2)
Tangential velocity w.r.t. the Galactic centre $v_{\phi,\odot}$	251.5 km s ⁻¹	(3), (1)
Velocity w.r.t. the LSR ($U_\odot, V_\odot, W_\odot$)	(11.1, 12.24, 7.25) km s ⁻¹	(4)

- (1) [GRAVITY Collaboration et al. \(2022\)](#)
(2) [Bennett & Bovy \(2019\)](#)
(3) [Reid & Brunthaler \(2020\)](#)
(4) [Schönrich et al. \(2010\)](#)



TRIMODAL STRUCTURE OF HERCULES STREAM EXPLAINED BY ORIGINATING FROM BAR RESONANCES

3.1 INTRODUCTION

The astrometry data of the *Gaia* provide snapshots of the stars in the Galactic potential and we here aim to obtain information on the dynamical structure of the *MW* by investigating the phase-space distributions of its stars. In this context, velocity-space structures of the solar neighbourhood have previously been repeatedly studied (e.g. Kalnajs 1991; Dehnen 1998, 1999b), but mainly under analytical or numerical approximations which we here drop.

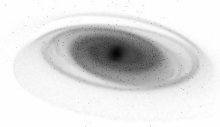
In Fig. 3.1, we present the distribution of radial velocities, v_R , versus angular velocities, v_ϕ , of stars observed with *Gaia* (similar to Figure 22 in Gaia Collaboration et al. 2018b). In this map, we see several arch-shaped over-densities with such as the so-called ‘horn’ near $(v_R, v_\phi) \sim (-50, 220) \text{ km s}^{-1}$ (Monari et al. 2017a; Fragkoudi et al. 2019) and the so-called ‘hat’ near $(v_R, v_\phi) \sim (\pm 50, > 250) \text{ km s}^{-1}$ (e.g. Hunt & Bovy 2018; Hunt et al. 2019). The most prominent structure is called the ‘Hercules’ stream, and is located between $(v_R, v_\phi) \sim (100, 200) \text{ km s}^{-1}$ and $(v_R, v_\phi) \sim (-70, 170) \text{ km s}^{-1}$.

Dehnen (1998) identified the Hercules stream as *U*-anomaly from the *Hipparcos* data (ESA 1997; Perryman et al. 1997), and *Gaia* DR2 (Gaia Collaboration et al. 2018a,b) revealed further detailed structures within. *Gaia* DR2 showed for the first time the trimodal structure of the Hercules stream, which is composed of three sub-streams at $v_\phi \sim 220, 200$ and 180 km s^{-1} (Gaia Collaboration et al. 2018b; Ramos et al. 2018; Trick et al. 2019; Li & Shen 2020). Although we refer to the bottom stream in Fig. 3.1 as ‘Hercules 3’, it is identical to a moving group, HR 1614 (Eggen 1971, 1978; Kushniruk et al. 2020).

Soon after the first discovery of the Hercules stream, a scenario on its origin was proposed by Dehnen (1999b, 2000). They calculated the evolution of the stellar phase space distribution in the simple $m = 2$ bar potential (where m indicates the azimuthal Fourier mode), and then argued that stars trapped in the 2:1 OLR of the bar can create moving groups in the solar neighbourhood. The exact position of the formed structure in phase space depends on the location of the OLR and the OLR position depends in turn on the pattern speed of the bar (Ω_b). Hence, to reproduce the observed features, this scenario requires a fast rotating bar to bring the 2:1 OLR around 8 kpc, i.e. $\Omega_b/\Omega_0 = 1.85$ (where Ω_0 is the local circular frequency); this corresponds to $\Omega_b = 53 \pm 3 \text{ km s}^{-1} \text{ kpc}^{-1}$ (see also Fux 2001; Minchev et al. 2007, 2010; Antoja et al. 2014). Such a fast ($\Omega_b \sim 50 \text{ km s}^{-1} \text{ kpc}^{-1}$) bar model is also favoured by test particle integration in a more realistic *MW* potential that was constructed from an *N*-body snapshot (Fragkoudi et al. 2019).

On the other hand, recent observations suggests slower pattern speeds of the bar. Combining data from *Gaia* DR2 and further surveys, both Sanders et al. (2019) and Bovy et al. (2019) estimated a pattern speed of $\Omega_b = 41 \pm 3 \text{ km s}^{-1} \text{ kpc}^{-1}$, and Clarke et al. (2019) estimated $\Omega_b = 37.5 \text{ km s}^{-1} \text{ kpc}^{-1}$. Recent measurements of the bar length also support a slow bar model. The measured ratio of the corotation radius (R_{CR}) to the bar length (R_b) $R_{CR}/R_b = 1.2 \pm 0.2$ for external galaxies (Aguerri et al. 2003, 2015). The bar length of $R_b = 5.0 \pm 0.2 \text{ kpc}$ in the *MW* (Wegg et al. 2015), therefore, suggests the corotation radius of $R_{CR} \sim 5\text{--}7 \text{ kpc}$ or the pattern speed of $\Omega_b \sim 34\text{--}47 \text{ km s}^{-1} \text{ kpc}^{-1}$. In addition, such slow and long bar is also supported by the dynamical modelling of bulge stars (Portail et al. 2017) and gas kinematics (Sormani et al. 2015; Li et al. 2016). With such a slow pattern speed, the 2:1 OLR should be located further than 8 kpc.

The slow and long bar model enhanced the studies of the Hercules stream’s origin, and new scenarios have been suggested. Most of them agree with the concept that resonant orbits due to non-axisymmetric structures, such as a bar and/or spiral arms, create the moving groups in the solar neighbourhood revealed by *Gaia* DR2. One of the new scenarios is the bar’s CR scenario. Pérez-Villegas et al. (2017) integrated orbits of test particles in a gravitational field constructed from a self-consistent *N*-body model of the *MW* to match observational data using the Made-to-Measure (M2M) method (Portail et al. 2017), and then proposed that the Hercules-like stream can be made of stars orbiting around Lagrangian points of the bar. These stars move outward from the bar’s CR radius to visit the solar neighbourhood. In this study, they assumed a slow bar ($\Omega_b \sim 40 \text{ km s}^{-1} \text{ kpc}^{-1}$). This scenario is also supported by analytic calculations of



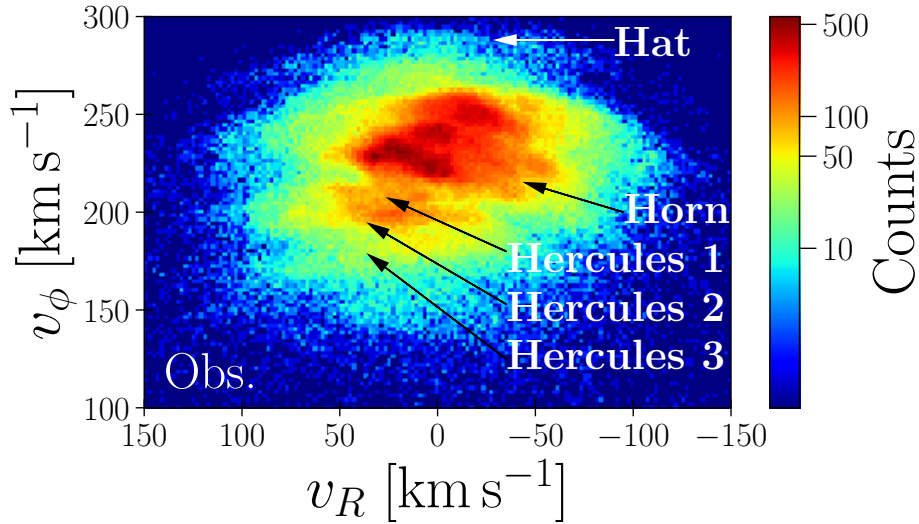


Figure 3.1: Radial and angular velocity-space distribution of stars within 0.2 kpc from the Sun, binned by $2 \text{ km s}^{-1} \times 2 \text{ km s}^{-1}$. This figure is the same as Fig. 1.13, but the data are from *Gaia* DR2 with a 10% relative error cut in the parallax.

perturbed DF in resonance regions (Monari et al. 2019a,b; Binney 2020), and full N -body simulations of a MW-like galaxy (D’Onghia & L. Aguerri 2020).

Other new scenarios attribute the Hercules stream to higher-order resonances of the slow, long bar. Hunt & Bovy (2018) integrated orbits of test particles in analytic bar potentials including an $m = 4$ Fourier mode and suggested that the 4:1 OLR of a slowly rotating bar can lead to a bimodal structure in the Hercules stream. Monari et al. (2019a) also studied the relation between the bar’s higher-order resonances and the solar neighbourhood kinematics using a resonant DF model (Monari et al. 2017c) in the same realistic bar potential as that used in Pérez-Villegas et al. (2017). They showed that CR and 6:1 OLR of the bar create a Hercules-like stream and a horn-like structure, respectively. Similarly, Michtchenko et al. (2018a) performed test particle simulations in a slow-bar potential with higher-order multipole moments combined with a spiral potential, and suggested that the Hercules stream associated with the spiral’s 8:1 ILR (see also Barros et al. 2020). On the other hand, Hattori et al. (2019) also showed that Hercules-like streams originate from orbit families associated with the 5:1 ILR in the simple $m = 2$ slow-bar + spiral potentials.

Note that most of the above studies are based on test particle simulations in ‘static’ (or analytic) potentials. We can easily capture resonant orbits of stars in static potentials; however, previously performed self-consistent N -body simulations of (barred) spiral galaxies have suggested that the structures in the spiral arms and bar change with time in complicated ways (e.g. Sellwood & Carlberg 1984; Sellwood & Sparke 1988; Baba et al. 2009, 2013; Grand et al. 2012a,b; Fujii et al. 2011; D’Onghia et al. 2013; Khoperskov et al. 2019). Such transient nature may affect stellar orbits in higher-order resonances. Higher order resonances are usually weaker than CR or 2:1 OLR. In order to detect higher order resonances such as 4:1 and 6:1 OLR in self-consistent N -body simulations, a high enough resolution is required. Recently, D’Onghia & L. Aguerri (2020) captured stars in the CR resonance using fully self-consistent N -body simulations, but they did not report higher order resonances as the origins of the Hercules stream. Hence, so far no high-order resonances have been reported in self-consistent N -body simulations.

Phase space structures have been found in these self-consistent N -body models, but their origin is unknown. Fujii et al. (2019) performed N -body simulations of disc galaxy models and found a MW-like model, of which some observed structures and kinematics match those of the MW. They performed simulations using a maximum of eight billion particles (more than two hundred million particles for the disc) with the dark-matter halo modelled with N -body particles (live halo). This is an order of magnitude higher mass-resolution than previous similar studies (e.g. D’Onghia & L. Aguerri 2020). Fujii et al. (2019) showed U - V maps obtained in their simulations and discussed if Hercules-like streams are found in

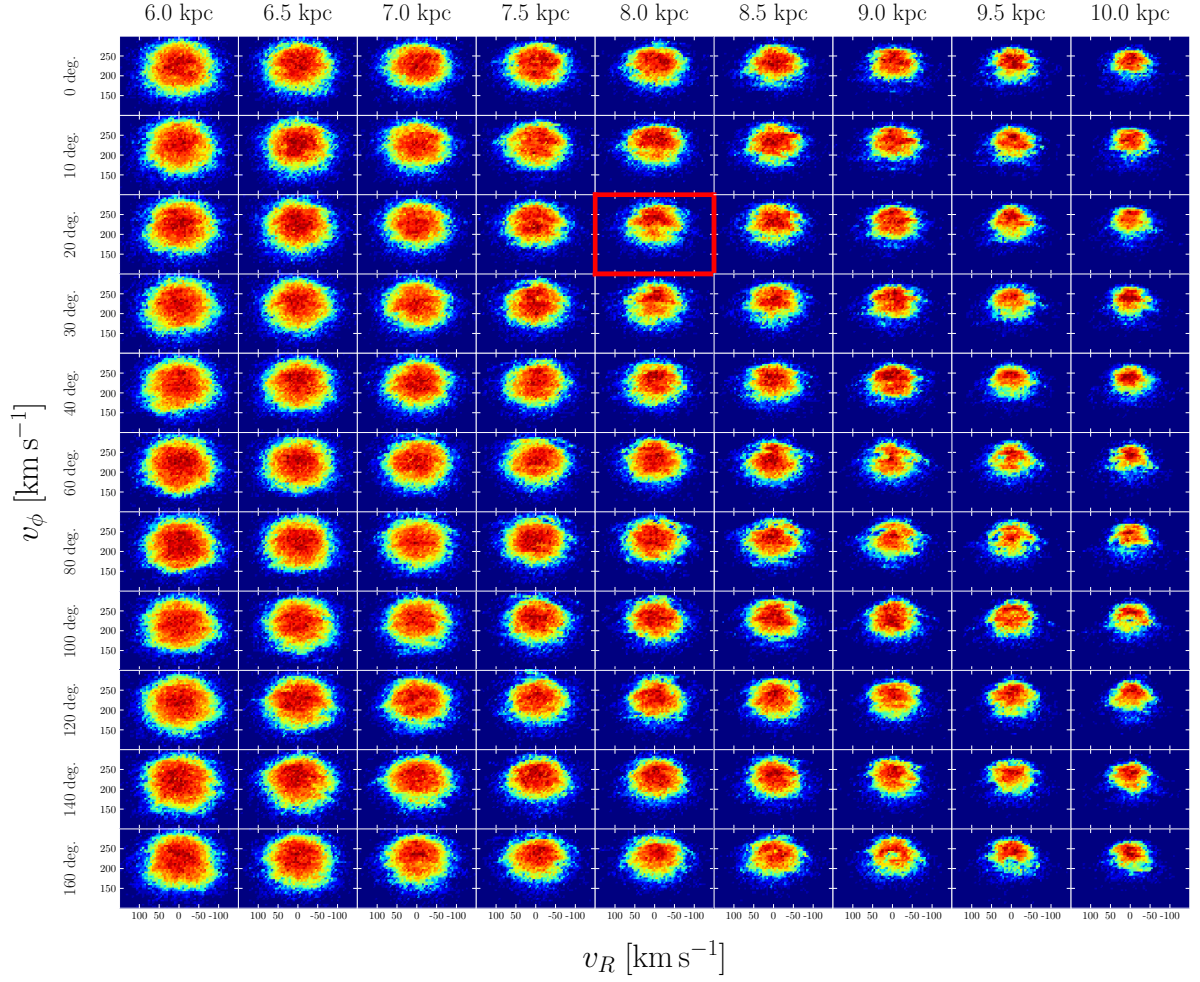


Figure 3.2: 2D-histogram in v_R versus v_ϕ space at various positions in the disc at 10 Gyr. The distribution is for particles within 0.2 kpc from each position. In all panels, the bin size is set to $5 \text{ km s}^{-1} \times 5 \text{ km s}^{-1}$. The panel for $(R, \phi) = (8 \text{ kpc}, 20^\circ)$, corresponding to the solar neighbourhood, is framed by a red rectangle.

N-body simulations. Indeed, they found some Hercules stream-like structures in their simulations, but the origin of the structures has not been investigated.

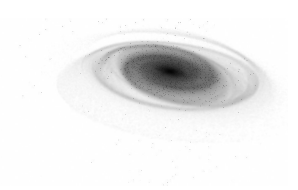
In this chapter, we analyse the results of the *N*-body simulations performed in [Fujii et al. \(2019\)](#), which represents an isolated *MW*-like galaxy modelled completely as an *N*-body system. In this simulation, we track and classify the stellar orbits. The purpose of the classification is to identify stars trapped in resonance. We then show that stars trapped in higher-order resonances actually exist in the live disc potential and that the trimodal structure of the Hercules stream can be explained by such higher-order resonances.

3.2 *N*-BODY MODEL

In this chapter, to study the relation between the velocity-space structures and bar resonances, we use the isolated *MW*-like galaxy modelled described in Section. 2.1.

3.2.1 Distribution of simulated stars in velocity space

To study the origin of the Hercules stream, we begin by locating a Sun-like position in the simulated galactic disc. We take the last snapshot of the simulations ($t = 10 \text{ Gyr}$) and plot the velocity-space distribution of particles within 0.2 kpc from the “Sun” and iterate over positions in the disc. The results



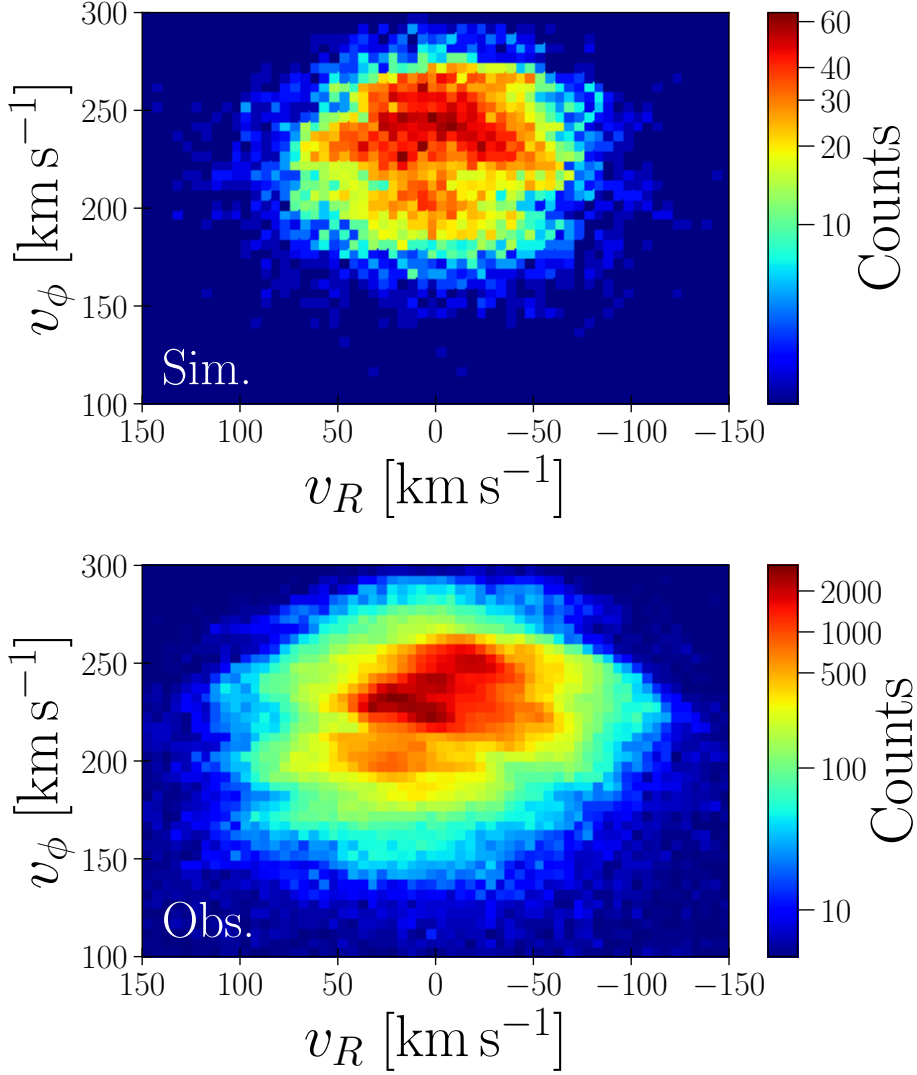


Figure 3.3: *Top*: Distribution of simulation particles in velocity space around $(R, \phi) = (8 \text{ kpc}, 20^\circ)$. This is an enlargement of the panel framed by a red rectangle in Fig. 3.2. *Bottom*: The same figure from Gaia DR2. This is identical with Fig. 3.1, but the bin size is different. The total number of the stars in the maps of the simulation and the observation are 13,303 and 345,152, respectively.

are shown in Fig. 3.2. Note that we assume the position of the “Sun” in the galactic mid-plane ($z = 0$) in the MW model.

At certain locations, we find a velocity-space structure similar to the one observed in Gaia DR2 (Gaia Collaboration et al. 2018b and Fig. 3.1). These observational studies suggest that the Sun has a distance of $R_0 \sim .2 \text{ kpc}$ (Bland-Hawthorn & Gerhard 2016) from the Galactic centre and lies at an angle of $\phi_\odot = 27^\circ \pm 2^\circ$ (Wegg & Gerhard 2013), $29^\circ \pm 2^\circ$ (Cao et al. 2013), $24^\circ\text{--}27^\circ$ (Rattenbury et al. 2007) and $20^\circ\text{--}25^\circ$ (Bissantz & Gerhard 2002) with respect to the major axis of the Galactic bar. By analysing our simulations, we select a distance and position relative to the bar of $(R, \phi) = (8 \text{ kpc}, 20^\circ)$. This choice is based on the similarity of the structure observed in Fig. 3.1 and compared with the kaleidoscope of similar phase-space images in Fig. 3.2. The velocity-space map at $(R, \phi) = (8 \text{ kpc}, 30^\circ)$ also shows the Hercules-like stream, but it is most clearly identified in the map at $(R, \phi) = (8 \text{ kpc}, 20^\circ)$. The space-coordinates framed in red in Fig. 3.2 has the closest correspondence with the observed image. We then select this particular phase-space position as the one to represent the Sun in our simulations.

Fig. 3.3 is the enlarged figure of the velocity-space distribution at $(R, \phi) = (8 \text{ kpc}, 20^\circ)$ (same as the panel framed by a red rectangle in Fig. 3.2). A Hercules-like stream is located from $(v_R, v_\phi) \sim (80, 200) \text{ km s}^{-1}$ to $(-60, 190) \text{ km s}^{-1}$ in this figure. In addition, a Hat-like stream and a Horn-like structure are also seen from

$(v_R, v_\phi) \sim (50, 260)$ to $(-50, 270)$ km s^{-1} and around $(v_R, v_\phi) = (-50, 220)$ km s^{-1} , respectively. Some other moving groups known from observations, such as the Hyades and Pleiades, cannot be clearly mapped to structures in the simulated MW model.

3.2.2 Orbit analysis and identification of resonantly trapped stars

The key advantage of working with an N -body simulation is that resonances can be tested in live systems. The spiral structures and bars evolve with time in a live potential, which is not the case in static potential simulations. In such a time-dependent potential, stars in a resonance may not be able to stay stable in the resonance. In order to capture resonances in a live potential, the orbits of individual stars have to be followed in the live simulations.

To this aim, we thus use the snapshots of our N -body simulation, and trace the orbits of the stars that we are interested in. We especially determine the orbital frequencies of the disc particles in order to classify the particles by their orbital characteristics such as resonances. For this purpose, we perform a frequency analysis of stellar orbits obtained from the N -body simulation with a following frequency measurement method used in Ceverino & Klypin (2007). Here, we detail upon the classification scheme used to identify stellar properties in our simulation.

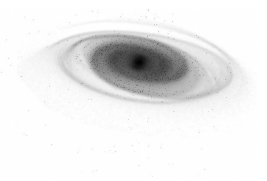
First, we determine the radial frequency, Ω_R . We distinguish Ω_R from the epicycle frequency, κ (Equation 3.1) because here we do not necessarily assume nearly circular orbits. Ω_R is determined from the time series orbit data in the simulation snapshots using the discrete Fourier transform (DFT) for $R(i)$, where $R(i)$ ($i = 1, \dots, 64$) is a radial coordinate in the i -th snapshot. We employ a zero-padding technique for Fourier transforming: 960 zero points are added at the end of the data series. We then sample frequency space with 512 points between $0 \text{ km s}^{-1} \text{ kpc}^{-1}$ and $315 \text{ km s}^{-1} \text{ kpc}^{-1}$, whereby the upper bound is given by the Nyquist frequency. We identify a resonant Ω_R as a frequency that causes a local maximum in the Fourier spectrum. For more details on the DFT analysis, see Binney & Spergel (1982) and Ceverino & Klypin (2007). In contrast, the associated angular frequency Ω_ϕ is determined by a regression analysis instead of a Discrete Fourier Transform. From the snapshots, we collect per particle the series of measured angles $\phi(i)$ as a function of time $t(i)$, where i iterates over the 64 snapshots available. For each particle, this results in pairs $[t(i), \phi(i)]$ ($i = 1, \dots, 64$) to which we fit the function $\phi = \Omega_\phi t + \phi_0$ using a least squares method. The resulting Least-Squares Estimator yields the angular frequency Ω_ϕ of the studied star.

Using the Fourier decomposition of the surface density as described in Chapter 2.1, we obtain the angle of the bar of the last 64 snapshots, which corresponds to $t = 9.38\text{--}10$ Gyr. The bar's pattern speed, Ω_b , is determined using the least squares fitting to $\phi_2(t) = \Omega_b t + \phi_{2,0}$. The obtained pattern speed of the bar in the simulation is $\Omega_b = 46.12 \text{ km s}^{-1} \text{ kpc}^{-1} = 1.53\Omega_{8\text{kpc}}$ where $\Omega_{8\text{kpc}}$ is the circular frequency at $R = 8 \text{ kpc}$ in our MW model. Recent studies such as Sanders et al. (2019) and Bovy et al. (2019) suggested a pattern speed of the Galactic bar of $\Omega_b = 41 \text{ km s}^{-1} \text{ kpc}^{-1} \sim 1.4\Omega_0$, where Ω_0 is the circular velocity at the solar distance. The bar's pattern speed in our simulation is slightly higher than this value, but slower than that favoured by Dehnen (2000)'s 2:1 OLR model for the Hercules stream ($\Omega_b \sim 50 \text{ km s}^{-1} \text{ kpc}^{-1} \sim 1.8\Omega_0$).

In Fig. 3.4, we show the distribution of the frequency ratio $(\Omega_\phi - \Omega_b)/\Omega_R$ for the particles within 0.2 kpc from our "Sun's" location at $(R, \phi) = (8 \text{ kpc}, 20^\circ)$. Here, we use the bar's pattern speed (Ω_b) obtained from our simulations. The clearly visible statistically significant peaks in the distribution correspond to stars in resonances with the bar, whereas small fluctuations simply arise from binning. In Fig. 3.4, we indicate the positions of multiple OLRs as vertical solid lines. In the region that we assumed as the solar neighbourhood, we find at the four OLR of 2:1, 3:1, 4:1 and 5:1.

We assume that particles within a rage of ± 0.01 from the exact resonance frequency ratio are in resonance; these are the two adjacent bins to the exact resonance frequency. We select these as resonant particles in the following analyses. As an example, for particles trapped in the 2:1 resonance, we select those whose frequency ratios are in the range of $-0.51 < (\Omega_\phi - \Omega_b)/\Omega_R < -0.49$ which corresponds to the bins between the two vertical dashed lines next to the line of $(\Omega_\phi - \Omega_b)/\Omega_R = -0.5$.

In order to confirm the validity of this selection procedure, we verify whether the selected particles are in resonant orbits. To verify the results of the Fourier analysis we randomly select 100 particles from the various resonant areas and plot their orbits over time. By visually inspecting them, as the sub-sample of 5 cases for each of the orbital resonances, presented in Fig. 3.5, we confirm that except a few odd cases, all stars are on the appropriate resonance orbit. We show the panels that demonstrate this procedure for 100



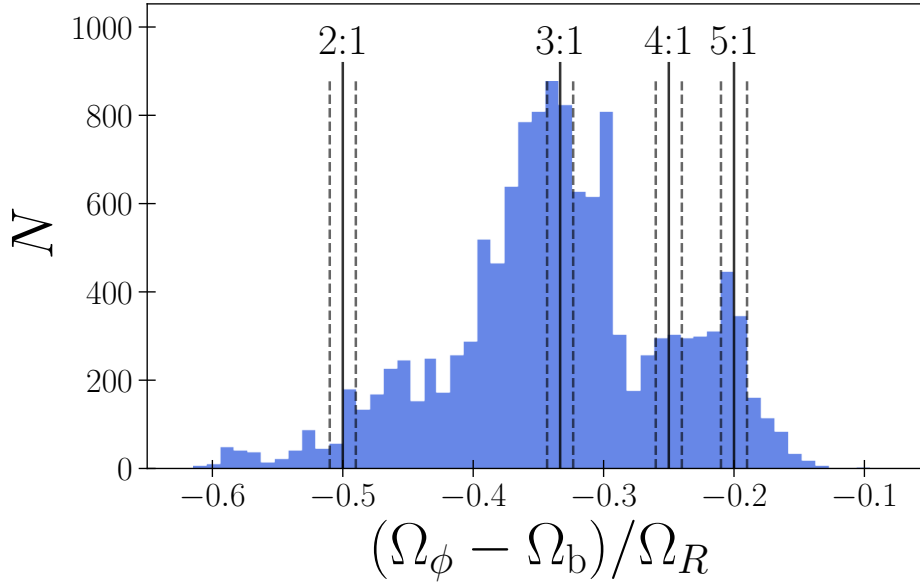


Figure 3.4: Orbital frequency ratios for the particles within 0.2 kpc from $(R, \phi) = (8 \text{ kpc}, 20^\circ)$. The four vertical solid lines indicate $(\Omega_\phi - \Omega_b)/\Omega_R = -1/2, -1/3, -1/4$ and $-1/5$, corresponding to the 2:1, 3:1, 4:1 and 5:1 resonances, respectively. Pairs of dashed lines beside solid lines indicate frequency ratios of $-1/2 \pm 0.01$, $-1/3 \pm 0.01$, $-1/4 \pm 0.01$, and $-1/5 \pm 0.01$, respectively. For each resonance, particles whose frequency ratios are between a dashed line pair are selected as resonantly trapped particles.

different plotted orbits in Appendix B. All the orbits in Fig. 3.5 are shown in the rotating frame of the bar, which is represented by the grey ellipse in each panel. In this figure, the galaxy rotates clockwise. In this frame, the particles accordingly rotate counter-clockwise as their angular frequencies are slower than the bar’s pattern speed. Stars trapped in the $m:1$ resonances oscillate m times in the radial direction while they circle the bar. Thus, we confirm that our method properly identifies stars in resonant orbits.

Note that naively, one would expect that orbits of the 2:1 resonance to align with the bar or to be perpendicular to it in the case of OLR. In our simulation, however, we find that the orbits in the 2:1 OLR are inclined with respect to the orientation of the bar as shown in the top five panels in Fig. 3.5. In other regions, however, particles which are exactly aligned with or perpendicular to the bar are dominant. In the region which we assumed as the solar neighbourhood, particles in inclined orbits are dominant. The reason is currently not clear, but this may be because the position we “observed” is not exactly on the 2:1 OLR radius. Other possible reasons are spiral arms and/or the bar’s slow-down.

Orbital radii decrease from lower to higher order resonances (from the top to the bottom in Fig. 3.5). This is more apparent in Fig. 3.6, in which we show four resonantly trapped orbits in a single frame. This is simply because higher-order resonances have smaller guiding radii.

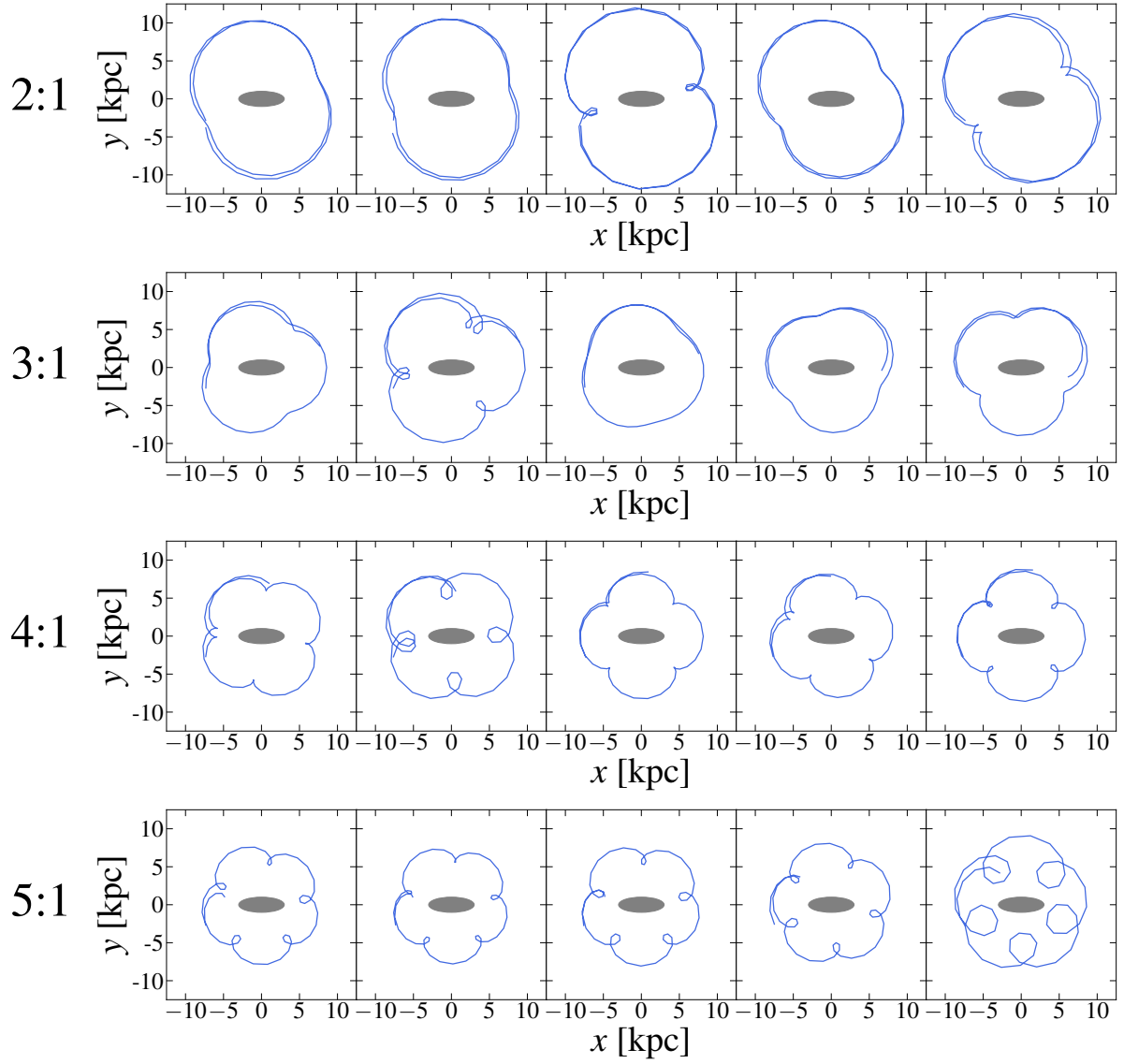
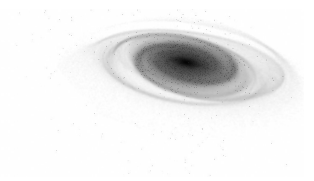


Figure 3.5: Examples of the orbits trapped in the bar resonances. The grey ellipse in the figure represents the bar orientation. The orbits are shown in the bar's rotating frame. The galaxy rotates clockwise, hence particles rotate counter-clockwise in this frame.



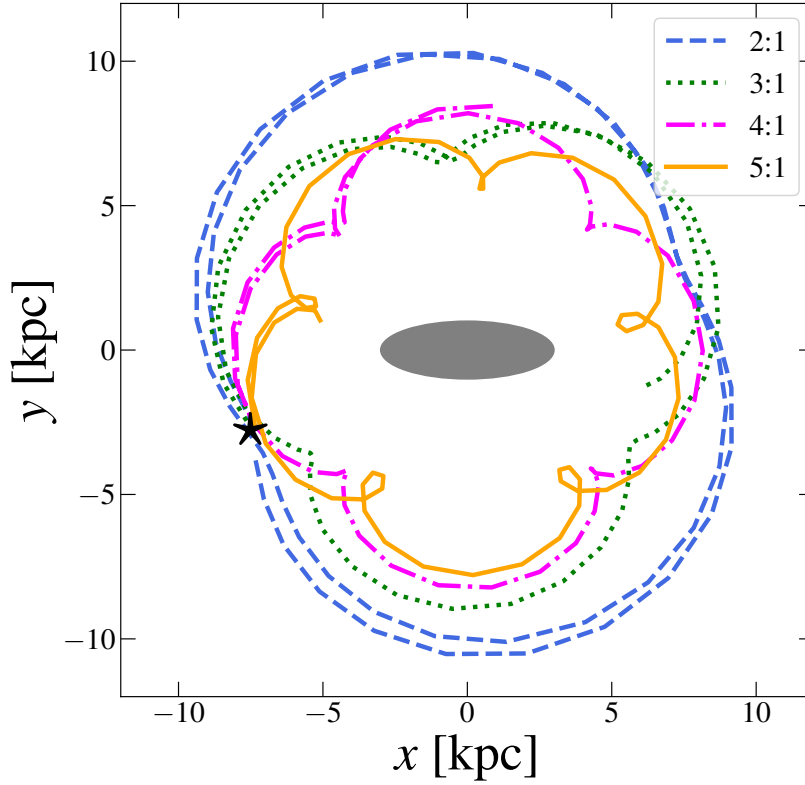


Figure 3.6: Resonantly trapped orbits in a single frame. The blue dashed, green dotted, magenta dash-dotted and orange solid lines represent the 2:1, 3:1, 4:1 and 5:1 resonance orbits, respectively. In this figure, the galaxy rotates clockwise. The star symbol presents the position of the Sun in our model, $(R, \phi) = (8 \text{ kpc}, 20^\circ)$.

3.3 RESULTS FOR GAIA

Using the orbit analysis of our simulation detailed upon in Sect. 3.2.2, we succeeded in identifying the simulation’s bar pattern speed, and the resonance type of stars trapped in resonant orbits. By now comparing to the Gaia data, we can thus use our simulation analysis to constrain the properties of the MW. The thus found implications for the origin of the Hercules stream are presented in Sect. 3.3.1, and constraints on the MW’s bar pattern speed are presented in 3.3.2.

3.3.1 The origin of the Hercules stream from resonances

The Hercules stream creates a prominent overdensity of stars in the v_R versus v_ϕ projection of the Gaia data (see Fig. 3.1). The recognition of this overdensity’s trimodality (e.g. Ramos et al. 2018) is recent, and requires an explanation. We here present the evidence that stars trapped in resonant orbits will form such a trimodal stream structure.

This can be seen from the top panel of Fig. 3.7, where we over plot the position of particles in resonance in the velocity map (Fig. 3.3). In the bottom panel of the figure, we show the velocity map coloured by the fraction of particles in resonance in each bin. We find that between 60% and 100% of all stars in the Hercules-like stream of our simulation are trapped in the 4:1 and 5:1 OLR. This implies that the stars within the Hercules stream (two streams at $v_\phi = 220$ and 200 km s^{-1}) will also be dominated by resonantly trapped stars. Although the two resonantly trapped families are blurred in our velocity map of Fig. 3.3, these two streams light up and are clearly separated when classified by resonance type in Fig. 3.7, thereby providing a natural explanation for multiple streams of Gaia’s observations of the Hercules stream.

In our simulations, stars trapped in the 2:1 OLR have velocities much higher than the rotation speed at the position of the Sun. This is because the guiding centre of the 2:1 OLR in our model is outer than 8 kpc. These stars appear to populate the area in phase space that was characterized by the ‘hat’ structure in

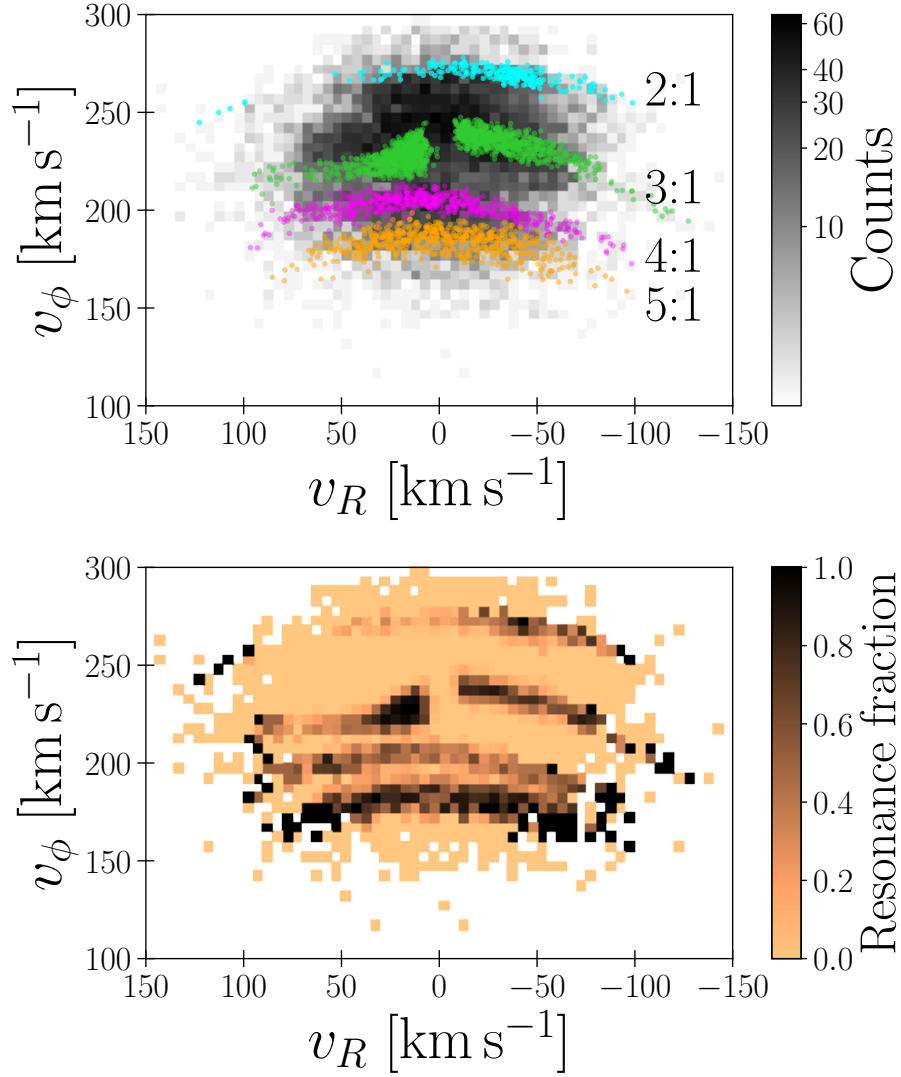


Figure 3.7: *Top*: Resonantly trapped particles in velocity space. The velocities of resonantly trapped particles are overplotted in the v_R versus v_ϕ plane in Fig. 3.3. Cyan, green, magenta and orange dots represent particles trapped in the 2:1, 3:1, 4:1 and 5:1 resonances, respectively. *Bottom*: Colours indicate the fraction of the particles trapped in the 2:1, 3:1, 4:1 or 5:1 resonances in each bin.

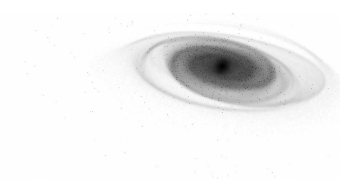
the observation. Stars in the 3:1 [OLR](#) are distributed around the circular velocity at 8 kpc. Among the 3:1 [OLR](#) stars, those with $v_R < 0$ are part of the ‘horn’ structure.

The guiding-centre radius (R_g) for each [OLR](#) for our simulated model can be determined as we know the structure of the simulated galactic disc. The radial frequency under the epicycle approximation is given by (Binney & Tremaine 2008)¹:

$$\kappa^2(R_g) = \left(R \frac{d\Omega^2}{dR} + 4\Omega^2 \right)_{R_g}. \quad (3.1)$$

Here, we calculate κ and Ω at each radius from the particle data of the N -body simulation. We also determine the circular frequency, Ω , by averaging the radial accelerations of particles in an annulus with a width of 50 pc at each radius. In Fig. 3.8, we show $\Omega + \kappa/m$ ($m = 2, 3, 4$ and 5) and Ω as functions of R . The horizontal line in Fig. 3.8 indicates the pattern speed of the bar. The radii at which the line intersects with the frequency curves correspond to the guiding-centre radii for the 2:1, 3:1, 4:1, 5:1 and the corotation resonances. In our model of the [MW](#), the Sun, at a distance of ~ 8 kpc from the Galactic

¹ Under the epicycle approximation, κ and Ω are identical with Ω_R and Ω_ϕ , respectively, but we use the different symbols to distinguish them because we do not necessarily assume nearly circular orbits in the simulation.



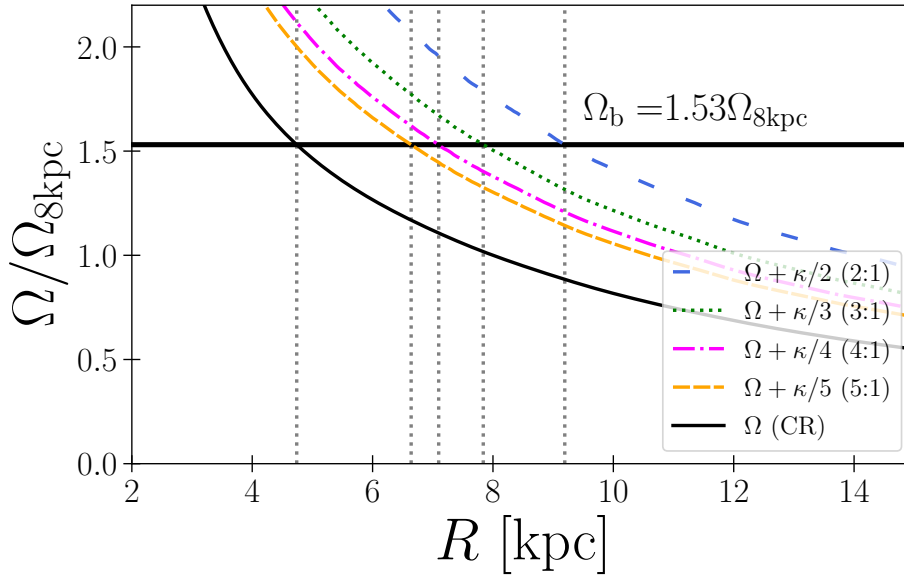


Figure 3.8: The orbital frequencies as functions of the galactocentric radius R . Ω was determined from the velocity curve and $\Omega + \kappa/m$ ($m = 2, 3, 4$ and 5) as expected within the epicycle approximation are plotted. The vertical axis is normalized by $\Omega_{8\text{kpc}}$. The horizontal line indicates the bar's pattern speed, and the vertical lines represent the guiding radii for the resonant orbits.

centre, is close to the 3:1 [OLR](#). It is then not surprising that this resonance is dominant in the local stellar population.

3.3.2 The Milky Way's bar pattern speed

When projecting the *Gaia* data into the R - v_ϕ plane, a series of ridges appears over a wide range of R ([Kawata et al. 2018](#); [Antoja et al. 2018](#); [Fragkoudi et al. 2019](#); [Ramos et al. 2018](#); [Bernet et al. 2022](#)). Although the origin of these structures is still in debate, previous studies (e.g. [Monari et al. 2017b, 2019a](#); [Fragkoudi et al. 2019](#); [Barros et al. 2020](#)) have discussed that these ridges may originate from resonances, while other studies have suggested perturbations by a satellite galaxy such as the Sagittarius dwarf ([Khanna et al. 2019](#); [Laporte et al. 2019](#)) or by winding transient spiral structure ([Hunt et al. 2018, 2019](#)). In this section, we study the relation between the observed ridges in *Gaia* DR2 and resonances in our simulated MW model: by projecting our simulated and classified stars into the R - v_ϕ plane, we can directly compare to the same projection of the *Gaia* DR2 data. If the stars classified by resonance type align with the observed ridges, then this provides compelling evidence that these ridges are indeed caused by resonantly trapped stars.

In Fig. 3.9, we show the distributions of stars in the R - v_ϕ plane as it arises in our simulated MW model (left column) and in the *Gaia* DR2 (right column). The top panels show 2D-histograms of particles within 2 kpc from the Sun [$(R, \phi) = (8\text{kpc}, 20^\circ)$, in our model]. This panel reveals a selection effect caused by *Gaia*'s measurement uncertainties: due to us having selected stars with relative parallax error below 10% the right-hand panel displays systematically fewer stars in approximately concentric rings around the Sun's position at 8.2 kpc. Visually, this causes the smaller extent of the red area in the right-hand panel. We expected, however, that our analysis is robust with respect to this selection effect: it implies that fewer stars make it into our DR2 projection than into the projection of our simulation, but those stars that are selected are not systematically biased.

The middle panels show the mean v_R values in each of the bins in the top panels. In order to make this figure, we selected stars from the *Gaia* DR2 catalogue whose relative errors in parallaxes are less than 10%, and whose errors in radial velocities are less than 5 km s^{-1} . Their distances from the Galactic mid-plane are less than 0.2 kpc, and their distances from the Sun are less than 2 kpc. The total number of stars in this sample is 2,289,755. We assume that the distance of the Sun from the Galactic centre is $R_0 = 8.2\text{ kpc}$, and that the distance of the Sun from the Galactic mid-plane is about $z_0 = 25\text{ pc}$, whereby the velocity of

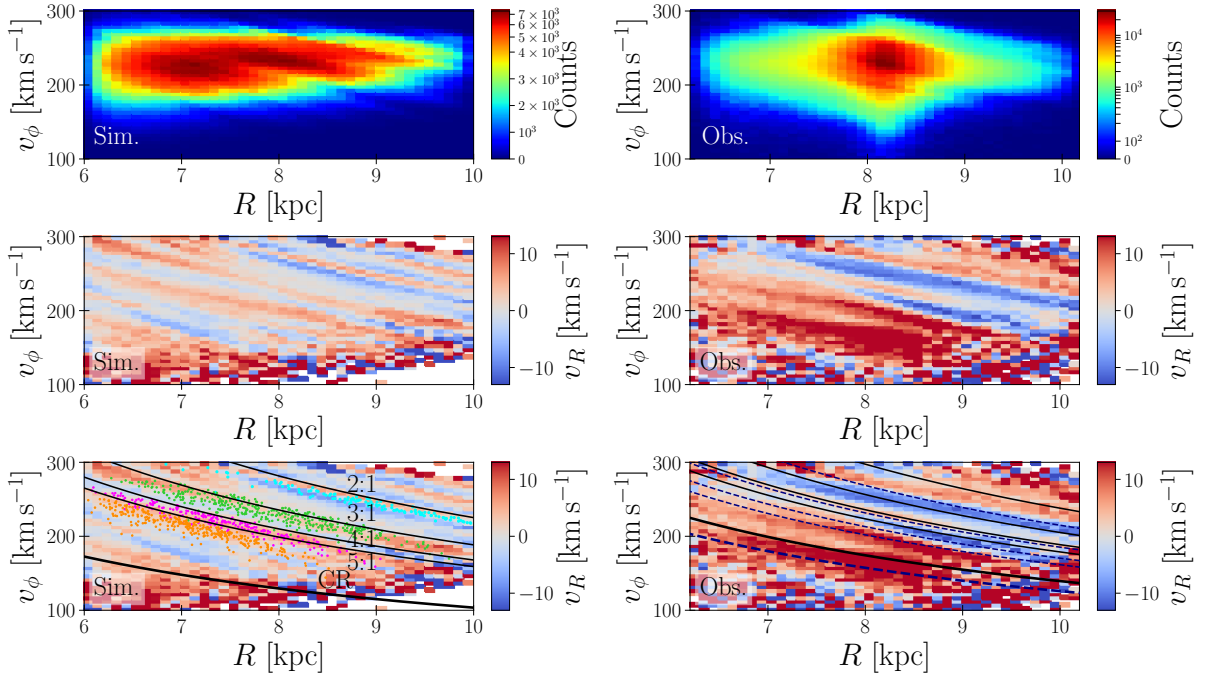


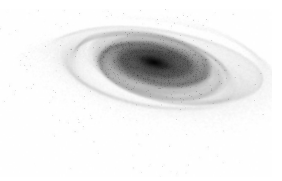
Figure 3.9: *Left*: Phase-space structures in the R versus v_ϕ space from the *MW* simulation. *Right*: Counterparts from *Gaia* DR2. *Top*: Colours indicate the number counts in each bin. *Middle*: Colours indicate the mean v_R in each bin. *Bottom*: Same as middle panels, but with curves of constant angular momentum overplotted. From the top to bottom curves, they correspond to the angular momenta of the circular orbits at a resonant radius of the 2:1, 3:1, 4:1, 5:1 OLR and CR. Solid and dashed curves in the bottom right panel correspond to a bar’s pattern speed of $\Omega_b = 1.4\Omega_0 \sim 40 \text{ km s}^{-1} \text{ kpc}^{-1}$ or $\Omega_b = 1.55\Omega_0 \sim 45 \text{ km s}^{-1} \text{ kpc}^{-1}$, respectively. Dots in the bottom left panel indicate positions of particles trapped in each of the resonances. The colours are the same as those in Fig. 3.7.

the Sun with respect to the LSR is about $(U_\odot, V_\odot) = (10, 11) \text{ km s}^{-1}$, and the circular velocity at $R = R_0$ of $v_0 = 238 \text{ km s}^{-1}$ (Bland-Hawthorn & Gerhard 2016).

In the middle right panel in Fig. 3.9, we can identify several streams, or ridges, in the *Gaia* data. For convenience, we refer to ridges with $v_R > 0$ as ‘red’ and $v_R < 0$ as ‘blue’. From top to bottom, red ridges alternate with blue ridges. Amongst these, two red ridges of $v_R > 0$ located at $v_\phi \sim 200 \text{ km s}^{-1}$ and $v_\phi \sim 180 \text{ km s}^{-1}$ at 8 kpc, are associated with the Hercules stream. In the middle panel our simulation is shown on the left-hand side. It shows ridges similar to those observed in the *Gaia* data (middle panel on the right-hand side). In our previous discussion, we argued that the Hercules-like stream in our *MW* model corresponds to a ridge from $(R, v_\phi) \sim (6 \text{ kpc}, 250 \text{ km s}^{-1})$ to $(9 \text{ kpc}, 180 \text{ km s}^{-1})$. This ridge, eventually branches into two separate structures at around 8 kpc.

In order to study the relation between the resonances and ridges in our simulation, we overplot the positions of particles in the resonances in the bottom left panel of Fig. 3.9. We here randomly sample 5000 particles within 2 kpc from $(R, \phi) = (8 \text{ kpc}, 20^\circ)$ and extract resonant particles from them as we do in Sec. 3. In addition, we plot curves of constant angular momentum ($L_z = Rv_\phi$) in the figure. These correspond to the angular momenta of the circular orbits at the resonance radii determined in Fig. 3.8. As discussed in studies such as Ramos et al. (2018) and Quillen et al. (2018), resonant orbits approximately follow constant L_z curves if their radial oscillations are small.

The overplotting reveals that both the resonant particles and the constant L_z curves follow the ridges. While Monari et al. (2019a) showed that the constant L_z curves are blue ridges ($v_R < 0$) for 2:1, 3:1 and 4:1 resonances according to their Figure 6, our L_z curves fall just between red ($v_R > 0$) and blue ridges. In addition, we find that the resonant particles are always distributed below the constant L_z curves in R - v_ϕ map. This arises due to their radial oscillations not being negligible. Orbits in a resonance follow a line in L_z vs. J_R space where J_R is a radial action (see Fig. 4 in Binney 2018). As the resonant lines have negative slopes, if resonant orbits J_R values are large, their L_z values are smaller than those of the circular orbits ($J_R = 0$).



Turning to the *Gaia* data, the ridges seem to trace the constant angular momentum lines also in our MW's data. The solid curves in the bottom right panel of Fig. 3.9 represent the angular momenta of the resonances for the bar's pattern speed of $\Omega_b = 1.4\Omega_0$, which is suggested by Sanders et al. (2019) and Bovy et al. (2019). We also present the same ones but for $\Omega_b = 1.55\Omega_0$, which is the pattern speed in our simulation. In order to determine the radii of the resonances and corresponding angular momenta, we assume a flat rotation curve of $v_c = 238 \text{ km s}^{-1}$.

Considering that the top red ridge corresponds to the 2:1 OLR, the curve at $\Omega_b = 1.4\Omega_0$ is close to the relation between the ridge and the constant L_z curve as shown in our simulation (the curve is located just above the red ridge). However, with $\Omega_b = 1.4\Omega_0 = 40 \text{ km s}^{-1} \text{ kpc}^{-1}$, there are no OLR around the Hercules stream, but the corotation resonance is located at the lowest value of v_ϕ of the Hercules stream. Accordingly, if we assume a higher pattern speed, i.e. $\Omega_b = 1.55\Omega_0 = 45 \text{ km s}^{-1} \text{ kpc}^{-1}$, the 2:1 resonance is located slightly below the top red ridge, but the relation between the resonances and ridges for the 4:1 and 5:1 resonances looks similar to that seen in our simulations. In both pattern speeds, the pronounced red ridge near the bottom which we identify with the third Hercules stream, correspond to the corotation resonance. We find the same phenomena in our simulation, but without the stars in corotation resonance. The latter is a consequence of the relatively low-resolution of our simulations and the fact that in the *Gaia* data the corotation resonance is closer to the Sun than in our simulations. This is a consequence of our models not perfectly matching to the real MW. Thus, our comparison between the *Gaia* data and our simulation suggest that the pattern speed of the MW's bar is relatively slow, with $\Omega_b = 1.4\text{--}1.55\Omega_0$ which corresponds to $40\text{--}45 \text{ km s}^{-1} \text{ kpc}^{-1}$.

3.4 SUMMARY

We have analysed a finely resolved N -body simulation of a MW-like galaxy obtained in Fujii et al. (2019) in order to investigate the origins of the phase-space structures in the MW galaxy as observed by *Gaia*. We investigated the distribution of particles in the v_R - v_ϕ plane by iterating over multiple positions in the disc. This revealed a Hercules-like stream around $(R, \phi) = (8 \text{ kpc}, 20^\circ)$ in our simulation, as is also known from the actual solar neighbourhood. From a spectral analysis of stellar orbits, we found mainly four resonances of the bar, namely the 2:1, 3:1, 4:1 and 5:1 resonances around there. The observed structures in the v_R - v_ϕ plane, can be explained by stars being trapped in the 4:1 and 5:1 outer Lindblad resonances. In our simulations, these resonances give rise to structures similar to those observed in the actual Hercules stream. Our results therefore favour that the Hercules stream is composed out of stars trapped in the 4:1 and 5:1 OLR and CR, which would also explain its trimodal structure as revealed by *Gaia* DR2. In addition, the stars in the 2:1 and 3:1 OLR match to the 'hat' and 'horn' structures, respectively.

We further compared the distribution of stars in the R - v_ϕ plane in our simulation with that obtained from the *Gaia* data. Particles identified to be in resonance in our simulation follow ridges in the R - v_ϕ plane. Similar ridges have also been found in the *Gaia* data and matching the observed ridges to resonances, our results suggest a relatively low pattern speed of the MW's bar, namely $\Omega_b = 1.4\text{--}1.55\Omega_0$, which corresponds to $40\text{--}45 \text{ km s}^{-1} \text{ kpc}^{-1}$. This is consistent with recent studies (e.g. Sanders et al. 2019; Bovy et al. 2019).

In contrast to test particle models using static potentials, N -body models have some difficulties when comparing the results with observational data due to the time-dependence of the bar and spiral arms. Fujii et al. (2019) showed that v_R - v_ϕ maps obtained from N -body simulations change with time. This is a natural consequences of dynamic spiral arms (e.g. Sellwood & Carlberg 1984; Baba et al. 2013). In fact, Hunt et al. (2018, 2019) discussed phase mixing by dynamic transient spiral arms, which in combination with bar resonances, creates a velocity-space distribution similar to what is seen in observations (see also De Simone et al. 2004). Furthermore, the evolution of the bar can also affect the stellar velocity-space distribution. Recently, Chiba et al. (2021) showed that stars trapped in the resonances of the bar are dragged in the phase space when the bar slows down using secular perturbation theory and test particle simulations (see also Weinberg 1994; Halle et al. 2018). This can also cause the formation of a Hercules-like structure. We will discuss the time dependence of the velocity distribution, caused by the dynamical evolution of spiral arms and bar in fully self-consistent N -body simulations, in the next chapter.

TIME EVOLUTION AND SPATIAL VARIATION OF THE VELOCITY-SPACE SUBSTRUCTURES

4.1 INTRODUCTION

In the previous chapter, we analysed a high-resolution N -body simulation of the MW-like isolated galaxy and found a Hercules-like stream in the final snapshot. Orbital frequency analysis confirmed that it is made from 4:1 OLR and 5:1 OLR. We concluded that the trimodal structure of the Hercules stream in the MW can be explained by 4:1 OLR, 5:1 OLR and CR in the bar's pattern speed of $\Omega_b \approx 40\text{--}45 \text{ km s}^{-1} \text{ kpc}^{-1}$. This study confirmed that Hercules-like streams originating from the bar resonance exist in at least one position in one snapshot. In this chapter, we analyse the same simulation data but put the focus on the time evolution and spatial variation of the local velocity-space distributions. We use Kullback-Leibler divergence (KLD) to measure the similarity of the velocity-space distributions in the simulation and that of the solar neighbourhood stars. In Section 4.2, we describe the analysis. In Section 4.3, we show how velocity-space distributions and the KLDs vary as functions of time and spatial positions. In Section 4.4, we perform the orbit analysis for the particles around the position where the velocity-space distributions with high similarities are detected. This analysis shows that velocity-space substructures such as Hercules stream are made from bar resonances. The summary of this chapter is given in Section 4.5.

4.2 DATA AND ANALYSIS

4.2.1 N -body model

We use the isolated MW-like N -body described in Section 2.1. In Chapter 3, we mainly analysed the local phase-space structure in the final snapshot of the simulation, whereas in this chapter, we analyse the time evolution of the velocity-space distributions. Fig. 4.1 shows the face-on views of the MW model at $t = 8.97, 9.29$ and 10 Gyr. As this figure shows, we do not see significant structural evolution of the disc in the later stage of the simulation. However, the detailed dynamical properties fluctuate with time. Fig. 4.2 shows the bar's pattern speed and amplitude as functions of time. The bar's pattern speed and amplitude exhibit oscillations even after the bar formation completes. These oscillations can potentially affect the velocity-space distributions in the solar neighbourhood.

4.2.2 Analysis of the Gaia data

From the Gaia EDR3 catalogue, we select samples whose distance from the Sun is less than 200 pc ($1/\omega[\text{mas}] < 0.2$). More details of the selection and analysis of the Gaia data are described in Section 2.3.

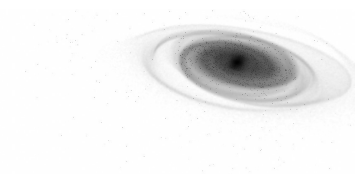
4.2.3 Kullback-Leibler divergence

We use Kullback-Leibler divergence (KLD; Kullback & Leibler 1951) to quantitatively evaluate the similarity of the velocity-space distributions in the simulation and that in the observation. KLD is defined between two probability distributions. When $p(x)$ and $q(x)$ are discrete distributions in a probability space \mathcal{X} , the KLD between them is defined as

$$D(p||q) \equiv \sum_{x \in \mathcal{X}} p(x) \log \frac{p(x)}{q(x)}. \quad (4.1)$$

KLD satisfies the following properties like a 'distance' between p and q .

1. $D(p||q) \geq 0$.
2. $D(p||q) = 0$ if and only if $p = q$.



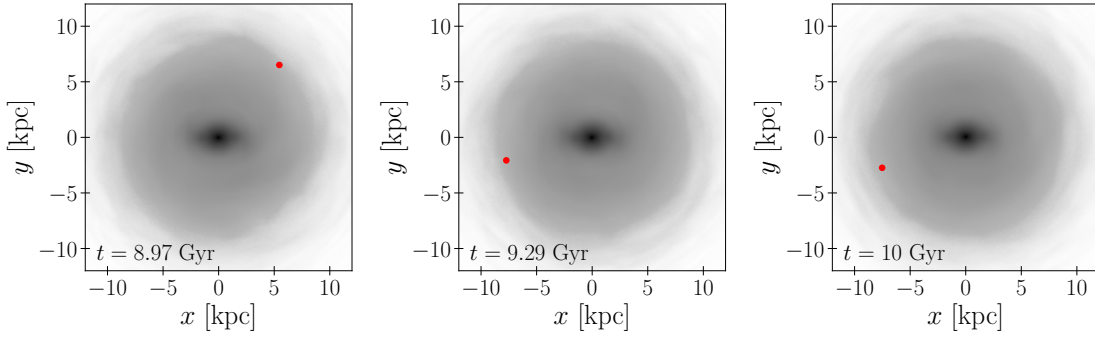


Figure 4.1: Face-on views of the MW model at $t = 8.97, 9.29$ and 10 Gyr. The red dots indicate the position where we detect the velocity-space distribution similar to that in the solar neighbourhood in the previous chapter ($t = 10$ Gyr) and this chapter ($t = 8.97$ and 9.29 Gyr).

We note that $D(p||q)$ is not equal to $D(q||p)$, hence it is not a distance in a mathematical sense. To be more precise, $D(p||q)$ represents how a distribution q differs from a reference distribution p . In this study we would like to evaluate how well the velocity-space distributions in the simulation reproduce that of the MW, hence p and q are determined from the observation and the simulation, respectively. The distribution p is determined from the *Gaia* EDR3 data (Gaia Collaboration et al. 2021). We first divide the velocity space in a grid shape to convert the observation and simulation data to probability distributions. There are some uncertainties in the rotation curves of the MW and the Sun’s velocity with respect to the LSR (Bland-Hawthorn & Gerhard 2016). To take the uncertainties into account, we use relative velocities, $\hat{v}_R = (v_R - \bar{v}_R)/\bar{v}_\phi$ and $\hat{v}_\phi = (v_\phi - \bar{v}_\phi)/\bar{v}_\phi$, instead of absolute values. Mean velocities $(\bar{v}_R, \bar{v}_\phi)$ are determined for the stars within 200 pc from the Sun. We divide the \hat{v}_R versus \hat{v}_ϕ space in a range of $(-0.5, 0.5) \times (-0.333, 0.333)$ into 48×32 cells. We determine the probability that we find a star in a cell, dividing the star count in the cell by the total number of stars in all the cells. Equation (4.1) indicates that KLD can diverge if a probability is zero in a cell (i.e. it does not contain stars). In order to avoid that, we alternatively use the kernel density estimation via `scipy.stats.gaussian_kde` (Virtanen et al. 2020) as value for the empty cells. The value in a cell at $(\hat{v}_R, \hat{v}_\phi)$ is represented as

$$f(\hat{v}) = \sum_{i=1}^N \prod_{j=\{R, \phi\}} \frac{w_j}{h_j} K\left(\frac{\hat{v}_j - \hat{v}_{ij}}{h_j}\right); \quad K(x) = \frac{1}{\sqrt{2\pi}} \exp\left(-\frac{x^2}{2}\right). \quad (4.2)$$

N is the total number of the stars in the sampling volume. \hat{v}_i is the relative velocity of the i -th star. w_R and w_ϕ are the cell widths with $w_R = w_\phi = 0.0208$. Kernel widths h_R and h_ϕ are determined with the method described in Scott (2015). The typical values of h_R and h_ϕ are 0.03 and 0.02, respectively.

4.3 RESULTS

4.3.1 Time evolution of the KLDs

In this section, we investigate the time evolution of the KLDs and velocity-space distributions in the simulation. We evaluate KLDs between the velocity-space distribution for the stars within 200 pc from the Sun and those for particles within 200 pc from $(R, \phi) = (7 \text{ kpc}, 25^\circ)$, $(8 \text{ kpc}, 25^\circ)$ and $(9 \text{ kpc}, 25^\circ)$ in the simulation, where R and ϕ are the distance from the galactic centre and the angle with respect to the bar’s major axis, respectively. We assume that the ‘Sun’ in the simulation locates on the galactic mid-plane ($z = 0$). Fig. 4.3 shows the KLDs at the three points as a function of time for both the long-term and short-term evolution. On a long time scale they decrease with time, and on a short time scale they oscillate. The long-term evolution indicates that the velocity-space distributions are more similar to that in the observed solar neighbourhood during the later epochs than in the early epochs of the simulation. This is a natural consequence of the setup of the simulation. Fujii et al. (2019) adjusted the initial conditions of the simulation so that the final snapshot fits the observations. The short-term evolution indicates that the similarity of the velocity-space distribution fluctuates rapidly. Even if we find a velocity-space distribution

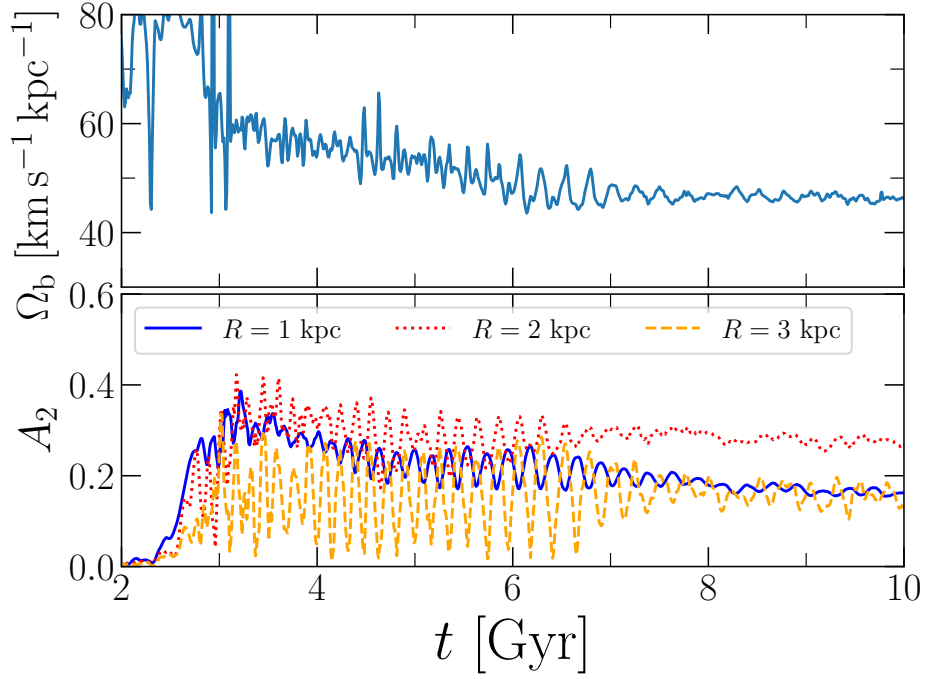


Figure 4.2: Time evolution of the bar’s pattern speed and amplitude.

similar to the observed one at a certain position at a certain time, a velocity-space distribution at the same position at another time is not necessarily similar to the observed one.

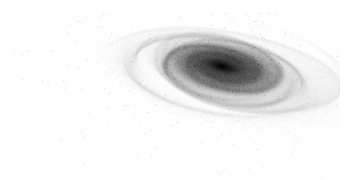
We can identify the correlation between the time evolutions of the [KLDs](#) and the time evolution of the bar by comparing Fig. 4.2 and Fig. 4.3. A clear bar structure appears at $t \simeq 3$ Gyr from the beginning of the simulation. The [KLDs](#) start decreasing at this time. From $t \simeq 3$ Gyr to $t \simeq 7$ Gyr, the bar’s pattern speed slows down. During this phase, the [KLDs](#) also decrease with time. The bar is more stable after $t \simeq 7$ Gyr than before that although the pattern speed shows small fluctuations. In this epoch, the [KLDs](#) at $(R, \phi) = (7 \text{ kpc}, 25^\circ)$ and $(8 \text{ kpc}, 25^\circ)$ do not evolve monotonously but fluctuate around 0.3 and 0.2, respectively. The [KLD](#) at $(9 \text{ kpc}, 25^\circ)$ decreases slowly. The bar’s pattern speed is a key parameter in discussions on bar resonances. It determines the resonance radii when azimuthal and radial frequencies are given as functions of radial coordinate R ([Binney & Tremaine 2008](#)). This correlation between the [KLDs](#) and the bar’s pattern speed implies that the bar resonances play an important role in regulating the local velocity-space distributions. In Section 4.4, we discuss the relation between the velocity-space substructures and bar resonances.

The fluctuations of the [KLDs](#) are also important. Although the [KLD](#) at $(R, \phi) = (8 \text{ kpc}, 25^\circ)$ is smaller than those at the other two positions at $t \gtrsim 7$ Gyr, it fluctuates with time. We do not always observe the velocity-space distributions similar to that in the solar neighbourhood at this position. This emphasizes the non-static nature of the galaxy in the simulation.

4.3.2 Angle with respect to the bar and spirals

4.3.2.1 Angle with respect to the bar

In the previous section we saw that after $t \simeq 7$ Gyr the [KLD](#) at $(R, \phi) = (8 \text{ kpc}, 25^\circ)$ tends to be smaller than at $(R, \phi) = (7 \text{ kpc}, 25^\circ)$ and $(R, \phi) = (9 \text{ kpc}, 25^\circ)$. Here, we investigate where in the disc we often detect velocity-space distributions similar to that in the solar neighbourhood. We evaluate the [KLDs](#) of



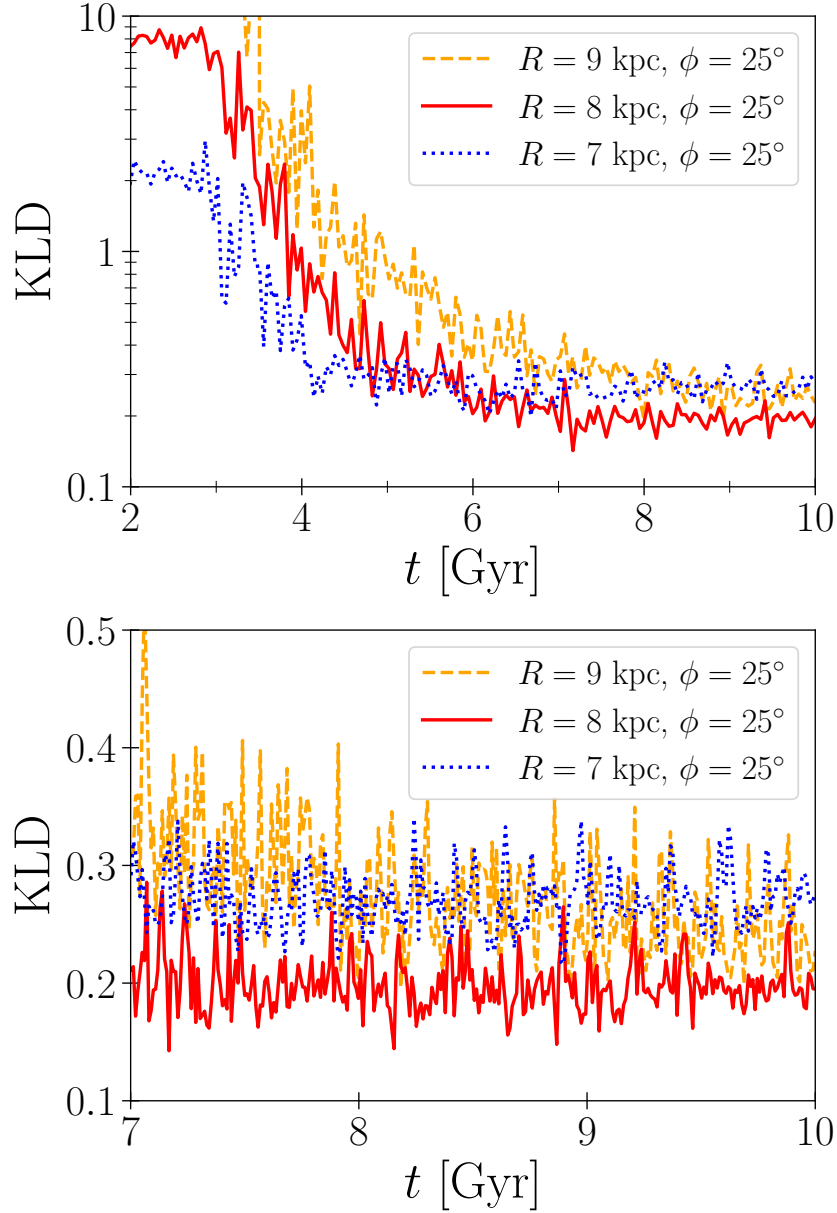


Figure 4.3: *Top*: Time evolution of the KLD s at fixed positions in the simulation. Blue, red and yellow lines show the KLD s at $(R, \phi) = (7 \text{ kpc}, 25^\circ)$, $(8 \text{ kpc}, 25^\circ)$ and $(9 \text{ kpc}, 25^\circ)$, respectively. *Bottom*: Same as the top panel but for the later time period

the velocity-space distributions at 648 points in the disc in the snapshots after $t = 7$ Gyr. Their positions in the galactocentric cylindrical coordinate are

$$\begin{cases} R = 6 \text{ kpc} + \Delta R \times i & (i = 0, \dots, 8), \\ \phi = -180^\circ + \Delta \phi \times j & (j = 0, \dots, 71), \\ z = 0 \text{ kpc}, \end{cases} \quad (4.3)$$

where $\Delta R = 0.5$ kpc and $\Delta \phi = 5^\circ$. We determine the velocity-space distribution for particles within 200 pc from each of the points and compute the KLD . We define that the velocity-space distribution in the simulation is similar to that in the solar neighbourhood if its KLD is less than 0.2. We select the threshold of 0.2 because the KLD of the velocity-space distribution for the particles within 200 pc from $(R, \phi) = (8 \text{ kpc}, 20^\circ)$ at $t = 10$ Gyr is ~ 0.2 . The velocity map is the one which we judged, by eye, to be similar to the map in the observation in Chapter 3. Fig. 4.4 shows the distribution of the KLD s at $t = 10$

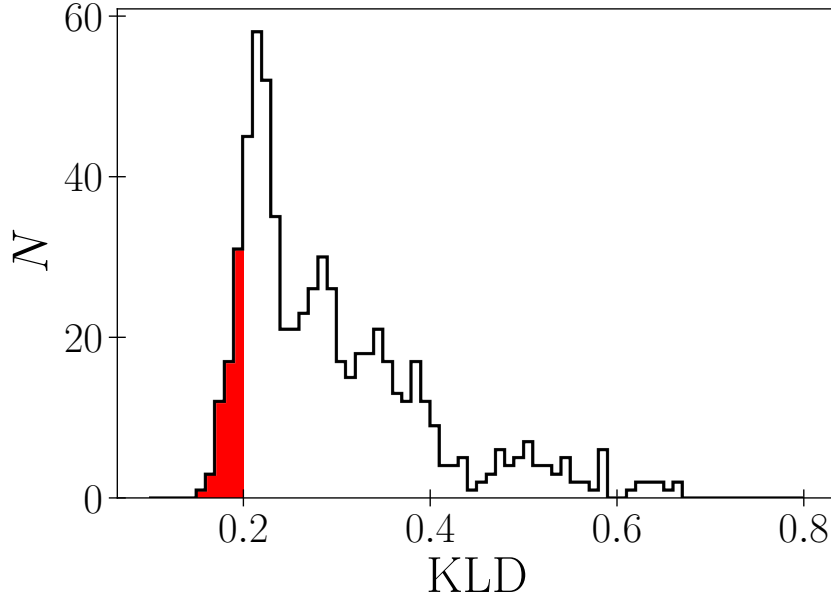


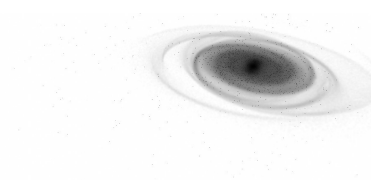
Figure 4.4: Distribution of the [KLDs](#) at $t = 10$ Gyr. The black line shows the histogram of the [KLDs](#) at all of the positions where the [KLDs](#) are computed. The region of $\text{KLD} < 0.2$ is filled with red.

Gyr. The velocity-space distributions whose [KLDs](#) lie in the red filled region ($\text{KLD} < 0.2$) have sufficiently high similarities.

Fig. 4.5 shows the number of the times that the [KLDs](#) less than 0.2 are detected at each position. Velocity-space distributions with these small [KLDs](#) are detected more frequently at $R = 8$ kpc and 8.5 kpc than the other radii. Especially around $(R, \phi) = (8 \text{ kpc}, 20^\circ)$ and $(R, \phi) = (8.5 \text{ kpc}, 50^\circ)$, the [KLDs](#) are smaller than 0.2 for more than 50% of the analysed snapshots from $t = 7$ to 10 Gyr. On the other hand, at $R \lesssim 7$ kpc or $R \gtrsim 9$ kpc the [KLDs](#) are larger than 0.2 for almost every snapshot.

[Fujii et al. \(2019\)](#) obtained similar results using a simpler analysis method. They fitted the sum of two Gaussian functions with the particle distributions in v_ϕ and detected two-peak (i.e. Hercules-like) features. Hercules-like features do not always appear at a fixed position. The detection frequency is at most 50% around $R \simeq 9$ kpc, which is slightly outside the 2:1 [OLR](#) radius. We only seldom detect velocity-space distributions similar to that in the solar neighbourhood around $R \simeq 9$ kpc. The difference may be due to that [Fujii et al. \(2019\)](#) focused only on one dimensional velocity (v_ϕ) distributions.

Fig 4.6 shows the ϕ dependence of the [KLD](#) more clearly. In the figure, we plot the histograms for the angles of positions where the [KLDs](#) are less than 0.2 at $R = 7.5$ kpc, 8 kpc, 8.2 kpc, 8.5 kpc and 9 kpc. As already seen in Fig. 4.5, these small [KLDs](#) are more frequently detected at $R = 8\text{--}8.5$ kpc. These values are close to distance between the Sun and the Galactic centre ([Bland-Hawthorn & Gerhard 2016](#)). The peaks of the histograms differ by R . The peak moves in the positive direction of ϕ as R increases. The peak of the histogram at $R = 8.2$ kpc locates at $\phi \simeq 30^\circ$, which is consistent with observationally suggested bar angle ([Bissantz & Gerhard 2002](#); [Rattenbury et al. 2007](#); [Cao et al. 2013](#); [Wegg & Gerhard 2013](#)). The R and ϕ dependence of the [KLD](#) also implies that the velocity-space distributions are related to bar resonances. Particles trapped in bar resonances do not distribute uniformly in the disc, instead their distributions are dependent on R and ϕ . ([Ceverino & Klypin 2007](#); [Khoperskov et al. 2020](#)).



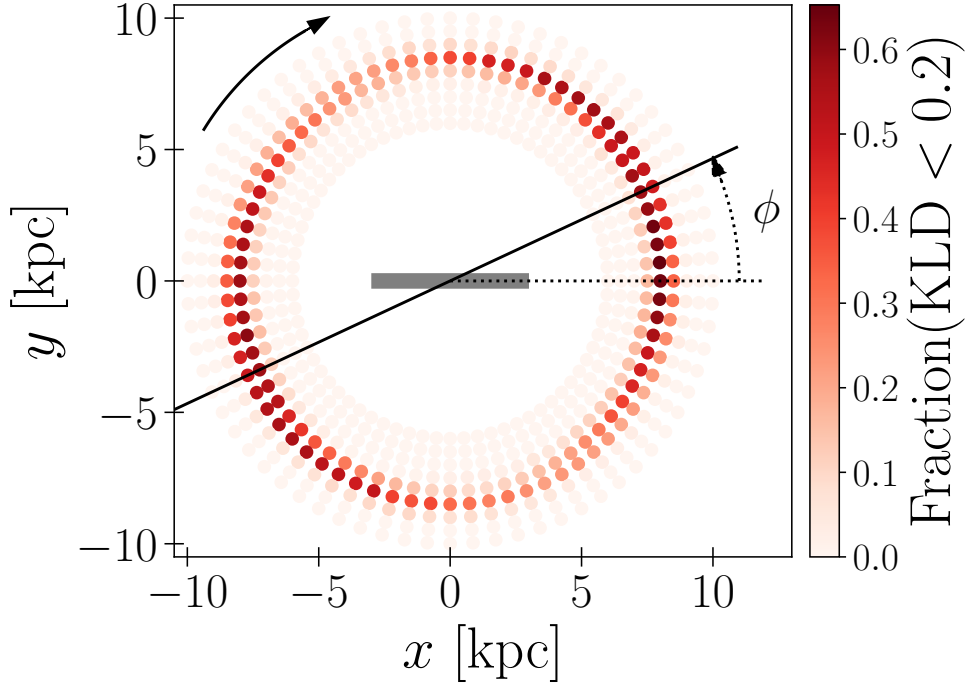


Figure 4.5: Positions where the velocity maps match that of the solar neighbourhood. The colours of the points represent the fractions of the number of times where **KLD**s less than 0.2 are detected at each position. The horizontal line and the solid arrow represent the bar orientation and the direction of the galaxy rotation, respectively. The black line represents the angle with respect to the bar of $\phi = 25^\circ$

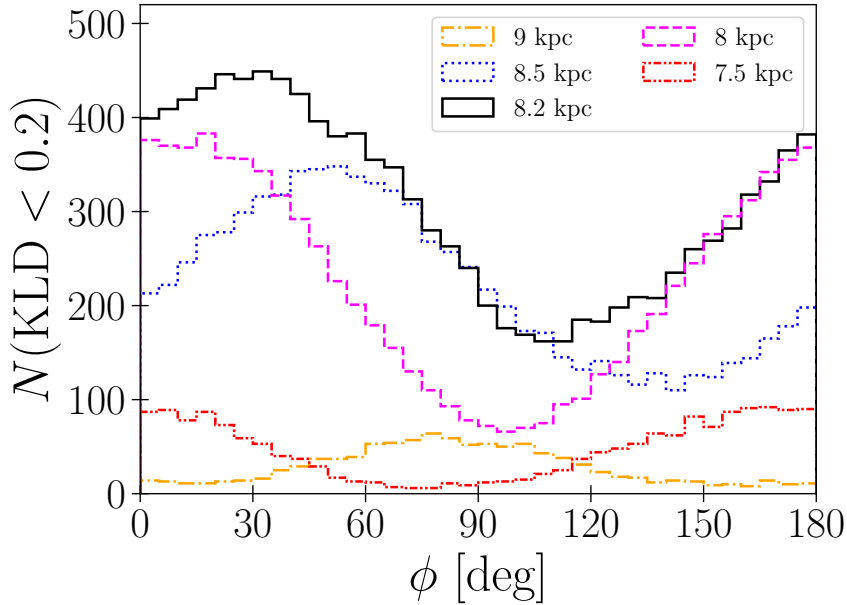


Figure 4.6: Histograms of the angles where the **KLD** of velocity distribution is less than 0.2. The angle ϕ is with respect to the bar. The red, magenta, black, blue and yellow lines show the histograms at $R = 7.5$ kpc, 8 kpc, 8.2 kpc, 8.5 kpc and 9 kpc, respectively.

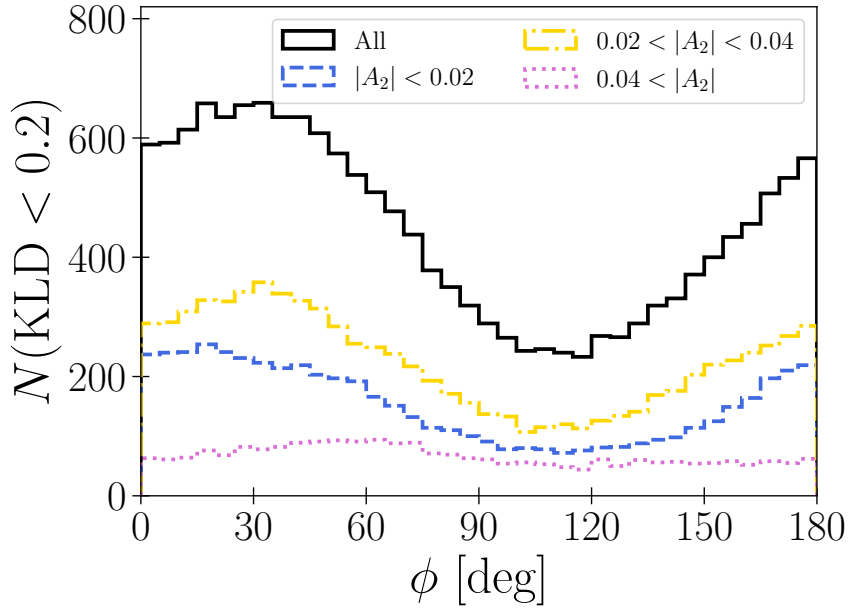


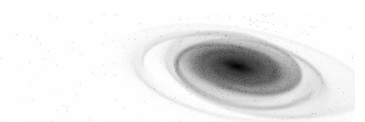
Figure 4.7: Histograms of the angles where the [KLD](#) of velocity distribution is less than 0.2. Blue, yellow and magenta lines show the histograms in the cases of weak ($|A_2| < 0.02$), intermediate ($0.02 < |A_2| < 0.04$) and strong ($0.04 < |A_2|$) spirals, respectively. The black line shows the histogram for all the spiral strength.

4.3.2.2 Angle with respect to the spirals

Not only the bar but also the spiral arms have impact on the stellar distribution and [KLD](#). We define the spiral position as a phase angle of Fourier $m = 2$ mode $\phi_2(R)$ and define the spiral strength as a Fourier amplitude $|A_2(R)|$. In Appendix C.1, the phase angles of $m = 2, 3$ and 4 modes are plotted on the density maps of the R - ϕ plane. The $m = 2$ mode traces the spiral arms better than the other modes. Fig. 4.7 shows the histograms for the ϕ of the positions with [KLD](#) < 0.2 for three spiral strength cases: $|A_2| < 0.02$, $0.02 < |A_2| < 0.04$ and $0.04 < |A_2|$. Here, the analysis is limited to the positions at $R = 8$ kpc and 8.5 kpc. The shape of the histograms depends on the spiral strength. The histogram of $0.02 < |A_2| < 0.04$ has a peak at $\phi \simeq 30^\circ$ and a valley at $\phi \simeq 110^\circ$. The histogram of $|A_2| < 0.02$ is less steep than the one of $0.02 < |A_2| < 0.04$. We see a plateau around $\phi = 0^\circ$ – 40° . The histogram of $|A_2| > 0.04$ is almost flat. When the spiral arm is strong, there is no specific angle where we often detect velocity distributions with small [KLDs](#). This indicates that the velocity-space distribution of the solar neighbourhood stars is not strongly influenced by spiral arms.

Fig. 4.8 shows the same histograms as Fig. 4.7 but now with respect to the spirals ($\phi - \phi_2$). The histogram for all the spiral strengths (black line) shows a peak around $\phi = 130^\circ$. The spiral positions are $\phi = 0^\circ$ and 180° , therefore the peak is at the inter-arm region, which is consistent with observations. [VLBI](#) observations suggest that the Sun is located in the inter-arm regions of the [MW](#)'s main spiral arms Perseus and Sagittarius-Carina ([Reid et al. 2019](#); [VERA Collaboration et al. 2020](#)). We note that the Sun may be close to the ‘Local Arm’, but that its features are not as clear as the Perseus or Sagittarius-Carina arms (see [Miyachi et al. 2019](#) and the references therein). The histograms in the cases of $|A_2| < 0.02$ and $|A_2| > 0.04$ are flatter than those of $0.02 < |A_2| < 0.04$.

It is unclear why the velocity-space distributions with small [KLDs](#) are more frequently detected in the inter-arm regions than in the arm regions. One possible explanation is that the spiral arms disrupt the velocity-space substructure as formed by the bar resonances. However, spiral arms can also form velocity-space substructures as shown in [Khoperskov & Gerhard \(2022\)](#) where direct imprints of the spiral arms appear as velocity-space substructures. In Section 4.4 we will see that the N -body model does not reproduce the detailed Hyades-Pleiades stream structures. Bar resonances cannot explain the origin of these structures and thus they may be due to the spiral arms.



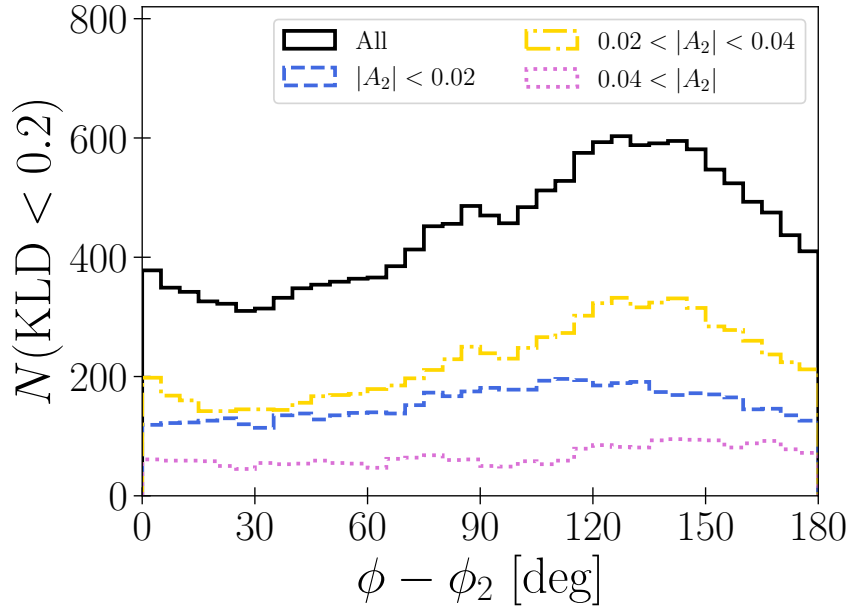


Figure 4.8: Same as Fig. 4.7 but now for the angle with respect to the spirals ($\phi - \phi_2$).

4.4 DISCUSSIONS

The previous section shows that the velocity-space distributions fluctuate with time in the simulation. However, some specific positions, namely $(R, \phi) \simeq (8 \text{ kpc}, 20^\circ)$, $(8.2 \text{ kpc}, 30^\circ)$ and $(8.5 \text{ kpc}, 50^\circ)$, frequently show velocity distributions similar to that in the solar neighbourhood. The (R, ϕ) dependence on the KLD implies that the bar resonances influence the velocity-space distribution. In this section, we discuss how the bar resonances impact the local velocity-space distributions at these positions.

Fig. 4.9 shows the velocity-space distributions for the particles within 200 pc from $(R, \phi) = (8 \text{ kpc}, 15^\circ)$ at $t = 9.29 \text{ Gyr}$. The KLD of this distribution is 0.145. This is one of the smallest values for the velocity-space distributions at $R = 8 \text{ kpc}$. The map in the top panel of Fig. 4.9 shows some substructures similar to that in Fig. 3.1. Hercules-like, horn-like, Sirius-like and hat-like structures locate at $(v_R, v_\phi) \simeq (10, 200) \text{ km s}^{-1}$, $(-50, 220) \text{ km s}^{-1}$, $(-50, 240) \text{ km s}^{-1}$ and $(0, 270) \text{ km s}^{-1}$, respectively. We compute the orbital frequencies of the particles around $(R, \phi) = (8 \text{ kpc}, 15^\circ)$ and select the ones trapped in bar resonances based on the frequency ratios as we did in Section 3.2.2. We mainly identify five resonances namely 2:1, 5:2, 3:1, 4:1 and 5:1 OLRs. The bottom panel of Fig. 4.9 shows their distributions in the velocity space. Cyan, yellow, green, magenta and orange dots indicate particles trapped in 2:1, 5:2, 3:1, 4:1 and 5:1 OLRs, respectively. The trajectories of the resonant orbits are shown in Appendix B. The Hercules-like stream is made from the 4:1 and 5:1 OLRs. Particles trapped in 2:1 and 3:1 OLRs contribute to the hat-like and horn-like structures respectively. In Chapter 3, we found the same correspondence between the resonances and the velocity-space substructures around $(R, \phi) = (8 \text{ kpc}, 20^\circ)$ at $t = 10 \text{ Gyr}$. Although the 5:2 OLR is not prominent at $t = 10 \text{ Gyr}$, there is still a large number of particles trapped in this resonance and they form a Sirius-like stream at $t = 9.29 \text{ Gyr}$.

Fig. 4.10 shows the same velocity-space distribution as Fig. 4.9 but now for the particles within 200 pc from $(R, \phi) = (8.5 \text{ kpc}, 50^\circ)$ at $t = 8.97 \text{ Gyr}$. The velocity-space distribution also has one of the smallest KLDs of ~ 0.145 . Visible in the top panel are Hercules-like, horn-like, Sirius-like and hat-like substructures. In this case, the horn-like, Sirius-like and hat-like substructures consist of particles trapped in 3:1, 5:2 and 2:1 OLRs, respectively. The bottom panel shows that the particles trapped in 4:1 and 5:1 OLRs are part of the Hercules-like stream, but the number of the particles in 5:1 OLR is smaller than that in Fig. 4.9. This is because $R = 8.5 \text{ kpc}$ is further from the 5:1 OLR radius. It is located at around $R \simeq 6.5 \text{ kpc}$ for the bar pattern speed of $\Omega_b \simeq 45 \text{ km s}^{-1} \text{ kpc}^{-1}$, which is the typical value for the latter epochs in our simulation.

The resonances of odd modes such as 3:1, 5:1 and 5:2 OLRs are due to the asymmetry of the bar potential, which is a natural consequence of N -body simulations. Most of the studies using test particle simulations assume symmetric bar potentials, whose Fourier decompositions include only even modes.

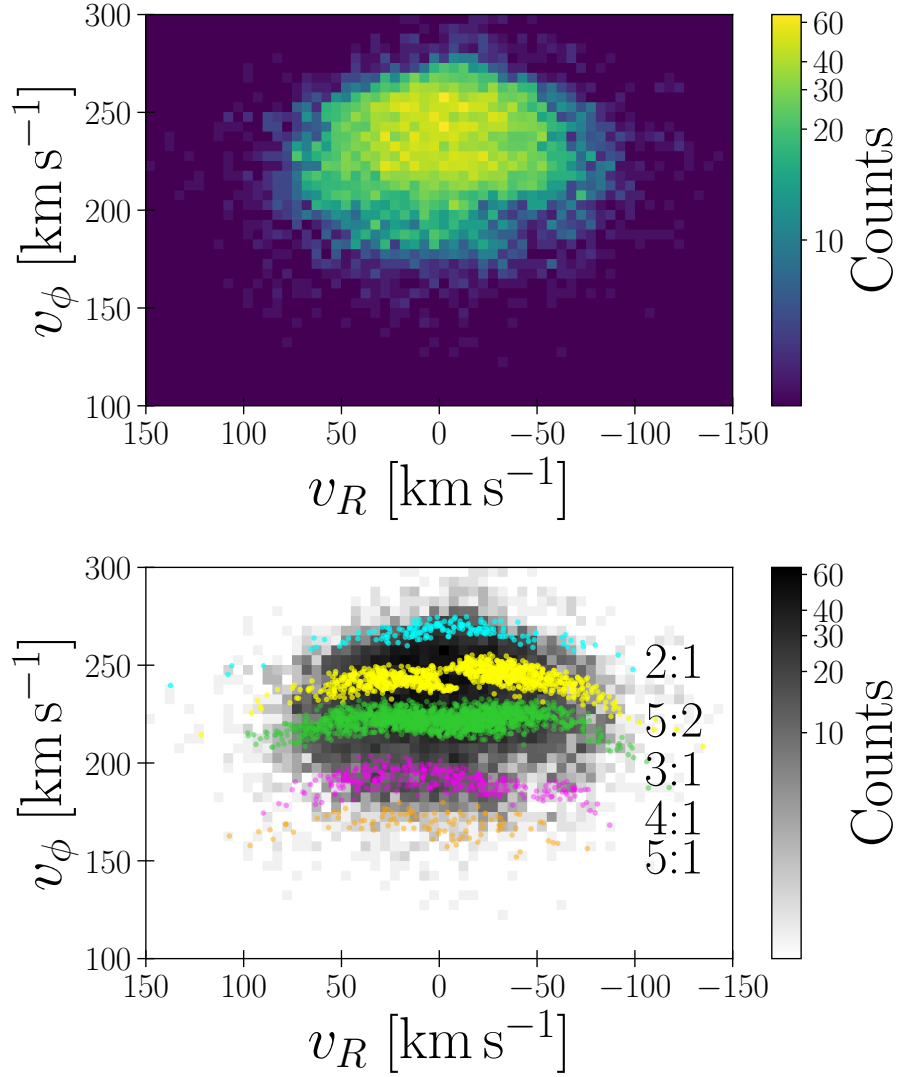
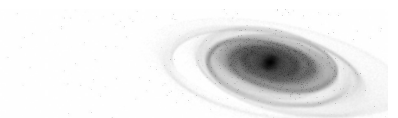


Figure 4.9: Velocity-space distribution for the particles within 200 pc from $(R, \phi) = (8 \text{ kpc}, 15^\circ)$ at $t = 9.29 \text{ Gyr}$. *Top:* The colours indicate number counts in each bin. The bin size is $5 \times 5 (\text{km s}^{-1})^2$. *Bottom:* Velocity-space distributions of the particles trapped in bar resonances. Cyan, yellow, green, magenta and orange dots indicate particles trapped in 2:1, 5:2, 3:1, 4:1 and 5:1 [OLRs](#), respectively.

Bars in N -body models are not completely symmetric, and therefore odd-mode resonances arise. [Monari et al. \(2019a\)](#) studied the impact of higher-order bar resonances on the velocity-space distribution of stars. The method used and the details of the results are different from ours. In both theirs and our models the hat is made from 2:1 [OLR](#). However, the correspondences between the other substructures and bar resonances are different from ours. In their model, Hercules, Serius and horn structures are made from [CR](#), 4:1 and 6:1 [OLRs](#), respectively. In their model the Galactic potential is based on the [M2M](#) method ([Portail et al. 2017](#)). The bar’s pattern speed is $\Omega_b = 39 \text{ km s}^{-1} \text{ kpc}^{-1}$, and the [CR](#) radius is located at $R \simeq 6 \text{ kpc}$. On the other hand, the [CR](#) radius of our N -body model is $R \simeq 5 \text{ kpc}$ and we do not observe particles in [CR](#) at $R \simeq 8\text{--}8.5 \text{ kpc}$. The bar potential of [Monari et al. \(2019a\)](#) comprises the Fourier components of $m = 2, 3, 4$ and 6 . The lack of the 5:1/5:2 [OLR](#) might be due to the lack of the $m = 5$ mode. The rotation curves (i.e. the axisymmetric component of the Galactic potential) also affect the distribution of the resonantly trapped stars.

Particles in the 3:1 [OLR](#) distribute on the Hyades-Pleiades region in addition to Horn. [Trick \(2022\)](#) also obtained a similar result that the location of 3:1 [OLR](#)’s resonance line is close to the ridge of Hyades and Horn in action space. The compact two peaks corresponding to Hyades and Pleiades respectively are not clearly identified in the density maps of Fig. 4.9 or Fig. 4.10. The residual maps in Fig. 4.11



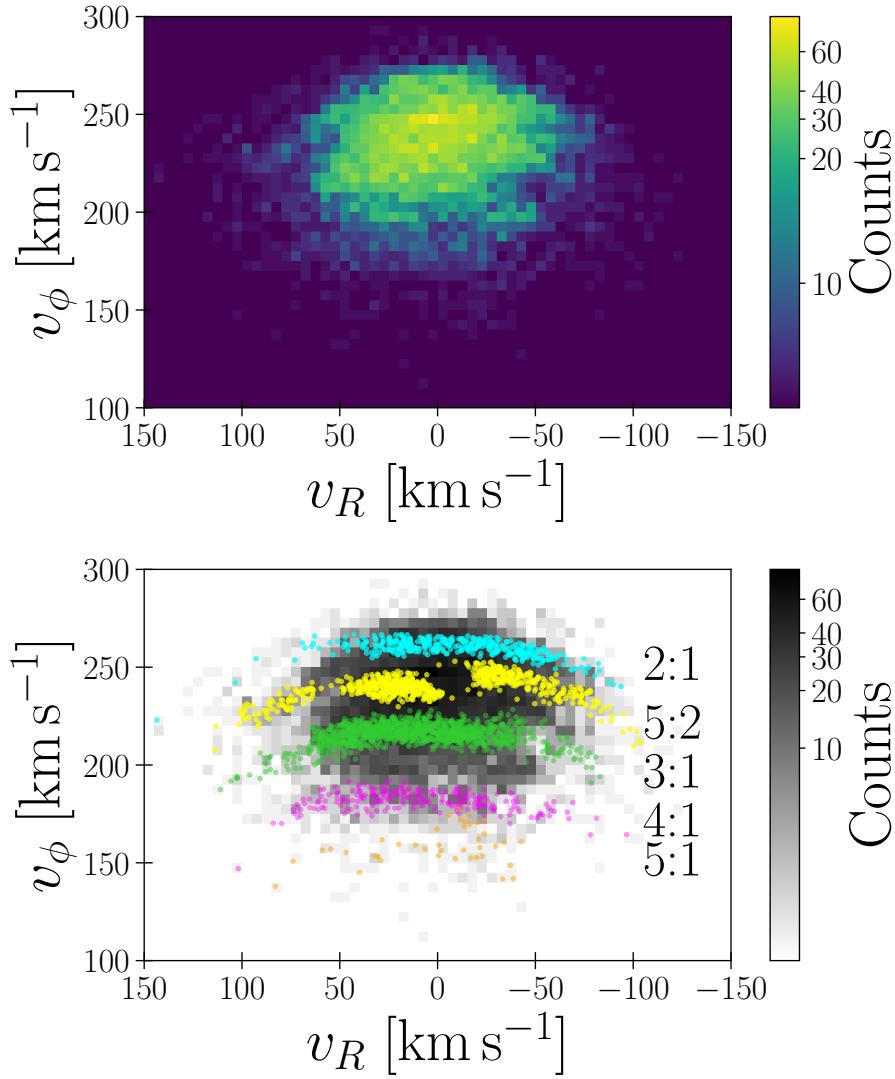


Figure 4.10: Same as Fig. 4.9 but for the particles within 200 pc from $(R, \phi) = (8.5 \text{ kpc}, 50^\circ)$ at $t = 8.97 \text{ Gyr}$.

highlight the differences of the velocity-space distributions between the observation and the simulation. The colours in the maps show the $q - p$ value at each of the points in the $\hat{v}_R - \hat{v}_\phi$ space. Here p and q are the probability distributions in the $\hat{v}_R - \hat{v}_\phi$ space derived from the *Gaia* and simulation data respectively. The upper and lower panels are the residual maps for the velocity-space distributions at $(R, \phi) = (8 \text{ kpc}, 15^\circ)$ at $t = 9.29 \text{ Gyr}$ (i.e. the top panel in Fig. 4.9) and $(R, \phi) = (8.5 \text{ kpc}, 50^\circ)$ at $t = 8.97 \text{ Gyr}$ (i.e. the top panel in Fig. 4.10), respectively. We see the dense blue regions from $(\hat{v}_R, \hat{v}_\phi) \simeq (0.2, 0.1)$ to $(0, -0.1)$ in both maps. These are the velocity-space substructures that are not reproduced by the N -body model. This may be due to the resolution limitation of the simulation. Another possibility is that they originate from mechanisms other than bar resonances such as spiral arms (Quillen & Minchev 2005; Michtchenko et al. 2018b; Barros et al. 2020).

Another difference between the velocity-space distribution in the observation and those in the simulation is the internal structure of the Hercules stream. *Gaia* data shows a trimodal structure for the Hercules stream, which is not seen in the simulation. The Hercules-like streams in our simulation consist of the two resonances of 4:1 and 5:1 OLRs but do not have a third component.

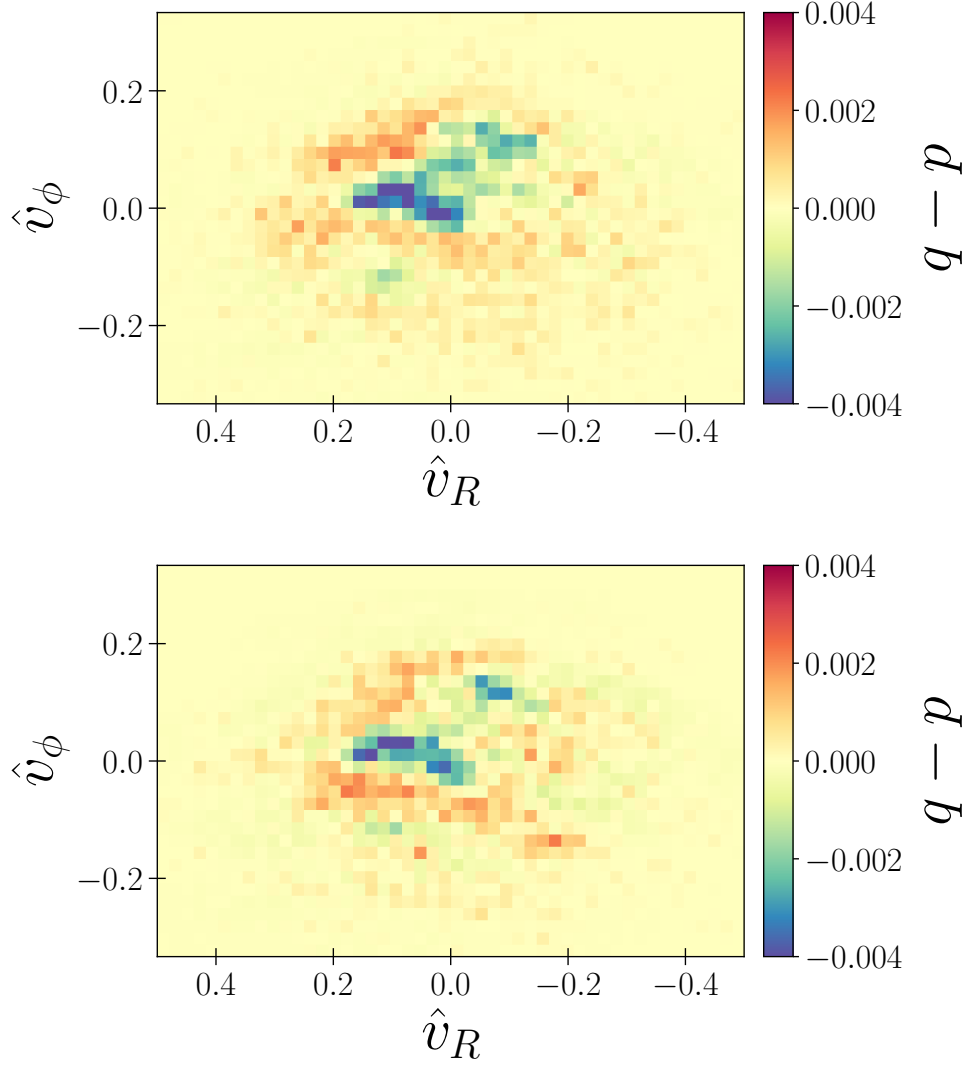


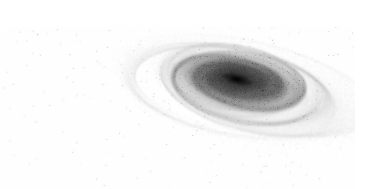
Figure 4.11: Residual maps of the simulated and observed \hat{v}_R - \hat{v}_ϕ space distributions. p and q are the probability distributions in the observation and the simulation, respectively, as defined in Section 4.2.3. *Top*: q is evaluated at $(R, \phi) = (8 \text{ kpc}, 15^\circ)$ at $t = 9.29 \text{ Gyr}$. *Bottom*: q is evaluated at $(R, \phi) = (8.5 \text{ kpc}, 50^\circ)$ at $t = 8.97 \text{ Gyr}$.

4.5 SUMMARY

In this chapter, we have quantitatively measured the similarities of velocity-space distributions using the **KLD**. We have evaluated the **KLDs** between the v_R - v_ϕ space distribution for the solar neighbourhood stars observed by the *Gaia* and those in an N -body MW model simulated by Fujii et al. (2019). The **KLDs** in the simulation show time evolution and spatial variation.

First, we have evaluated the **KLDs** at the three fixed points of $(R, \phi) = (7 \text{ kpc}, 25^\circ)$, $(8 \text{ kpc}, 25^\circ)$ and $(9 \text{ kpc}, 25^\circ)$. The time evolution of the **KLDs** are linked with bar's evolution. High **KLDs** (i.e. low similarities) at the beginning of the simulation reflect the initial condition. They drop rapidly around the bar formation epoch ($t \approx 3 \text{ Gyr}$). During the bar's slowing down phase ($3 \text{ Gyr} \lesssim t \lesssim 7 \text{ Gyr}$), they decrease with time. After the slowing down ($t \gtrsim 7 \text{ Gyr}$), the **KLDs** are almost constant but show small fluctuations. The small **KLDs** in this epoch indicate relatively high similarities. Especially, the **KLD** at $(R, \phi) = (8 \text{ kpc}, 25^\circ)$ is smaller than the other two positions. In this position of the simulation, we frequently but not always observe the velocity-space distributions similar to that of the solar neighbourhood.

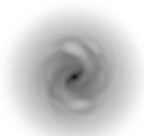
Next, we have investigated where in the disc we often detect velocity-space distributions similar to that in the solar neighbourhood. Velocity-space distributions with sufficiently high similarities (**KLD** < 0.2)



are frequently found in the range of $R = 8\text{--}8.5$ kpc. The detection frequency at $R \lesssim 7$ kpc and $R \gtrsim 9$ kpc are almost zero. The detection frequency depends also on ϕ . When R is fixed, there is a specific angle at which the small **KLDs** are detected most frequently. The peak angle moves in the direction of positive ϕ as R increases. Especially at $R = 8.2$ kpc, the peak is $\phi \simeq 30^\circ$. These R and ϕ are close to those of the Sun. Spiral arms also impact the velocity-space distribution. The (R, ϕ) dependence of the **KLD** is weakened when the spiral arms are strong. Furthermore, the velocity-space distributions with small **KLDs** are more frequently detected at the inter-arm regions than the arms regions.

We have investigated the relation between the bar resonances and the substructures in the velocity distributions with small **KLDs**. We have plotted the resonantly trapped particles in the velocity map at $(R, \phi) = (8 \text{ kpc}, 15^\circ)$ at $t = 9.29$ Gyr. We have performed the same analysis for the velocity map at $(R, \phi) = (8.5 \text{ kpc}, 50^\circ)$ at $t = 8.97$ Gyr. In both the cases, Hercules-like, horn-like, Sirius-like and hat-like substructure are confirmed. They are made from bar resonances. The Hercules-like streams consist of 4:1 **OLR** and 5:1 **OLR**. We obtained the same conclusion from the analysis of the final snapshot only in Chapter 3. Bar's higher order resonances as origin of the phase-space substructures are discussed in other recent studies (e.g. [Monari et al. 2017c](#); [Hattori et al. 2019](#); [Monari et al. 2019a](#); [Moreno et al. 2021](#); [Trick 2022](#)).

As the **KLD's** oscillation suggests, the velocity-space distribution at a fixed position largely fluctuates. However, even in the non-static model, the bar resonances have significant impact on the stellar velocity-space distribution. Spiral arms may weaken the underlying influence of the bar resonances and cause the fluctuation of the **KLD**. This is consistent with the result that the detection frequency of the small **KLD** is higher in the inter-arm regions than in the arm regions.



5.1 INTRODUCTION

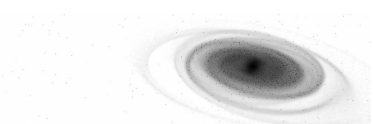
Since [Morgan et al. \(1952\)](#) first identified spiral arms in the [MW](#), their geometry, structure, and kinematics have been studied with various tracers ([Vallée 2017](#); [Shen & Zheng 2020](#)). Observations of OB stars and H II regions suggest that the [MW](#) is a four-arm spiral galaxy (e.g. [Georgelin & Georgelin 1976](#); [Urquhart et al. 2014](#)). The [VLBI](#) observations can measure trigonometric parallaxes of molecular masers associated with young massive stars and provide accurate distances to them ([Reid et al. 2014, 2019](#); [VERA Collaboration et al. 2020](#)). Based on these observations which support the four-arm model, the Sun is located between two main arms: the Perseus arm and the Sagittarius-Carina arm, and also close to a minor arm called the Local arm. The distribution of classical Cepheids shows similar pictures about the spiral geometry ([Skowron et al. 2019](#)). According to [Hou & Han \(2014\)](#), both three-arm and four-arm logarithmic spiral models can fit the tracers of H II regions, giant molecular clouds and 6.7 GHz methanol masers. On the other hand, observations of old stars in [IR](#) wavelength favour a two-stellar-arm model ([Drimmel 2000](#); [Benjamin et al. 2005](#); [Churchwell et al. 2009](#)). It is still challenging to fully map the global structures of spiral arms in the Galactic disc.

In a few kpc ranges from the Sun, we can study properties of the spiral arms based on the stellar distribution and kinematics thanks to the precise astrometry of *Gaia* ([Gaia Collaboration et al. 2016a](#)). [Miyachi et al. \(2019\)](#) cross-matched the *Gaia* [DR2](#) ([Gaia Collaboration et al. 2018a](#)) catalogue with the Two Micron All Sky Survey ([2MASS](#)) Point Source Catalogue ([Skrutskie et al. 2006](#)) and detected the overdensity of relatively old (~ 1 Gyr) stars at the Local arm. [Poggio et al. \(2021\)](#) mapped the overdensity of the young upper main sequence stars using *Gaia* [EDR3](#) ([Gaia Collaboration et al. 2021](#)) data. They estimated that the length of the Local arm is at least 8 kpc, which indicates that the Local arm is more significant than previously thought. Face-on maps of the mean in-plane, i.e. radial and tangential, velocities ([Eilers et al. 2020](#); [Martinez-Medina et al. 2022](#); [Gaia Collaboration et al. 2023b](#); [Almanna et al. 2023](#)) and the median radial action ([Palicio et al. 2023](#)) highlight spiral features.

Spiral arms affect not only planar motion but also vertical motion. They are considered to induce vertical bulk motion called the breathing mode ([Debattista 2014](#); [Faure et al. 2014](#); [Monari et al. 2016a,b](#); [Khachatryan et al. 2022](#); [Kumar et al. 2022](#)). The breathing mode is coherent vertical oscillation whose vertical velocity field is antisymmetric about the mid-plane. Previous studies (e.g. [Widrow et al. 2012](#); [Williams et al. 2013](#); [Gaia Collaboration et al. 2018b](#); [Carrillo et al. 2019](#); [Wang et al. 2020](#); [López-Corredoira et al. 2020](#); [Ghosh et al. 2022](#); [Widmark et al. 2022](#); [Ardèvol et al. 2023](#)) reported the breathing mode in the Galactic disc. [Ghosh et al. \(2022\)](#) discovered that the observed breathing amplitude increases with the height from the mid-plane. This trend is expected from the spiral-induced breathing mode ([Debattista 2014](#)). [Widmark et al. \(2022\)](#) reported a tentative evidence of the compressing breathing motion aligned with the Local arm.

The phase spirals are also linked to the bending and breathing modes. [Antoja et al. \(2018\)](#) identified a one-arm phase spiral in the *Gaia* [DR2](#) data ([Gaia Collaboration et al. 2018a](#)), while [Hunt et al. \(2022\)](#) discovered a two-arm phase spiral in the *Gaia* [DR3](#) data ([Gaia Collaboration et al. 2023a](#)), and these are associated with the bending and breathing modes, respectively. The bending mode can be reasonably explained by the passage of the Sagittarius dwarf galaxy. The breathing mode, on the other hand, can be substantially excited by the external perturbation only when the vertical velocity of the perturber is faster than that of the disc stars ([Widrow et al. 2014](#)). Theoretical approaches ([Banik et al. 2022, 2023](#)) based on the linear perturbation theory suggest that the bending mode dominates over the breathing mode in the solar neighbourhood and in the inner Galaxy in the case of the Sagittarius dwarf's passage. The two-arm phase spiral is likely to originate from internal perturbation, possibly induced by spiral arms ([Hunt et al. 2022](#); [Li et al. 2023a](#)).

In this chapter, we report that the compressing breathing mode is clearly associated with the Local arm in Section 5.2. In Section 5.3, we compare the observed breathing pattern with that seen in an N -body model of [MW](#)-like disc galaxy. We demonstrate that the breathing motion can infer the evolution phases



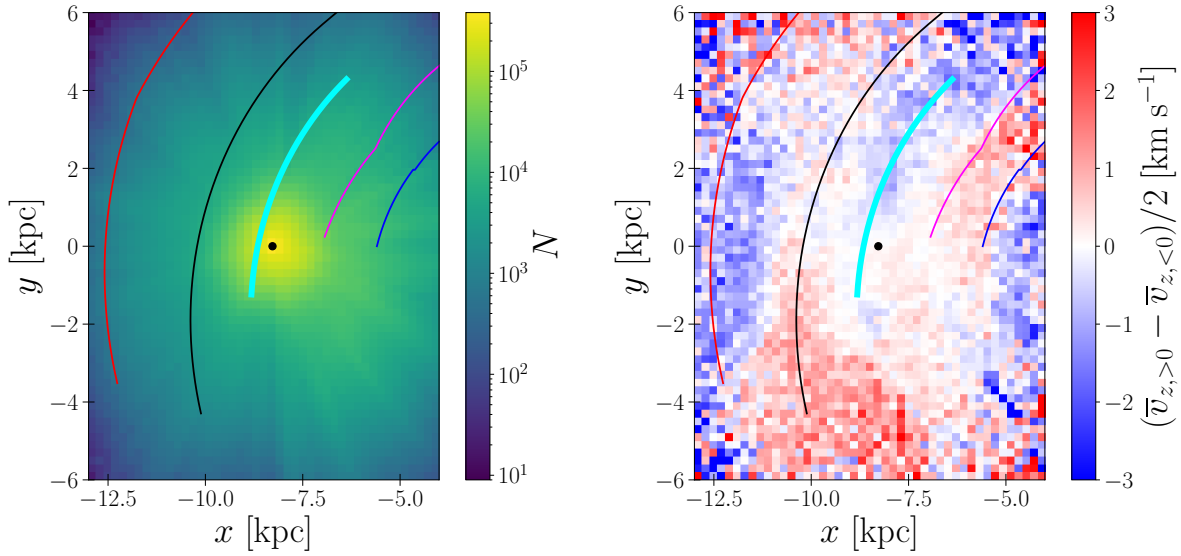


Figure 5.1: Face-on maps from the *Gaia* data. *Left*: Number counts. *Right*: Breathing velocity. Solid lines indicate the position of the spiral arms: Outer arm (red), Perseus arm (black), Local arm (cyan), Sagittarius–Carina arm (purple) and Scutum–Centaurus arm (blue), from Reid et al. (2019). The black dot indicates the position of the Sun.

of the spiral arms, and the compressing motion observed in the Local arm can be interpreted as the Local arm being in the growth phase. We provide our conclusion in Section 5.4.

5.2 THE BREATHING MOTION IN THE MILKY WAY DISC

We have selected stars from *Gaia* (Gaia Collaboration et al. 2023a) DR3 catalogue in the criteria described in 2.3.

Fig. 5.1 shows face-on maps of the Galactic disc made from the *Gaia* data. The left panel shows the number counts of the stars in each bin, whose size is 0.2×0.2 kpc². The right panel shows the breathing velocity $\frac{1}{2}(\bar{v}_{z,>0} - \bar{v}_{z,<0})$, where $\bar{v}_{z,>0}$ and $\bar{v}_{z,<0}$ are the mean vertical velocities of the stars within $0 < z < 1.5$ kpc and $-1.5 < z < 0$ kpc, respectively. The locations of the spiral arms are plotted as follows: Outer arm (red), Perseus arm (black), Local arm (cyan), Sagittarius–Carina arm (purple) and Scutum–Centaurus arm (blue). The locations are based on the spiral arms traced by the massive star-forming regions (Reid et al. 2019), but we add an offset of 0.127 kpc in the radial direction because they assume a Sun–Galactic centre distance different from ours. The number counts are significantly affected by the selection bias, and therefore, it is difficult to find intrinsic overdensity or underdensity from this map. On the other hand, the right panel exhibits some breathing patterns. The most distinct structure is a compression area (indicated by the blue colour) extending from the upper right corner of the panel to the point near the Sun. Remarkably, this pattern closely aligns with the Local arm highlighted with the cyan line in Fig. 5.1. This is likely indicating that the Local arm induces the compressing breathing mode.

The identical structure can be seen in the red giant branch (RGB) star sample in Fig. 23 of Gaia Collaboration et al. (2023b). They noted that the expanding breathing motion observed in their OB star sample could possibly align with the Local arm. However, the amplitude of this expansion is smaller than that of the compressing breathing motion seen in the RGB star sample. Additionally, the association with the arm is less distinct in the OB star sample when compared to the RGB star sample. Recently, Ardévol et al. (2023) reported a breathing mode in the $60^\circ \leq l \leq 75^\circ$ direction for the A star sample. They probably have captured the same structure in a different view, but they did not discuss the association with the spiral arm. Widmark et al. (2022) also discussed a tentative alignment between the Local arm and the compressing breathing mode. They highlighted the offset of the compressing breathing mode from their derived stellar density excess, which is not in the same location as where suggested in Reid et al. (2014). The true location of the Local arm is still in debate. Because our result shown in Fig. 5.1 presents even

more clear alignment with the Local arm position suggested by Reid et al. (2019) than previously shown, in this chapter we consider that the location of the Local arm is where suggested in Reid et al. (2019). In Section 5.3, we show that with this assumption the Local arm is well explained with the dynamic spiral arm scenario seen in N -body simulations.

While the Local arm exhibits a clear connection between the compressing breathing motion, the other spiral arms are more weakly associated with the breathing motion. The area between the Sagittarius–Carina arm and the Scutum–Centaurus arm exhibits the expanding breathing motion (indicated by the red colour). Outside of the Local arm, a large area of the expansion breathing mode exists, and it looks to partially coincide with the Perseus arm. We see compression zones in the outer Galaxy ($R \gtrsim 12$ kpc) and in the inner Galaxy ($R \lesssim 5$ kpc). The Outer arm passes through the outer one. The inner one is not associated with any spiral arms but is near the bar end. One possibility is that it is driven by the bar. Theoretical studies show that both bars and spiral arms can excite breathing mode (Monari et al. 2015, 2016b; Banik et al. 2023). However, this is beyond the scope of this chapter, and the further studies are encouraged.

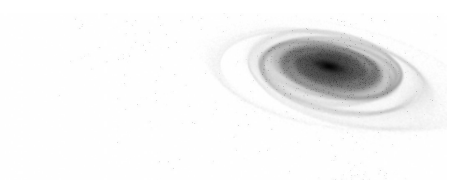
5.3 BREATHING MOTION IN AN N -BODY SIMULATION

We use an isolated MW-like N -body model, MWaB, simulated by Fujii et al. (2019). For more details on the simulations, see Chapter 2.

5.3.1 Breathing motion in an N -body simulation

The upper panels of Fig. 5.2 show a comparable plot to Fig. 5.1 created from the N -body model at $t = 4.216$ Gyr. The simulated galaxy has a bar, and the angle between its major axis and the x -axis is 25° , like the MW. However, the bar is small and does not appear in this plot. Regarding the local kinematics in the solar neighbourhood (Asano et al. 2020, 2022) and the global dynamical structure (Fujii et al. 2019), the snapshots in the later epoch ($t \gtrsim 8$ Gyr) of the simulation better reproduce the observed properties such as the local and bulge velocity dispersions of the MW. However, in this epoch, the spiral arms are fainter due to the dynamical heating of the disc. In this chapter, we focus on the spiral-induced breathing motion, therefore, we have analysed the earlier snapshots which show prominent spiral structure. We have selected the snapshot at $t = 4.216$ Gyr because it exhibits the spiral arm geometrically most similar to that around the Sun. The contour map in the bottom panel displays the normalised surface density $\Sigma(R, \phi)/\Sigma_0(R)$, where $\Sigma(R, \phi)$ and $\Sigma_0(R)$ are the surface density and the azimuthally averaged surface density profile, respectively. To estimate $\Sigma_0(R)$, we calculate the averaged surface densities for 40 annuli between $R = 5$ kpc and 13 kpc and fit them with an exponential profile. The fitted scale radius of 2.4 kpc is comparable to that for the initial condition of the stellar disc. The same contour is overplotted on the upper panels. The top right shows the breathing velocity. The breathing mode is clearly correlated with the spiral arms. The compression mode and the expansion mode appear in the arm and inter-arm regions, respectively. In the outer galaxy, the arms are weak and the breathing velocity is almost zero.

The top right panel of Fig. 5.2 shows that the spiral arm seen in the middle of the panel is qualitatively similar to what is seen around the Local arm in the right panel of Fig. 5.1, although the amplitude of the breathing velocity is smaller than the observed one. The *Gaia*’s selection bias can explain this difference. The intrinsic amplitude of the spiral-induced breathing mode should increase with height from the mid-plane (Debattista 2014), and this trend has been partially confirmed in the *Gaia* DR2 data (Gaia Collaboration et al. 2018b; Ghosh et al. 2022). In the *Gaia* data, stars at higher height from the mid-plane are preferentially sampled at the region of the further distance from the Sun, because the completeness of the *Gaia* data is lower at low Galactic latitudes at a farther distance due to the dust extinction. As a result, a higher amplitude of the breathing velocity is expected. In fact, the breathing amplitude in the solar neighbourhood ($\lesssim 1$ kpc) is smaller than in the distant region because the data are more complete in the mid-plane. In Appendix D, we demonstrate how the selection bias affects the observed breathing amplitude.



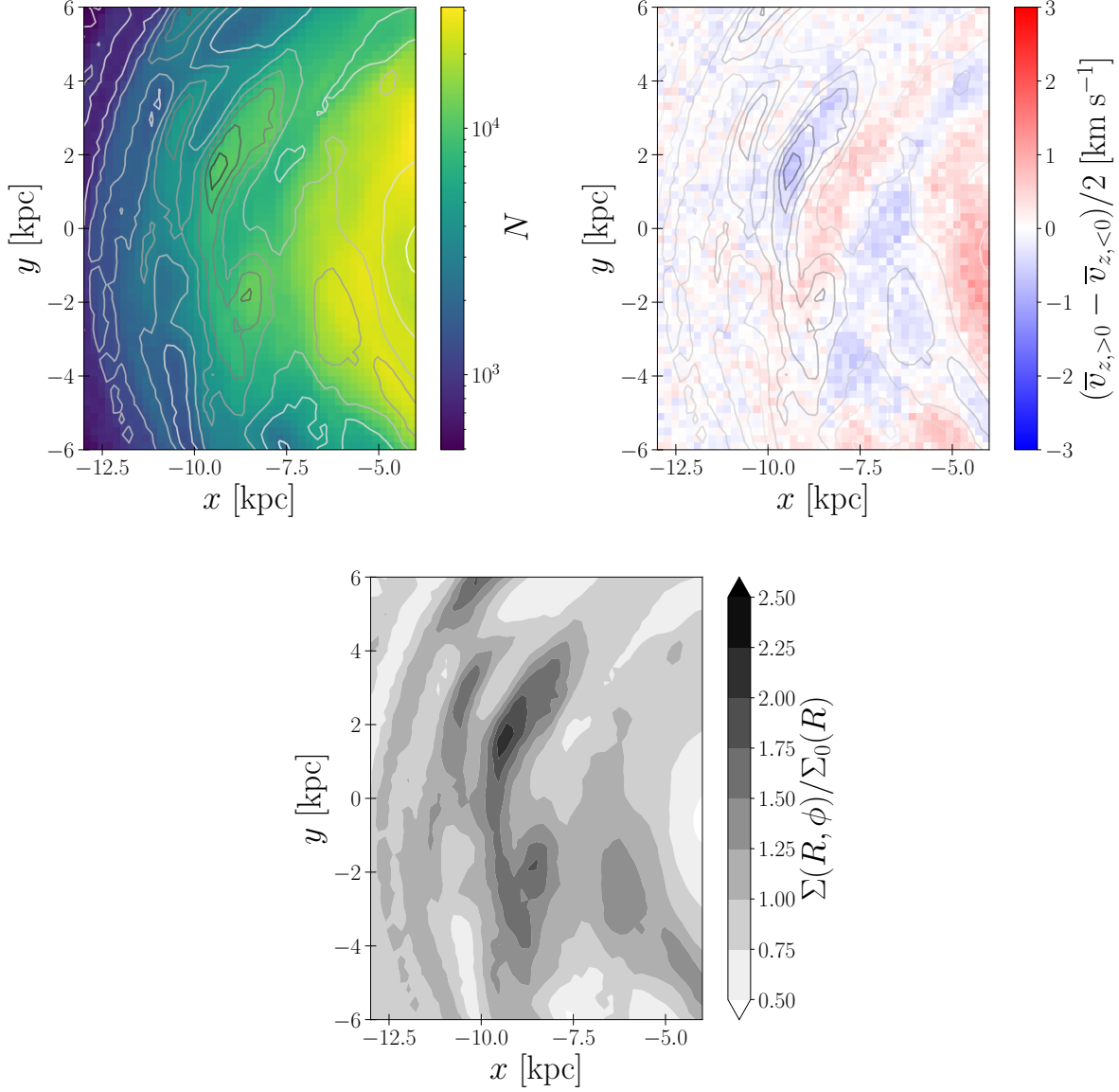


Figure 5.2: Face-on maps from the N -body model. *Top left panel* shows the number counts. *Top right panel* shows the breathing velocity. *Bottom panel* shows the contour map of the normalised surface density $\Sigma(R, \phi) / \Sigma_0(R)$, where $\Sigma(R, \phi)$ and $\Sigma_0(R)$ are the 2D surface density and the exponential surface density, respectively. The same contours are shown in the other two panels. We assume the “Sun” is located at $(x, y) \sim (-8.5, 0)$ kpc.

5.3.2 Time evolution of spiral arms and breathing mode

We further investigate how the dynamic spiral arms and breathing mode in the N -body model evolve with time. In Fig. 5.3 we present the normalised surface density $\Sigma(R, \phi) / \Sigma_0(R)$ (first row) and the breathing velocity $\frac{1}{2}(\bar{v}_{z, > 0} - \bar{v}_{z, < 0})$ (second row) around the spiral arm located at the centre of Fig. 5.2 for ten sequential time steps ranging from $t = 4.126$ Gyr to 4.214 Gyr. These maps are shown in a frame rotating at an angular velocity of $27 \text{ km s}^{-1} \text{ kpc}^{-1}$, which is the circular frequency at $R \sim 9 \text{ kpc}$. The galaxy rotates in the direction in which ϕ decreases. The first (left-hand) and last (right-hand) five columns correspond to the growth and disruption phases of this highlighted spiral arm, respectively. We trace the peak surface density (indicated by blue points in the top panels) and the breathing velocity there and present their time evolution in the bottom panel of Fig. 5.3. The amplitude of the compressing breathing mode at the arm region increases as the arm grows. At the same time, a large expansion of breathing velocity appears at the trailing side of the arm. The compressing amplitude decreases rapidly during the disruption phase. In the

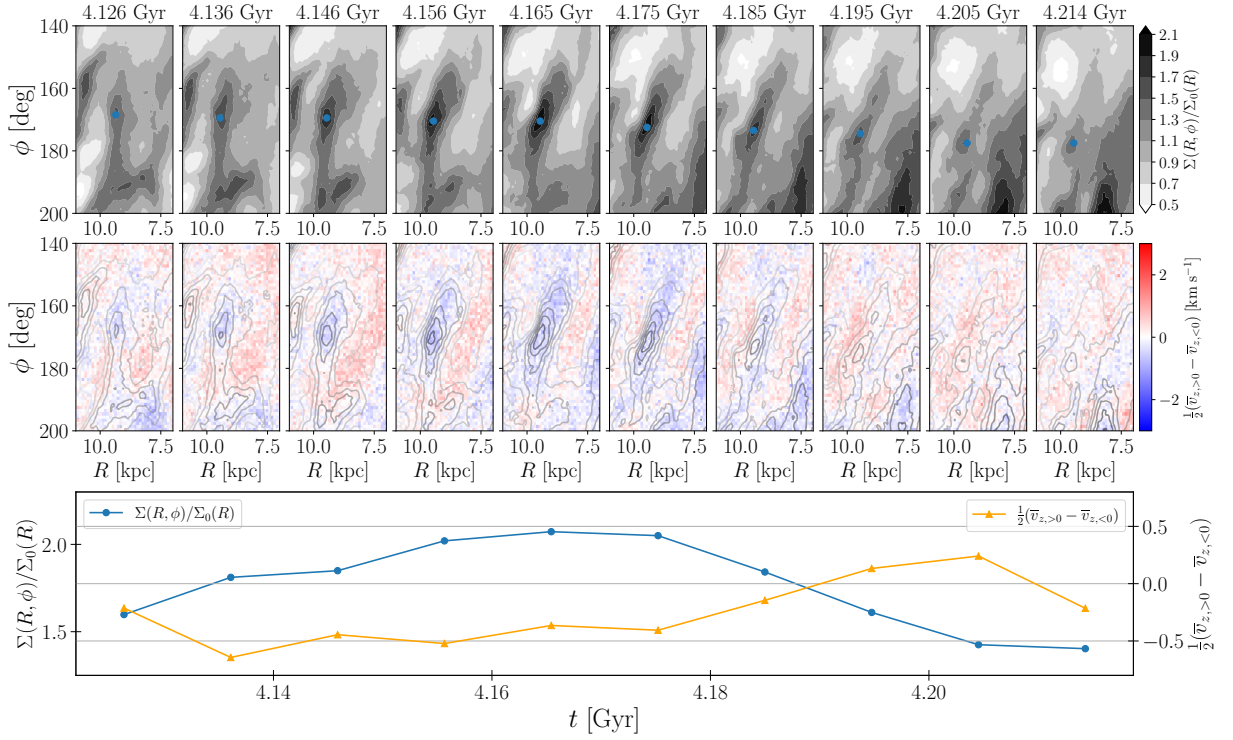


Figure 5.3: Time evolution of a spiral arm and the associated breathing motion. *Top panels* shows the normalised surface density in the ten snapshots between $t = 4.126$ Gyr and 4.214 Gyr. The density maps are shown in the frame rotating with the circular frequency at $R \sim 9$ kpc on R - ϕ plane. The galaxy rotates in the direction in which ϕ decreases. *Middle panels* shows the breathing velocity. The contours of the upper panels are overplotted. *Bottom panel* shows the normalised surface density and the breathing velocity at the points indicated by blue dots in the top panels as functions of time.

last three snapshots ($t = 4.195$, 4.205 and 4.214 Gyr), both the spiral arm and breathing mode become weaker. The breathing mode reaches almost zero. In the last snapshot, the spiral arm almost disappears, but is still identifiable. Hence, the dynamic spirals have almost no correlation with the breathing motion in the disrupting phase.

The previous theoretical studies of the breathing mode due to the spiral arms were based on the density-wave theory of the spiral arm. [Debattista \(2014\)](#) showed that stars move towards (away from) the mid-plane when they enter (leave) the spiral arms, if the spiral arms are like density-wave, and the stars rotate with significantly different speed from the pattern speed of the spiral arms. Therefore, the compressing (expanding) breathing mode appears at the trailing (leading) side of the arm inside the corotation radius, and the opposite trend appears outside the corotation radius. They confirmed this phenomenon through investigation in an N -body disc model which has grand-designed spiral arms with a well-defined single pattern speed. In an analytical model ([Monari et al. 2016a](#)) and test particle simulations ([Faure et al. 2014](#); [Monari et al. 2016a](#)), it is also shown that stellar motion is compressing and expanding at the trailing and leading sides, respectively, when the corotation radius is at outside of the disc.

Contrary to these previous studies, in our model, the compressing motion is confined to the arm, and there is no systematic displacement. This is because in our simulation the spiral arms are transient and dynamic spiral arms, as seen in many N -body simulations (e.g. [Sellwood & Carlberg 1984](#); [Baba et al. 2009, 2013](#); [Fujii et al. 2011](#); [Wada et al. 2011](#); [Grand et al. 2012a,b](#); [D’Onghia et al. 2013](#); [Baba 2015](#)). In the dynamic spiral arms, the spiral-arm features co-rotate with the disc stars at every radius. Hence, as a result, the compression due to the spiral arms coincides with the density contrast of the spiral arm, unlike the offset expected from the density wave-like spiral arms.

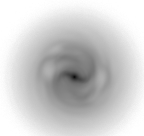
The alignment between the Local arm and the compression mode in the Gaia data in Fig. 5.1 is striking. Note that in this study the arm position are determined not from the *Gaia* data but from the VLBI

observations (Reid et al. 2019), but for the Local arm there is no significant displacement between the arm location traced by high-mass star-forming regions and that by old stars (Miyachi et al. 2019). Based on the result of our simulation and similarity to the observed trend, we are tempted to suggest that the Local arm is a spiral arm strong enough to induce the compressing breathing mode, and it is a co-rotating dynamic arm like what we can find in the N -body simulations. Then, the compressing breathing motion in the Local arm indicates that the Local arm is in the growth phase of the dynamic arm.

5.4 DISCUSSION AND CONCLUSION

In this chapter, we have reported the detection of the breathing mode associated with the spiral arms, especially the striking coincidence of the compression mode in the Local arm, in the *Gaia* data. We have also identified a similar compressing breathing pattern in growing spiral arms in the isolated N -body disc model. If the real spiral arms of the MW are similar to this dynamic nature, we can conclude that the observed compressing breathing motion aligned well with the Local arm infers the growth phase of dynamic spiral arms. The strong compressing breathing feature in the Local arm also indicates that the Local arm is not a minor spiral arm but a major strong arm that influences even the vertical velocity field of the stars.

In contrast to the Local arm, the Perseus arm has almost no correlation with the breathing mode although it looks to partially coincide with the expanding breathing mode (see the right panel of Fig. 5.1). This implies that the Perseus arm is in the disrupting phase. Baba et al. (2018) discovered that velocities of classical Cepheids around the Perseus arm show a sign of the disruption phase expected from the dynamic spiral arm model (Baba et al. 2013; Baba 2015). Applying the same inference from our N -body simulation result, the Outer arm can be considered as a growth phase. This may indicate that the MW harbours the different phases of the dynamic spiral arms, which is naturally seen in N -body simulations (Funakoshi et al. 2024). We note that inferring the evolutionary phases of the arms in the inner Galaxy is more challenging, because they are near the bar end, and the combined effect of the spiral arms and the bar makes the vertical stellar motion more complex (Monari et al. 2016b). Further studies of the impacts of interference between the bar and spiral arms to the vertical motions are encouraged to comprehensively understand the fascinating nature of the Galactic disc structure.



BENDING AND BREATHING MOTIONS OF THE GALACTIC DISC INDUCED BY DWARF GALAXIES

本章については、5年以内に雑誌などで刊行予定のため、非公開。



SUMMARY AND CONCLUSIONS

7.1 SUMMARY

ESA's *Gaia* mission has been providing us with unprecedented astrometry data of the MW stars. They have revealed the phase-space structure of the MW disc in great detail. We have investigated the relation between the phase-space structures and the internal and external perturbations using high-resolution N -body simulations. We have discussed the present-day dynamical structure of the MW disc and its time evolution comparing the phase-space structures in the simulations with those in the *Gaia* data. Summary of each chapter is as follows.

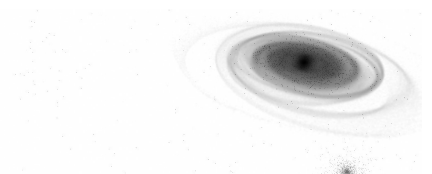
In Chapter 3, we have analysed an isolated N -body simulation of a MW-like galaxy performed by Fujii et al. (2019) in order to investigate the origins of velocity-space substructures. We have investigated the distribution of particles in the v_R - v_ϕ space in the final snapshot ($t = 10$ Gyr), and have found a Hercules-like stream at $(R, \phi) = (8 \text{ kpc}, 20^\circ)$. From a frequency analysis of stellar orbits, we have detected mainly four resonances, namely the 2:1, 3:1, 4:1 and 5:1 OLRs of the bar around there. The observed structures in the v_R - v_ϕ plane can be explained by stars being trapped in the 4:1 and 5:1 OLRs. In our simulations, these resonances give rise to structures similar to those observed in the actual Hercules stream. Our results therefore favour that the Hercules stream is composed of stars trapped in the 4:1 and 5:1 OLR and CR, which would also explain its trimodal structure as revealed by *Gaia* data. In addition, the stars in the 2:1 and 3:1 OLR match the 'hat' and 'horn' structures, respectively.

We further compared the distribution of stars in the R - v_ϕ plane in our simulation with that obtained from the *Gaia* data. Particles identified to be in resonance in our simulation follow ridges in the R - v_ϕ plane. Similar ridges have also been found in the *Gaia* data and matching the observed ridges to resonances, our results suggest a relatively low pattern speed of the MW's bar, namely $\Omega_b = 1.4$ – $1.55\Omega_0$, which corresponds to 40 – $45 \text{ km s}^{-1} \text{ kpc}^{-1}$. This is consistent with recent studies (e.g. Sanders et al. 2019; Bovy et al. 2019).

In Chapter 4, we have investigated the time evolution and spatial variation of the velocity-space distribution, and persistency of the velocity-space substructures. We have quantitatively measured the similarities of velocity-space distributions using the KLD. We have evaluated the KLDs between the v_R - v_ϕ space distribution for the solar neighbourhood stars observed by *Gaia* and those in the same N -body MW model used in Chapter 3.

First, we have evaluated the KLDs at the three fixed points of $(R, \phi) = (7 \text{ kpc}, 25^\circ)$, $(8 \text{ kpc}, 25^\circ)$ and $(9 \text{ kpc}, 25^\circ)$. The time evolution of the KLD is linked with the bar's evolution. The high KLDs (i.e. low similarities) at the beginning of the simulation reflect the initial condition. They drop rapidly around the bar formation epoch ($t \approx 3$ Gyr). During the bar's slowing down phase ($3 \text{ Gyr} \leq t \leq 7 \text{ Gyr}$), they decrease with time. After the slowing down ($t \gtrsim 7 \text{ Gyr}$), the KLDs are almost constant but show small fluctuations. The small KLDs in this epoch indicate relatively high similarities. Especially, the KLD at $(R, \phi) = (8 \text{ kpc}, 25^\circ)$ is smaller than the other two positions. In this position of the simulation, we frequently but not always observe the velocity-space distributions similar to that of the solar neighbourhood.

Next, we have investigated where in the disc we frequently detect velocity-space distributions similar to that in the solar neighbourhood. Velocity-space distributions with sufficiently high similarities ($\text{KLD} < 0.2$) are frequently found in the range of $R = 8$ – 8.5 kpc . The detection frequency at $R \lesssim 7 \text{ kpc}$ and $R \gtrsim 9 \text{ kpc}$ are almost zero. The detection frequency depends also on ϕ . When R is fixed, there is a specific angle at which the small KLDs are detected most frequently. The peak angle moves in the direction of positive ϕ as R increases. Especially at $R = 8.2 \text{ kpc}$, the peak is $\phi \approx 30^\circ$. This R and ϕ are close to those of the Sun. Spiral arms also impact the velocity-space distribution. The (R, ϕ) dependence of the KLD is weakened when the spiral arms are strong. Furthermore, the velocity-space distributions with small KLDs are more frequently detected at the inter-arm regions than the arms regions.



Finally, we have investigated the relation between the bar resonances and the substructures in the velocity distributions with small **KLDs**. We have plotted the resonantly trapped particles in the velocity map at $(R, \phi) = (8 \text{ kpc}, 15^\circ)$ at $t = 9.29 \text{ Gyr}$. We have performed the same analysis for the velocity map at $(R, \phi) = (8.5 \text{ kpc}, 50^\circ)$ at $t = 8.97 \text{ Gyr}$. In both cases, Hercules-like, horn-like, Sirius-like and hat-like substructures are confirmed. They are made from bar resonances. The Hercules-like streams consist of 4:1 **OLR** and 5:1 **OLR**. This is consistent with our finding in Chapter 3

As the **KLD**'s oscillation suggests, the velocity-space distribution at a fixed position largely fluctuates. However, even in the non-static model, the bar resonances have a significant impact on the stellar velocity-space distribution. Spiral arms may weaken the underlying influence of the bar resonances and cause the fluctuation of the **KLD**. This is consistent with the result that the detection frequency of the small **KLD** is higher in the inter-arm regions than in the arm regions.

In Chapter 5, we target spiral arms and the breathing motion induced by them. We have found a coincidence between the compression mode and the location of the Local arm in the *Gaia* data. We have also identified a similar compressing breathing pattern in growing spiral arms in the isolated N -body disc model. If the real spiral arms of the **MW** are similar to this dynamic nature, we can conclude that the observed compressing breathing motion aligned well with the Local arm infers the growth phase of dynamic spiral arms. The strong compressing breathing feature in the Local arm also indicates that the Local arm is not a minor spiral arm but a major strong arm that influences even the vertical velocity field of the stars. In contrast to the Local arm, the Perseus arm has almost no correlation with the breathing motion. This implies that the Perseus arm is in the disrupting phase.

In Chapter 6, we have performed an N -body simulation of a **MW**-like galaxy perturbed by a Sagittarius dwarf (Sgr)-like satellite to explore the influences of the external perturbation on the phase-space structure of the galactic disc. Close encounters with the dwarf excite the bending oscillation of the galactic disc and tidally induced spiral arms. These bending oscillations and tidally induced spiral arms form characteristic phase-space structures, such as ridges in R - v_ϕ space. In the z - v_z space, both one-arm (bending) and two-arm (breathing) phase spirals are observed.

We have performed Fourier analysis of the bending mode, breathing mode and disc surface density. The analysis has revealed distinct time evolutions for the bending mode and breathing mode. The bending mode decays more rapidly than the breathing mode, and the decay time scale of the bending mode increases with R , whereas that of the breathing mode exhibits weaker dependence on R . This difference in decay time scales results in the transition of the dominant mode from the bending mode to the breathing mode, and the transition of the dominant mode propagates from the inner galaxy to the outer galaxy.

In addition to the Fourier analysis, we have performed the spectral analyses. For the breathing mode and surface density, the dominant Fourier mode is $m = 2$. The breathing mode and share the same pattern speeds, indicating that the breathing mode is excited by density waves (the bar and spiral arms).

In the *Gaia* data, two-armed phase spirals are observed only for stars with guiding radii of $R_g \lesssim 7 \text{ kpc}$ (Hunt et al. 2022). This observational result and our findings suggest that the **MW** disc was externally perturbed a few hundred million years ago and is currently in a transitional phase from a bending-dominated disc to a breathing-dominated disc.

In this thesis, we have explored the impact of both internal and external perturbations on the dynamical structure of the **MW** disc through the lens of galactic seismology. The distribution of stars in 6D phase space results from various perturbations, forming a complex structure that is challenging to understand comprehensively. Nevertheless, the substructure due to each perturbation has a characteristic geometry and scale, allowing us to study them individually by extracting lower-dimensional spaces. As summarised above, this thesis has focused on the local velocity map, the breathing map and the vertical phase-space map. By comparing these phase space maps in the *Gaia* data and those in the N -body simulations, we gained insights into the bar, spiral arms and external perturbations.

7.2 THE FUTURE

7.2.1 Combined effects of the internal and external perturbations

Vasiliev & Belokurov (2020) analysed stellar kinematics and 3D structure of the Sgr using the astrometric and photometric data from *Gaia* and other surveys. They estimated that the current mass of the Sgr is $\sim 4 \times 10^8 M_\odot$ by comparing of the observed kinematic structure of the Sgr and those in a large suite of N -body simulations. On the other hand, according to the analytical calculations by Binney & Schönrich (2018), the Sgr's mass required to reproduce the observed phase spiral of the MW disc is $\gtrsim 2 \times 10^{10} M_\odot$. In a series of N -body simulations by Bennett et al. (2022), Sgr models with an initial mass of $1 \times 10^{10} M_\odot$ do not form clear phase spirals.

To address this discrepancy in the estimated mass of Sgr, one possible solution is to consider the combined effect of the internal and external perturbations. In Fig. ??, we saw a bending motion near the bar end radius, potentially resulting from the bar's structural evolution induced by the external perturbation. This thesis used a disc model with a well-developed bar, but when the bar is in its growth phase, stronger influences of external perturbation on the bar might be observable, even if a perturber is less massive. For a comprehensive understanding of the impact of dwarf perturbations on the Galactic bar, it is crucial to perform simulations of discs with bars at various evolution stages.

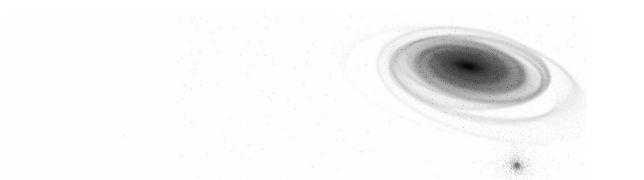
7.2.2 NIR astrometry surveys

Two NIR space astrometry missions are planned. One of them is the Japan Astrometry Satellite Mission for INfrared Exploration (*JASMINE*) mission (Gouda 2011, 2012, 2018; Yamada et al. 2015; Gouda & Jasmine Team 2020; Kawata et al. 2023). The other one is the *Gaia*NIR mission (Hobbs et al. 2016; Hobbs & Høg 2018) led by ESA. While *Gaia* cannot observe the inner part of the Galactic disc, where the dust extinction is severe, the observation data at NIR wavelengths from the future missions will provide us with more complete 6D phase-space information of stars in the MW disc. The degeneracy between the bar pattern speed and types of resonances is the major reason why the origins of the velocity-space substructures such as the Hercules stream are still controversial. Kawata et al. (2021) concluded that bar pattern speeds of $\Omega_b = 34 \text{ km s}^{-1} \text{ kpc}^{-1}$ and $\Omega_b = 42 \text{ km s}^{-1} \text{ kpc}^{-1}$ can explain phase-space substructures in the solar neighbourhood by bar resonances. The NIR astrometry data will help us to break this degeneracy. If we can detect the signatures of the bar resonances in a wide R range, we can constrain the bar pattern speed and the origins of the velocity-space substructures simultaneously.

7.2.3 Chemodynamicaics of the Milky Way disc

The Sgr not only has dynamical influences on the MW disc but can also induce chemical evolution. Ruiz-Lara et al. (2020) found episodic star formation enhancements in the MW disc at $t = 5.9, 1.9$ and 1.0 Gyr ago. They suggested that the timing of the star formation enhancements coincides with the Sgr's pericentre passages. Carr et al. (2022) suggested that the perturbation by the Sgr triggers the radial migration of stars in the MW disc.

Chemical abundances are important in estimating the birthplaces of stars. The Subaru Prime Focus Spectrograph (PFS) survey (Takada et al. 2014) will provide us with the chemical abundances and radial velocities of the disc stars. By combining the PFS data with the *Gaia* data, we will be able to make a chemodynamical map of the MW disc, which will offer insights into the evolution history of the MW. To interpret observation data, theoretical counterparts of the MW are necessary. These counterparts should contain both chemical and dynamical information. N -body/hydrodynamical simulations that include baryonic physics, such as star formation and feedback, are an ideal approach for chemodynamical modelling of galaxies. However, their computational costs are orders of magnitude higher than those of pure N -body simulations. Current simulations of MW-mass galaxies have a maximum mass resolution of $\sim 10^3 M_\odot$ (e.g. Hopkins et al. 2018; Grand et al. 2021). To achieve higher resolutions comparable to the *Gaia*/PFS data, technological breakthroughs in numerical simulations, possibly supported by deep learning technologies (Hirashima et al. 2023), are required.



Part II

APPENDICES

Fujii et al. (2019) performed a series of N -body simulations of MW-like galaxies. Here, we briefly describe the disc and bulge properties of their three best-fitting models, MWa5B, MWb6B and MWc7B. The parameters of their initial conditions are listed in Table A.1. The definitions of the parameters are described in Section 2.1.

Fujii et al. (2019) simulated the models for 10 Gyr and compared the disc and bulge properties at $t = 10$ Gyr in each of the models with those of the observations. The disc and bulge properties of MWa5B at $t = 10$ Gyr are shown in Fig. A.1. The top left panel show the disc surface density Σ as a function of the galactocentric radius R . The observed value in the solar neighbourhood (McKee et al. 2015; Bland-Hawthorn & Gerhard 2016) is also indicated by the grey shaded region. The top middle panel shows the radial velocity dispersion profile. The grey shaded region indicates the observed value for old thin disc stars in the solar neighbourhood (Bland-Hawthorn & Gerhard 2016). The top right panel shows the disc and DM density within $|z| < 1.1$ kpc, $K_z/2\pi G$ (Kuijken & Gilmore 1991) as a function of R . The orange dots with errors represent the observational measurements (Bovy & Rix 2013). The bottom left and bottom right panels show the line-of-sight velocity v_{los} and the line-of-sight velocity dispersion σ_{los} of the bulge region ($R < 3$ kpc), respectively. The blue solid, orange dashed and red dotted lines represent the values at $b = 4^\circ$, $b = 6^\circ$ and $b = 8^\circ$ as functions of l , respectively. Symbols with error bars represent the observational values from the Bulge Radial Velocity Assay (BRAVA) (Rich et al. 2007; McKee et al. 2015). Comparable plots for MWb6B and MWc7B are displayed in Fig. A.2 and Fig. A.3, respectively.

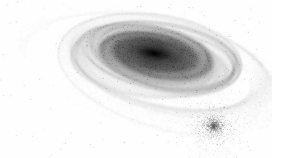
All of the models exhibit similar disc and bulge properties and are qualitatively consistent with the observations. Fujii et al. (2019) measured χ^2 for $\Sigma(R = 8 \text{ kpc})$, $\sigma_R(R = 8 \text{ kpc})$, $K_z(R = 8 \text{ kpc})$, v_{los} and σ_{los} of the bulge region to quantitatively evaluate how well the models reproduce the observations. They calculated the following value for each of the observables:

$$\chi_a^2 = \sum_{i=1}^{N_a} \left(\frac{a_{\text{sim},i} - a_{\text{obs},i}}{\sigma_{\text{obs},i}} \right)^2, \quad (\text{A.1})$$

where $a_{\text{sim},i}$ and $a_{\text{obs},i}$ are data points of the simulation and the observation, respectively, and $\sigma_{\text{obs},i}$ is the error of the observation. N_a is the number of data points. The values of χ^2 for each of the observables are listed in Table A.2. The total χ^2 of MWa5B is the smallest among the three models. Especially, its χ^2 for Σ , σ_R and K_z are smaller by a factor of 3–10 compared to the other models. On the other hand, the χ^2 for v_{los} and σ_{los} are comparable among the three models. In this study, we use MWa5B whose disc structure fits the observations the best because we mainly target the dynamics of the disc part.

Table A.1: Initial condition parameters for the MW models

	a_h	σ_h	ϵ_h	α_h	a_b	σ_b	ϵ_b	α_b	R_d	z_d	M_d	σ_{R0}
	[kpc]	[km s ⁻¹]			[kpc]	[km s ⁻¹]			[kpc]	[kpc]	[10 ¹⁰ M _⊙]	[km s ⁻¹]
MWa5B	10	420	0.85	0.8	0.75	330	0.99	0.5	2.3	0.2	3.61	94
MWb6B	10	380	0.83	0.8	0.78	273	0.99	0.5	2.6	0.2	4.1	90
MWc7B	12	400	0.80	0.8	1.0	280	0.97	0.5	2.6	0.2	4.1	90



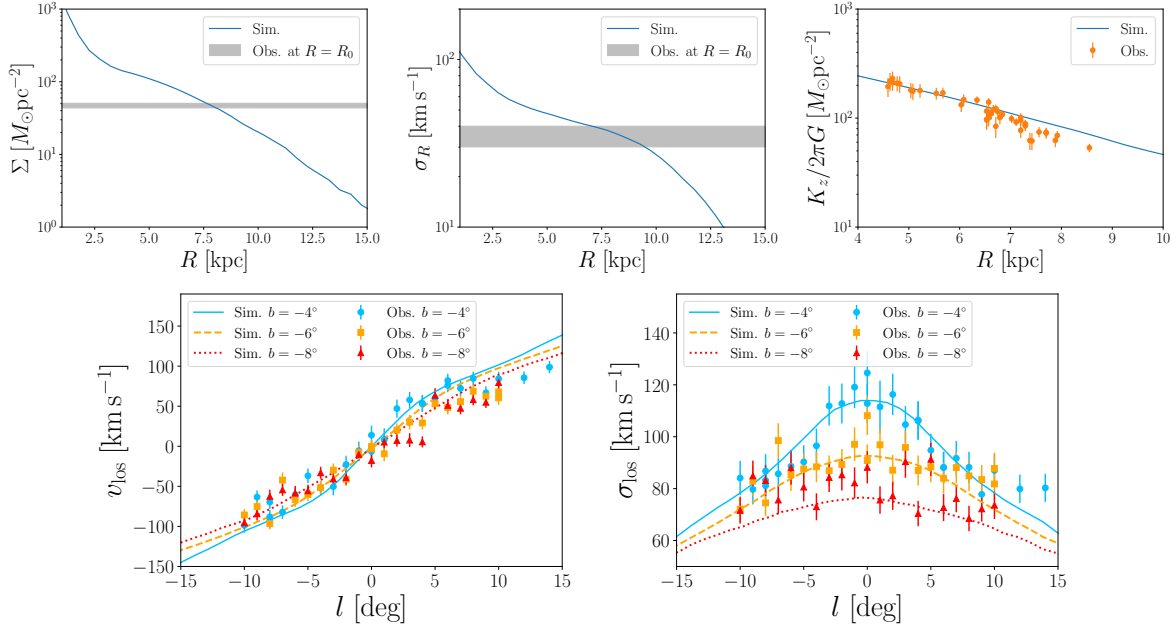


Figure A.1: Disc and bulge properties of MWa5B and comparison with observations. *Top left*: Disc surface density as a function of the galactocentric radius R . The grey shaded region indicates the observed value in the solar neighbourhood: $47.1 \pm 3.4 M_{\odot} \text{pc}^{-2}$ (McKee et al. 2015; Bland-Hawthorn & Gerhard 2016). *Top middle*: Radial velocity dispersion as a function of R . The grey shaded region indicates the observed value for old thin disc stars in the solar neighbourhood: $35 \pm 5 \text{km s}^{-1}$ (Bland-Hawthorn & Gerhard 2016). *Top right*: Disc and DM density within $|z| < 1.1$ kpc as a function of R . Orange dots with error bars represent the observational measurements (Bovy & Rix 2013). *Bottom left*: Line-of-sight velocity of the bulge region as a function of galactic longitude l . Blue solid, orange dashed and red dotted lines represent the values at $b = 4^\circ$, $b = 6^\circ$ and $b = 8^\circ$, respectively. Symbols with error bars represent the BRAVA data (Rich et al. 2007; McKee et al. 2015). *Bottom right*: Same as the bottom left panel but for the line-of-sight velocity dispersion.

Table A.2: χ^2 for Σ , σ_R , K_z , v_{los} and σ_{los}

	Σ	σ_R	K_z	v_{los}	σ_{los}	Total
MWa5B	0.4	0.1	0.2	2.3	1.6	4.5
MWb6B	1.5	1.5	1.0	2.8	1.2	8.1
MWc7B	2.0	3.0	0.6	2.1	1.3	9.0

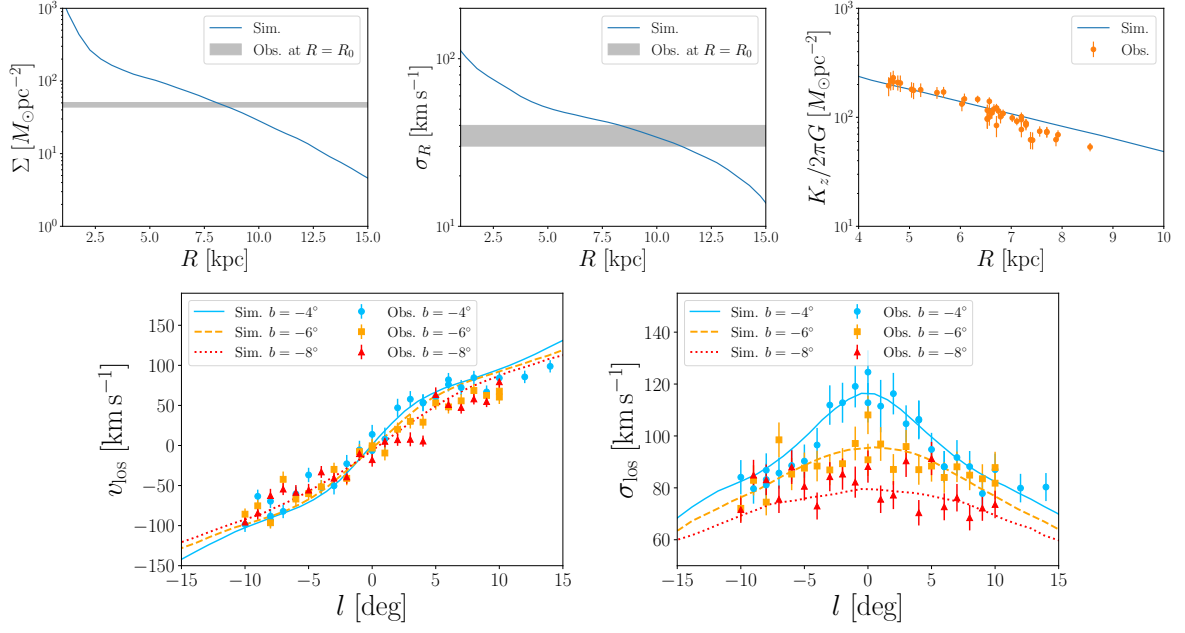


Figure A.2: Same as Fig. A.1 but for MWb6B.

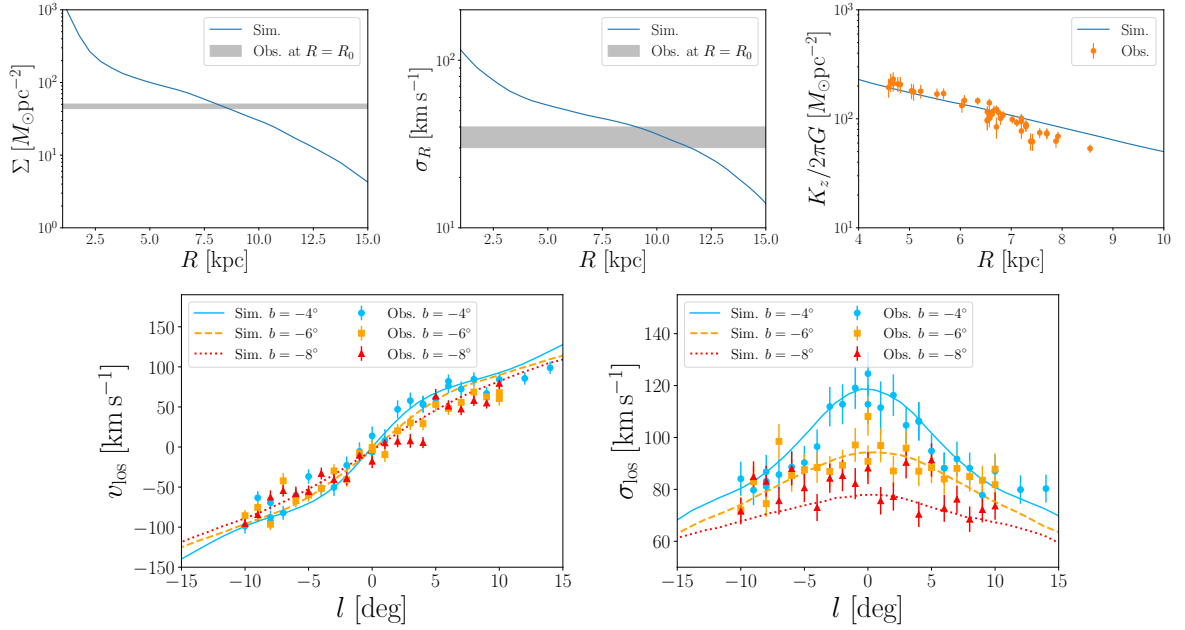


Figure A.3: Same as Fig. A.1 but for MWc7B.



SHAPES OF THE RESONANTLY TRAPPED ORBITS

In order to validate the frequency analysis described in Section 3.2.2, we visually checked the orbital shapes for 100 randomly selected particles in each of the resonances. These particles were selected by first statistically identifying the resonant bins (as presented in Fig. 3.4) and subsequently select 100 particles randomly from that particular resonant bin. Realistically one would expect some pollution of non-resonant orbits among the true resonance, but as we demonstrate the Fig. B.1 to Fig. B.4 where we show their orbits, it is clear that these resonant-bins are completely dominated by particles in the appropriate resonance. We therewith validate our analysis of using a Fourier selected sample for the analysis in this thesis.



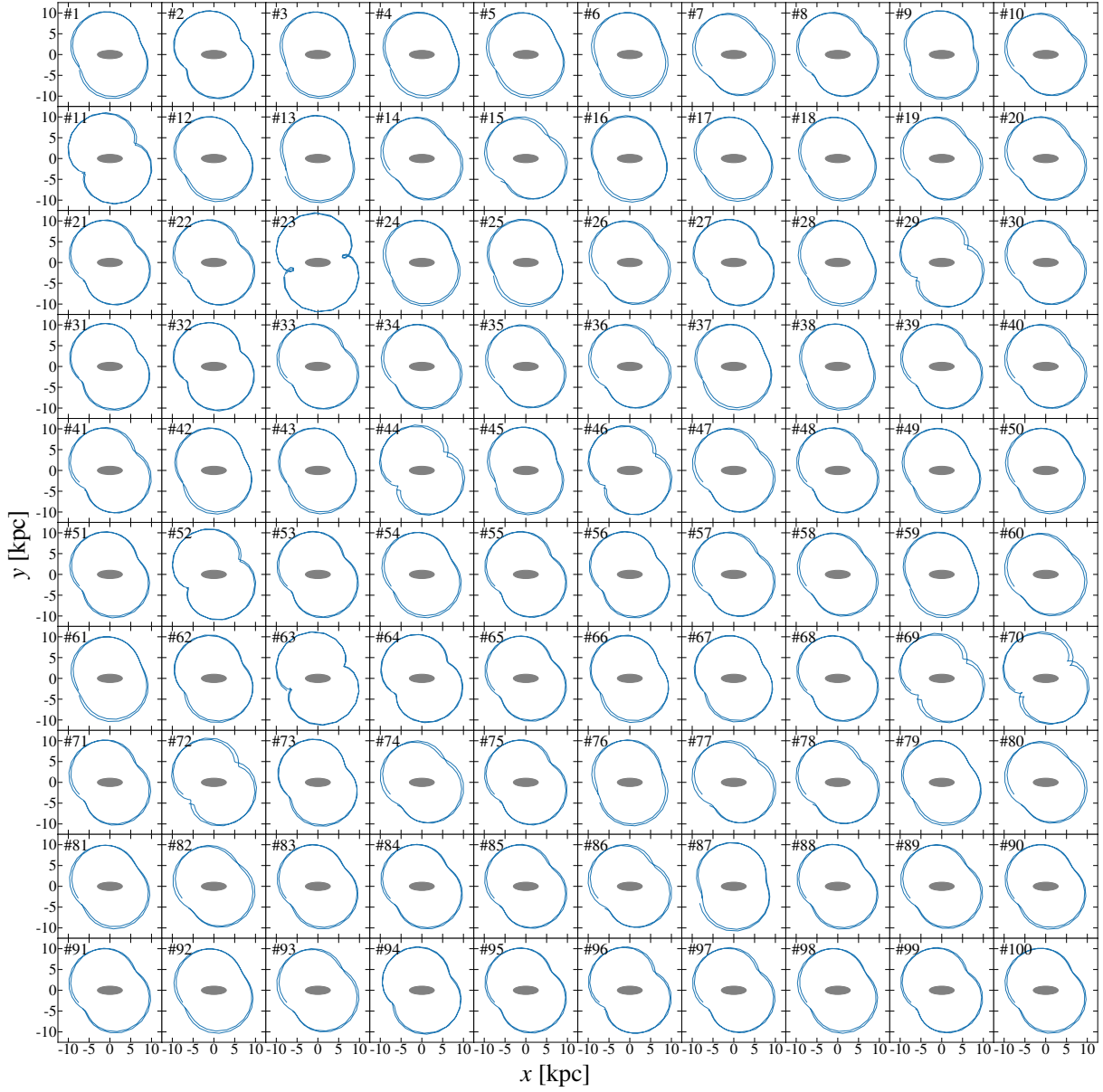


Figure B.1: Orbital shapes of the particles trapped in the 2:1 OLR.

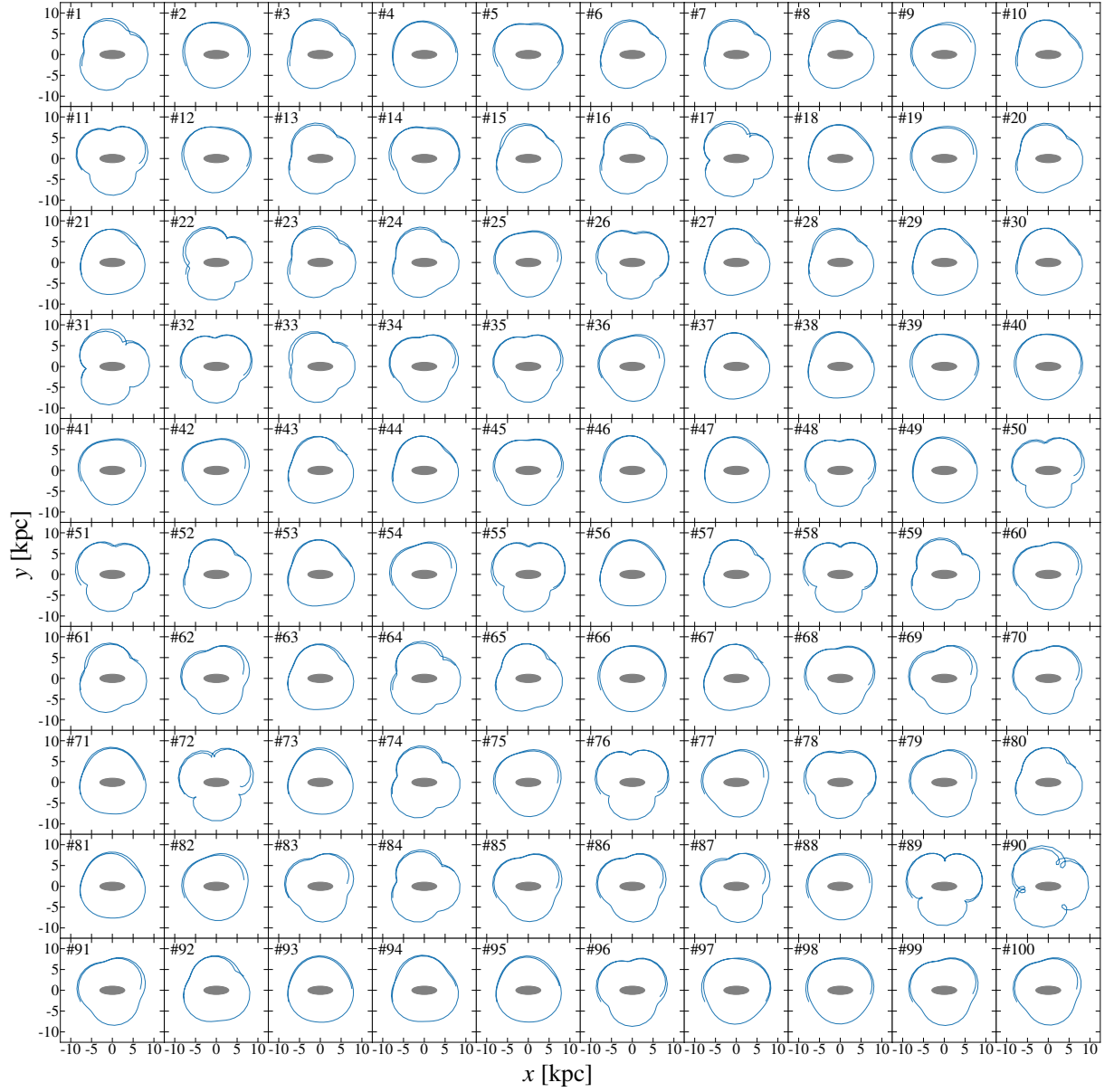
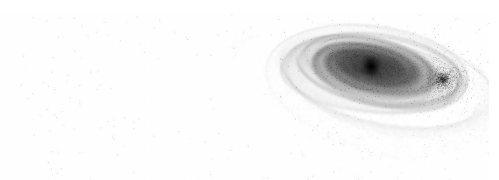


Figure B.2: Same as Fig. B.1 but for the 3:1 OLR.



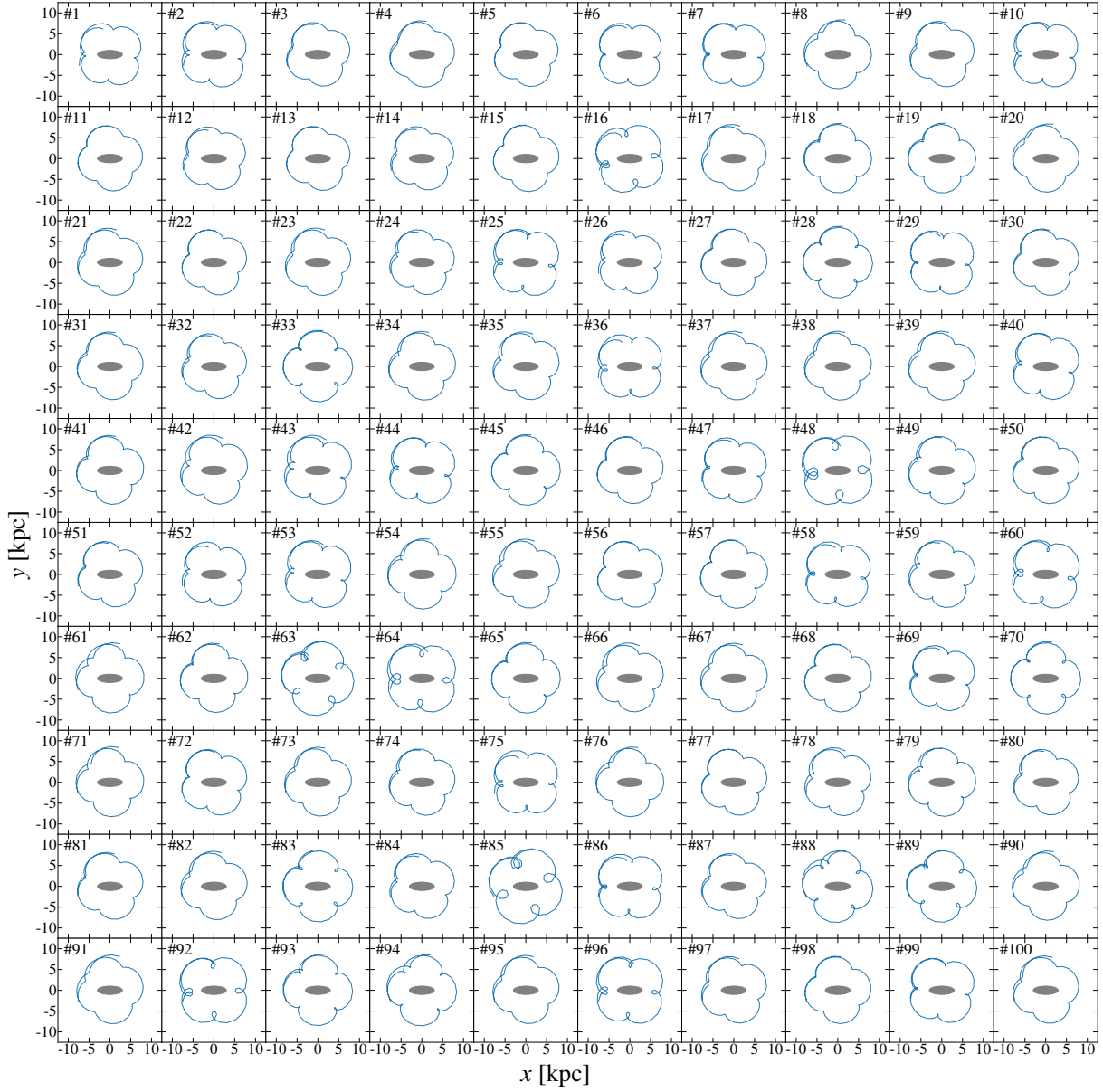


Figure B.3: Same as Fig. B.1 but for the 4:1 OLR.

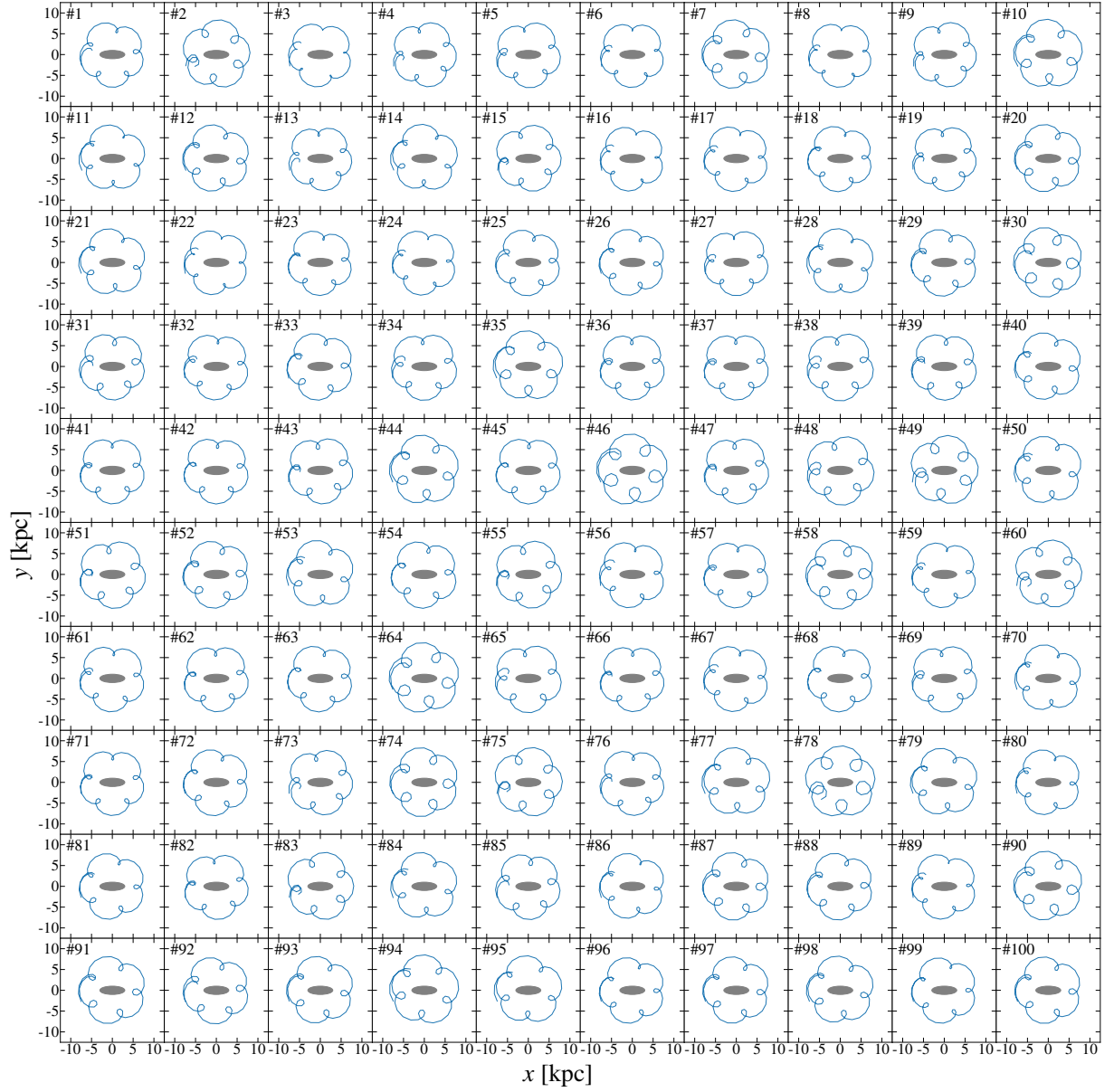
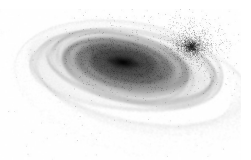


Figure B.4: Same as Fig. B.1 but for the 5:1 OLR.



LOCATION OF SPIRAL ARM

We describe two methods for determining the positions of the spiral arms in the disc of the simulated galaxy. The first method (Section C.1) is based on Fourier decomposition and is used to determine the global spiral pattern. The second method (Section C.2) is based on a peak-finding algorithm and is used to determine spiral positions in local snapshots. The former is used in Chapter 4 and the latter is used in Chapter 6.

C.1 AZIMUTHS OF SPIRAL ARMS

In N -body simulations of disc galaxies, spiral arms are not in steady states. Instead they undergo repeated formation and destruction (Baba et al. 2013), and determining their positions is not straightforward. Fourier decomposition of the disc surface density is used to determine their global pattern. In Fig. C.1, the phase angles $\phi_m(R)$ for $m = 2, 3$ and 4 are overplotted on the normalised density maps of the R - ϕ space. The overdense regions (i.e. spiral arms) show complex morphologies. None of the Fourier modes completely traces the overdensities. However, the $\phi_2(R)$ fits the high-density regions relatively well and hence we use that to define the spiral arms positions.

C.2 RADII OF SPIRAL ARMS

The arm and inter-arm radii in Chapter 6 are determined by the following method. We calculate the R distribution $n(R)$ for the particles in a narrow rectangle of $\{(x, y) \mid 4 < x < 16 \text{ kpc and } |y| < 1 \text{ kpc}\}$, where the Sun is located at $(x, y) = (8, 0) \text{ kpc}$. We smooth $n(R)$ with a Gaussian of 0.5 kpc width, and $\tilde{n}(R)$ represents it. Arm and inter-arm locations appear as peaks and dips in $(n - \tilde{n})/\tilde{n} = n/\tilde{n} - 1$, respectively. We apply a peak finding algorithm for $n/\tilde{n} - 1$ with `find_peaks` function implemented in `scipy` package (Virtanen et al. 2020). Fig. C.2 shows $n(R)$, $\tilde{n}(R)$, and $n(R)/\tilde{n}(R) - 1$ for the snapshots at $t = 2.5$ and 4.8 Gyr . Magenta and blue vertical lines respectively indicate the arm and inter-arm locations determined by the above method.



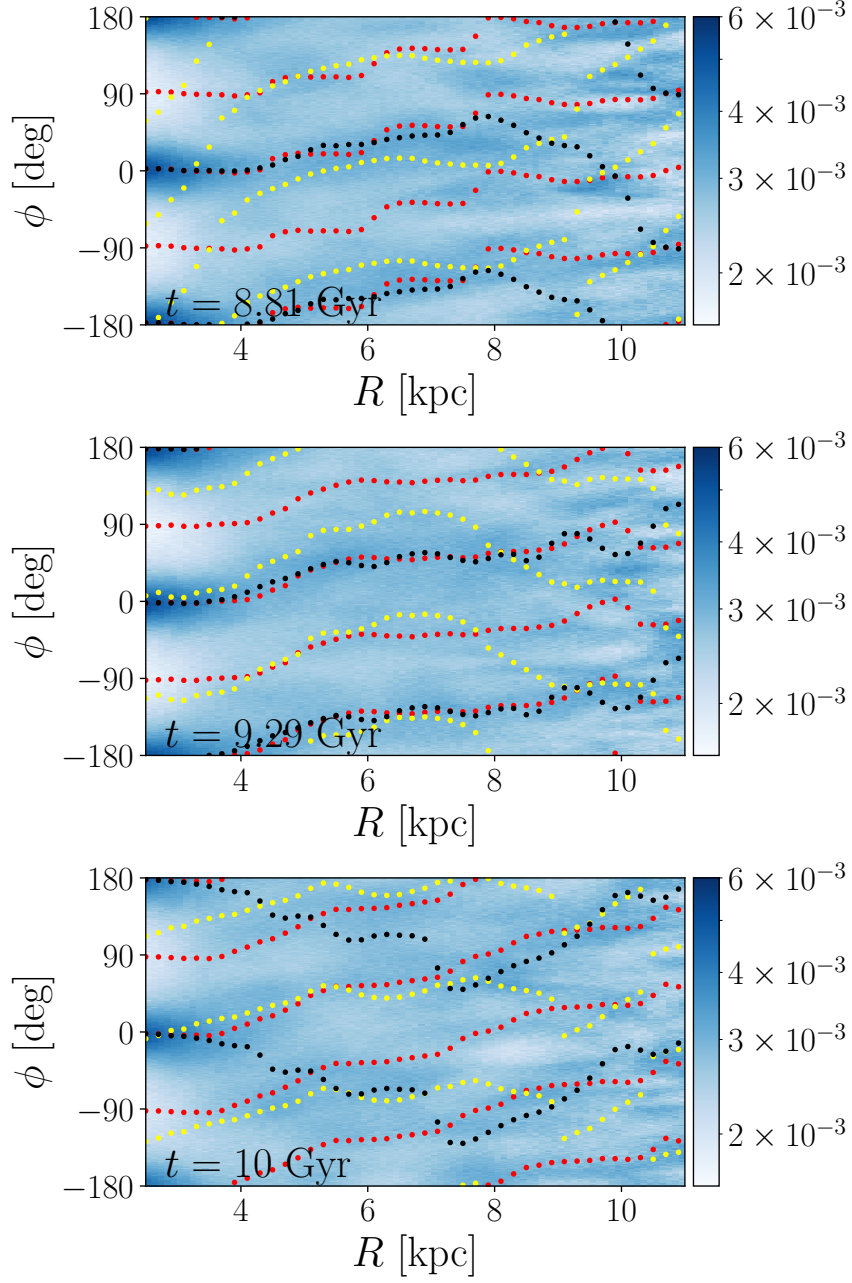


Figure C.1: The phase angles for the Fourier decomposition of the disc surface density, shown at $t = 8.81$, 9.29 , and 10 Gyr. Black, yellow, and red dots represent the phase angles for the $m = 2$, 3 , and 4 modes, respectively. The background colour represent the normalised surface densities, $\Sigma(R, \phi) / \Sigma_0(R)$.

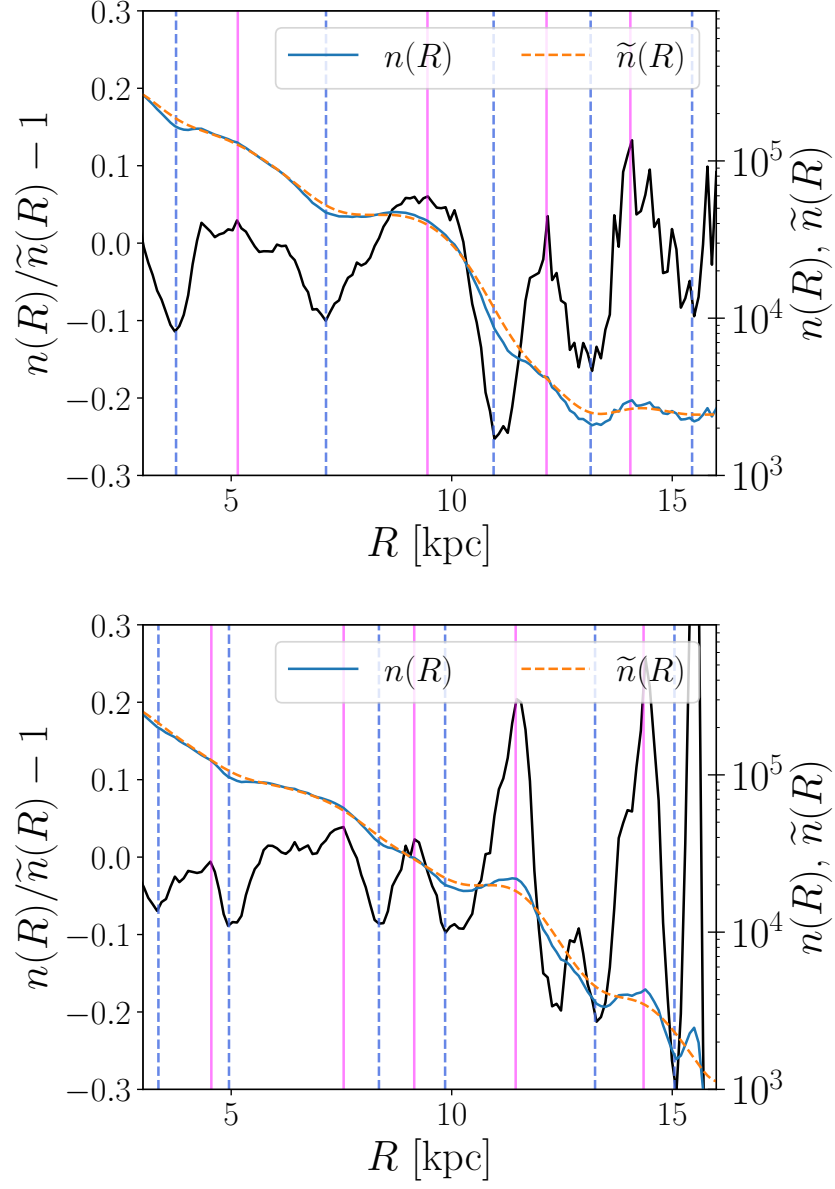
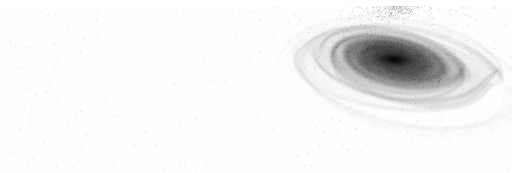


Figure C.2: Local stellar particle distributions in R at $t = 2.5$ (top) and 4.8 Gyr (bottom). Blue and orange lines show original and Gaussian-smoothed distributions, respectively. Magenta and blue vertical lines indicate the arm and inter-arm locations determined by the peak finding algorithm for $n/\tilde{n} - 1$ (black line).



SELECTION EFFECTS ON THE BREATHING MOTION

Fig. D.1 shows the selection function for the *Gaia* DR3 radial velocity sample (Cantat-Gaudin et al. 2023; Castro-Ginard et al. 2023) in the range $60^\circ \leq l \leq 75^\circ$, corresponding to the line-of-sight direction to the Local arm. We plot the completeness as a function of b for $G = 11, 13$ and 15 , with the $G - G_{RP}$ colour fixed at 1. We use `gaiaunlimited` Python package to make the plot. The completeness decreases towards the mid-plane at $|b| \lesssim 5^\circ$. The Galactic latitude of $|b| = 5^\circ$ corresponds to $|z| = 0.09, 0.17, 0.26$ and 0.35 kpc at the heliocentric distances $d = 1, 2, 3$ and 4 kpc, respectively. Fig. D.2 shows the face-on maps of the breathing velocity in the N -body model, as in the middle panel of Fig. 5.2, but here we use the particles only at $|z| > z_{\text{lim}}$ ($= 0.1, 0.2, 0.3$ and 0.4 kpc). The figure demonstrates how the selection bias affects the observed breathing velocity. As the limiting height z_{lim} increases, the amplitude of the breathing velocity increases. The selection effect can explain the trend that the amplitude of the breathing velocity in the region distant from the Sun is larger than that in the solar neighbourhood seen in Fig. 5.1.

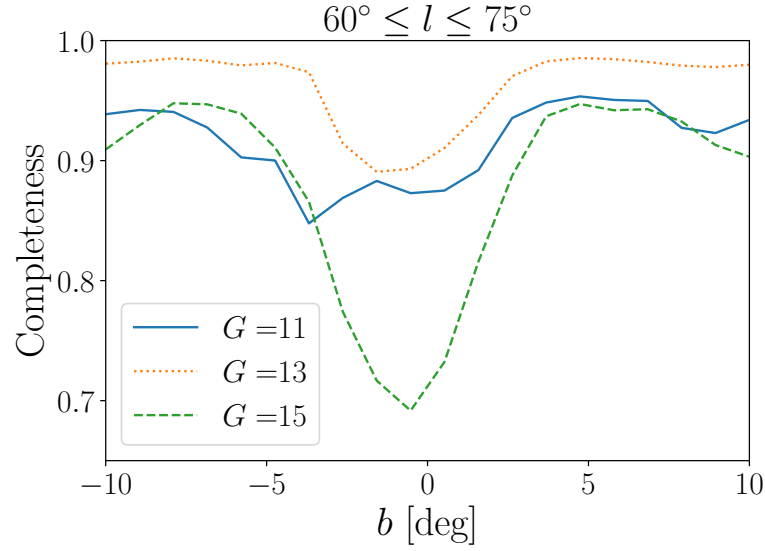


Figure D.1: Selection function for the *Gaia* DR3 radial velocity sample at $60^\circ \leq l \leq 75^\circ$.



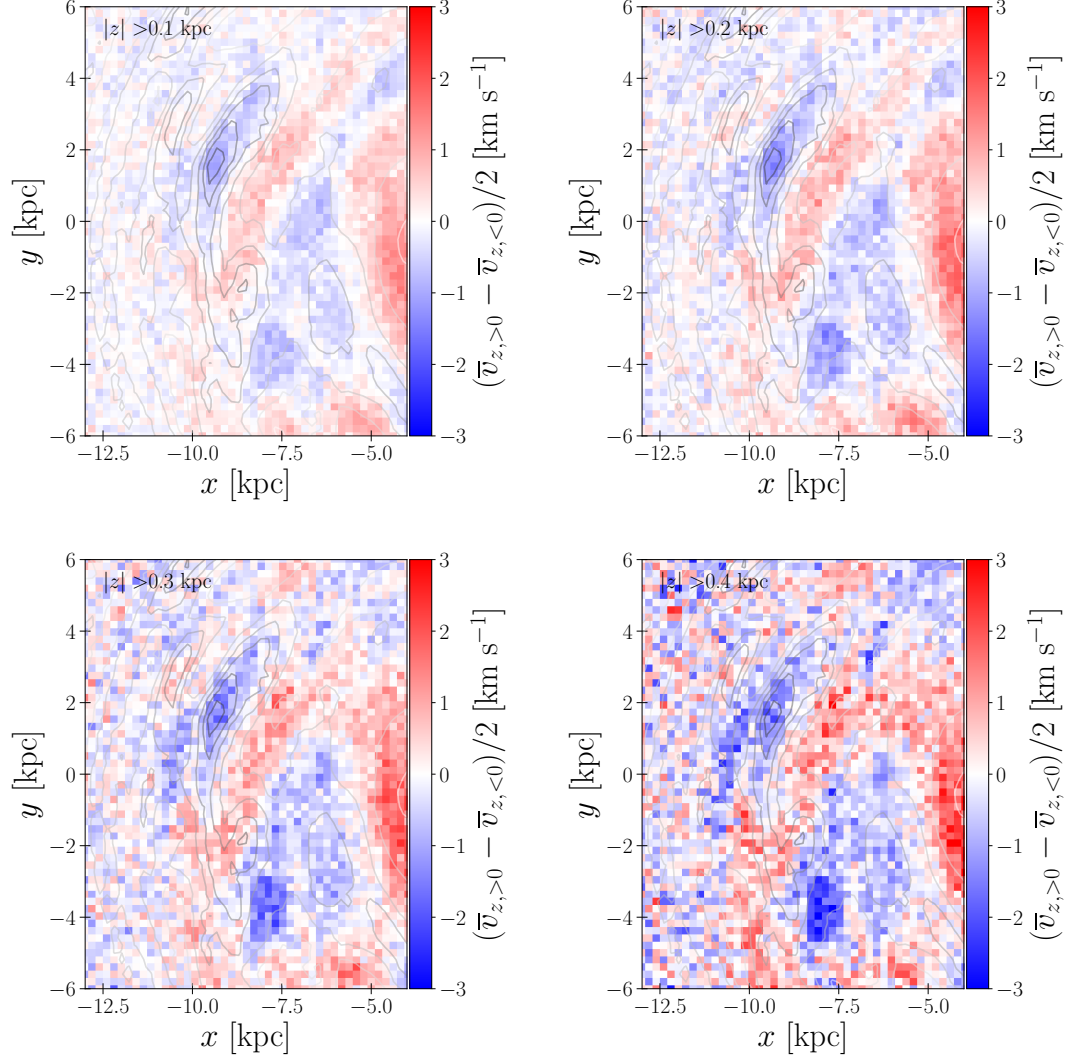


Figure D.2: Face-on maps of the breathing velocity for the particles at $|z| > 0.1$ (upper left), 0.2 (upper right), 0.3 (lower left) and 0.4 (lower right) kpc.

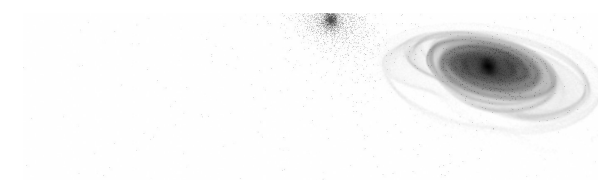
BIBLIOGRAPHY

- Aguerri J. A. L., Debattista V. P., Corsini E. M., 2003, *MNRAS*, **338**, 465
- Aguerri J. A. L., et al., 2015, *A&A*, **576**, A102
- Almannaei A. S., Kawata D., Baba J., Hunt J. A. S., Seabroke G., Yan Z., 2023, *arXiv e-prints*, p. [arXiv:2310.06831](#)
- Antoja T., et al., 2014, *A&A*, **563**, A60
- Antoja T., et al., 2018, *Nature*, **561**, 360
- Antoja T., Ramos P., García-Conde B., Bernet M., Laporte C. F. P., Katz D., 2023, *A&A*, **673**, A115
- Aoki S., Noguchi M., Iye M., 1979, *PASJ*, **31**, 737
- Ardèvol J., Monguió M., Figueras F., Romero-Gómez M., Carrasco J. M., 2023, *A&A*, **678**, A111
- Asano T., Fujii M. S., Baba J., Bédorf J., Sellentin E., Portegies Zwart S., 2020, *MNRAS*, **499**, 2416
- Asano T., Fujii M. S., Baba J., Bédorf J., Sellentin E., Portegies Zwart S., 2022, *MNRAS*, **514**, 460
- Asano T., Kawata D., Fujii M. S., Baba J., 2024, *MNRAS*, **529**, L7
- Astropy Collaboration et al., 2013, *A&A*, **558**, A33
- Astropy Collaboration et al., 2018, *AJ*, **156**, 123
- Astropy Collaboration et al., 2022, *ApJ*, **935**, 167
- Athanassoula E., 2002, *ApJ*, **569**, L83
- Athanassoula E., 2005, *MNRAS*, **358**, 1477
- Baba J., 2015, *MNRAS*, **454**, 2954
- Baba J., Asaki Y., Makino J., Miyoshi M., Saitoh T. R., Wada K., 2009, *ApJ*, **706**, 471
- Baba J., Saitoh T. R., Wada K., 2010, *PASJ*, **62**, 1413
- Baba J., Saitoh T. R., Wada K., 2013, *ApJ*, **763**, 46
- Baba J., Morokuma-Matsui K., Saitoh T. R., 2017, *MNRAS*, **464**, 246
- Baba J., Kawata D., Matsunaga N., Grand R. J. J., Hunt J. A. S., 2018, *ApJ*, **853**, L23
- Baba J., Kawata D., Schönrich R., 2022, *MNRAS*, **513**, 2850
- Banik U., Weinberg M. D., van den Bosch F. C., 2022, *ApJ*, **935**, 135
- Banik U., van den Bosch F. C., Weinberg M. D., 2023, *ApJ*, **952**, 65
- Barnes J., Hut P., 1986, *Nature*, **324**, 446
- Barros D. A., Pérez-Villegas A., Lépine J. R. D., Michtchenko T. A., Vieira R. S. S., 2020, *ApJ*, **888**, 75
- Bédorf J., Gaburov E., Portegies Zwart S., 2012, *Journal of Computational Physics*, **231**, 2825
- Bédorf J., Gaburov E., Fujii M. S., Nitadori K., Ishiyama T., Portegies Zwart S., 2014, in *Proceedings of the International Conference for High Performance Computing*. pp 54–65 ([arXiv:1412.0659](#)), [doi:10.1109/SC.2014.10](#)
- Benjamin R. A., et al., 2005, *ApJ*, **630**, L149
- Bennett M., Bovy J., 2019, *MNRAS*, **482**, 1417
- Bennett M., Bovy J., Hunt J. A. S., 2022, *ApJ*, **927**, 131
- Bernet M., Ramos P., Antoja T., Famaey B., Monari G., Al Kazwini H., Romero-Gómez M., 2022, *A&A*, **667**, A116
- Binney J., 2010, *MNRAS*, **401**, 2318
- Binney J., 2012, *MNRAS*, **426**, 1324
- Binney J., 2018, *MNRAS*, **474**, 2706
- Binney J., 2020, *MNRAS*, **495**, 895
- Binney J., McMillan P., 2011, *MNRAS*, **413**, 1889
- Binney J., Merrifield M., 1998, *Galactic Astronomy*
- Binney J., Schönrich R., 2018, *MNRAS*, **481**, 1501
- Binney J., Spergel D., 1982, *ApJ*, **252**, 308
- Binney J., Tremaine S., 2008, *Galactic Dynamics: Second Edition*
- Bissantz N., Gerhard O., 2002, *MNRAS*, **330**, 591
- Bland-Hawthorn J., Gerhard O., 2016, *ARA&A*, **54**, 529
- Bland-Hawthorn J., Tepper-García T., 2021, *MNRAS*, **504**, 3168
- Bland-Hawthorn J., et al., 2019, *MNRAS*, **486**, 1167
- Bovy J., 2015, *ApJS*, **216**, 29



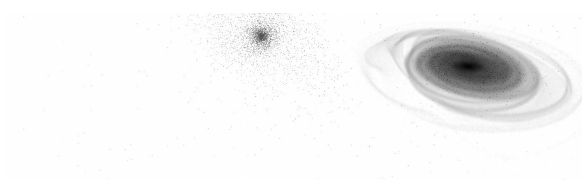
- Bovy J., 2017, *MNRAS*, **468**, L63
- Bovy J., Rix H.-W., 2013, *ApJ*, **779**, 115
- Bovy J., Leung H. W., Hunt J. A. S., Mackereth J. T., García-Hernández D. A., Roman-Lopes A., 2019, *MNRAS*, **490**, 4740
- Bureau M., Freeman K. C., 1999, *AJ*, **118**, 126
- Cantat-Gaudin T., et al., 2023, *A&A*, **669**, A55
- Cao L., Mao S., Nataf D., Rattenbury N. J., Gould A., 2013, *MNRAS*, **434**, 595
- Carr C., Johnston K. V., Laporte C. F. P., Ness M. K., 2022, *MNRAS*, **516**, 5067
- Carrillo I., et al., 2019, *MNRAS*, **490**, 797
- Castro-Ginard A., et al., 2023, *A&A*, **677**, A37
- Ceverino D., Klypin A., 2007, *MNRAS*, **379**, 1155
- Chiba R., 2023, *MNRAS*, **525**, 3576
- Chiba R., Kataria S. K., 2023, *arXiv e-prints*, p. arXiv:2311.07640
- Chiba R., Schönrich R., 2021, *MNRAS*, **505**, 2412
- Chiba R., Schönrich R., 2022, *MNRAS*, **513**, 768
- Chiba R., Friske J. K. S., Schönrich R., 2021, *MNRAS*, **500**, 4710
- Christiansen W. N., Hindman J. V., 1951, *Nature*, **167**, 635
- Churchwell E., et al., 2009, *PASP*, **121**, 213
- Clarke J. P., Wegg C., Gerhard O., Smith L. C., Lucas P. W., Wylie S. M., 2019, *MNRAS*, **489**, 3519
- Combes F., Sanders R. H., 1981, *A&A*, **96**, 164
- Combes F., Debbasch F., Friedli D., Pfenniger D., 1990, *A&A*, **233**, 82
- D’Onghia E., L. Aguerri J. A., 2020, *ApJ*, **890**, 117
- D’Onghia E., Vogelsberger M., Hernquist L., 2013, *ApJ*, **766**, 34
- Dambis A. K., et al., 2015, *Astronomy Letters*, **41**, 489
- De Simone R., Wu X., Tremaine S., 2004, *MNRAS*, **350**, 627
- Debattista V. P., 2014, *MNRAS*, **443**, L1
- Debattista V. P., Ness M., Gonzalez O. A., Freeman K., Zoccali M., Minniti D., 2017, *MNRAS*, **469**, 1587
- Debattista V. P., Liddicott D. J., Khachatryan T., Beraldo e Silva L., 2020, *MNRAS*, **498**, 3334
- Dehnen W., 1998, *AJ*, **115**, 2384
- Dehnen W., 1999a, *AJ*, **118**, 1201
- Dehnen W., 1999b, *ApJ*, **524**, L35
- Dehnen W., 2000, *AJ*, **119**, 800
- Drimmel R., 2000, *A&A*, **358**, L13
- ESA ed. 1997, The HIPPARCOS and TYCHO catalogues ESA Special Publication Vol. 1200
- Eggen O. J., 1958a, *MNRAS*, **118**, 65
- Eggen O. J., 1958b, *MNRAS*, **118**, 154
- Eggen O. J., 1971, *PASP*, **83**, 762
- Eggen O. J., 1978, *ApJ*, **222**, 203
- Eilers A.-C., Hogg D. W., Rix H.-W., Ness M. K., 2019, *ApJ*, **871**, 120
- Eilers A.-C., Hogg D. W., Rix H.-W., Frankel N., Hunt J. A. S., Fouvy J.-B., Buck T., 2020, *ApJ*, **900**, 186
- Elsen E., Vishal V., Houston M., Pande V., Hanrahan P., Darve E., 2007, *arXiv e-prints*, p. arXiv:0706.3060
- Englmaier P., Gerhard O., 1999, *MNRAS*, **304**, 512
- Ewen H. I., Purcell E. M., 1951, *Nature*, **168**, 356
- Fabrizius C., et al., 2021, *A&A*, **649**, A5
- Famaey B., Jorissen A., Luri X., Mayor M., Udry S., Dejonghe H., Turon C., 2005, *A&A*, **430**, 165
- Famaey B., Pourbaix D., Frankowski A., van Eck S., Mayor M., Udry S., Jorissen A., 2009, *A&A*, **498**, 627
- Faure C., Siebert A., Famaey B., 2014, *MNRAS*, **440**, 2564
- Fragkoudi F., et al., 2019, *MNRAS*, **488**, 3324
- Friedli D., Pfenniger D., 1990, in European Southern Observatory Conference and Workshop Proceedings. p. 265
- Fujii M. S., Baba J., Saitoh T. R., Makino J., Kokubo E., Wada K., 2011, *ApJ*, **730**, 109
- Fujii M. S., Bédorf J., Baba J., Portegies Zwart S., 2018, *MNRAS*, **477**, 1451
- Fujii M. S., Bédorf J., Baba J., Portegies Zwart S., 2019, *MNRAS*, **482**, 1983
- Fukushima T., et al., 2019, *PASJ*, **71**, 72
- Funakoshi N., Matsunaga N., Kawata D., Baba J., Taniguchi D., Fujii M., 2024, *arXiv e-prints*, p. arXiv:2401.13037

- Fux R., 1999, *A&A*, **345**, 787
- Fux R., 2001, *A&A*, **373**, 511
- GRAVITY Collaboration et al., 2022, *A&A*, **657**, L12
- Gaia Collaboration et al., 2016a, *A&A*, **595**, A1
- Gaia Collaboration et al., 2016b, *A&A*, **595**, A2
- Gaia Collaboration et al., 2018a, *A&A*, **616**, A1
- Gaia Collaboration et al., 2018b, *A&A*, **616**, A11
- Gaia Collaboration et al., 2021, *A&A*, **649**, A1
- Gaia Collaboration et al., 2023a, *A&A*, **674**, A1
- Gaia Collaboration et al., 2023b, *A&A*, **674**, A37
- García-Conde B., Antoja T., Roca-Fàbrega S., Gómez F., Ramos P., Garavito-Camargo N., Gómez-Flechoso M., 2023, *arXiv e-prints*, p. [arXiv:2311.07137](https://arxiv.org/abs/2311.07137)
- Georgelin Y. M., Georgelin Y. P., 1976, *A&A*, **49**, 57
- Ghosh S., Debattista V. P., Khachaturyants T., 2022, *MNRAS*, **511**, 784
- Gontcharov G. A., 2006, *Astronomy Letters*, **32**, 759
- Gouda N., 2011, *Scholarpedia*, **6**, 12021
- Gouda N., 2012, in Aoki W., Ishigaki M., Suda T., Tsujimoto T., Arimoto N., eds, *Astronomical Society of the Pacific Conference Series Vol. 458, Galactic Archaeology: Near-Field Cosmology and the Formation of the Milky Way*. p. 417
- Gouda N., 2018, in Recio-Blanco A., de Laverny P., Brown A. G. A., Prusti T., eds, *Proceedings of the International Astronomical Union Vol. 330, Astrometry and Astrophysics in the Gaia Sky*. pp 90–91, [doi:10.1017/S1743921317005270](https://doi.org/10.1017/S1743921317005270)
- Gouda N., Jasmine Team 2020, in Valluri M., Sellwood J. A., eds, *Proceedings of the International Astronomical Union Vol. 353, Galactic Dynamics in the Era of Large Surveys*. pp 51–53, [doi:10.1017/S1743921319007968](https://doi.org/10.1017/S1743921319007968)
- Grand R. J. J., Kawata D., Cropper M., 2012a, *MNRAS*, **421**, 1529
- Grand R. J. J., Kawata D., Cropper M., 2012b, *MNRAS*, **426**, 167
- Grand R. J. J., et al., 2021, *MNRAS*, **507**, 4953
- Grand R. J. J., Pakmor R., Fragkoudi F., Gómez F. A., Trick W., Simpson C. M., van de Voort F., Bieri R., 2023, *MNRAS*, **524**, 801
- Halle A., Di Matteo P., Haywood M., Combes F., 2018, *A&A*, **616**, A86
- Hamada T., Iitaka T., 2007, *arXiv e-prints*, pp [astro-ph/0703100](https://arxiv.org/abs/astro-ph/0703100)
- Hamilton C., Tolman E. A., Arzamasskiy L., Duarte V. N., 2023, *ApJ*, **954**, 12
- Hammersley P. L., Garzón F., Mahoney T. J., López-Corredoira M., Torres M. A. P., 2000, *MNRAS*, **317**, L45
- Hattori K., Gouda N., Tagawa H., Sakai N., Yano T., Baba J., Kumamoto J., 2019, *MNRAS*, **484**, 4540
- Hernquist L., 1990, *ApJ*, **356**, 359
- Herschel W., 1785, *Philosophical Transactions of the Royal Society of London Series I*, **75**, 213
- Hilmi T., et al., 2020, *MNRAS*, **497**, 933
- Hirashima K., Moriwaki K., Fujii M. S., Hirai Y., Saitoh T. R., Makino J., 2023, *MNRAS*, **526**, 4054
- Hobbs D., Høg E., 2018, in Recio-Blanco A., de Laverny P., Brown A. G. A., Prusti T., eds, *Proceedings of the International Astronomical Union Vol. 330, Astrometry and Astrophysics in the Gaia Sky*. pp 67–70, [doi:10.1017/S1743921317005348](https://doi.org/10.1017/S1743921317005348)
- Hobbs D., et al., 2016, *arXiv e-prints*, p. [arXiv:1609.07325](https://arxiv.org/abs/1609.07325)
- Hoeg E., et al., 1997, *A&A*, **323**, L57
- Hoeg E., et al., 2000, *A&A*, **355**, L27
- Hopkins P. F., et al., 2018, *MNRAS*, **480**, 800
- Hou L. G., Han J. L., 2014, *A&A*, **569**, A125
- Hunt J. A. S., Bovy J., 2018, *MNRAS*, **477**, 3945
- Hunt J. A. S., Hong J., Bovy J., Kawata D., Grand R. J. J., 2018, *MNRAS*, **481**, 3794
- Hunt J. A. S., Bub M. W., Bovy J., Mackereth J. T., Trick W. H., Kawata D., 2019, *MNRAS*, **490**, 1026
- Hunt J. A. S., Stelea I. A., Johnston K. V., Gandhi S. S., Laporte C. F. P., Bédorf J., 2021, *MNRAS*, **508**, 1459
- Hunt J. A. S., Price-Whelan A. M., Johnston K. V., Darragh-Ford E., 2022, *MNRAS*, **516**, L7
- Ibata R. A., Gilmore G., Irwin M. J., 1994, *Nature*, **370**, 194
- Iye M., 1978, *PASJ*, **30**, 223
- Iye M., 1985, in van Woerden H., Allen R. J., Burton W. B., eds, *IAU Symposium Vol. 106, The Milky Way Galaxy*. p. 535



- Jönsson H., et al., 2020, *AJ*, **160**, 120
- Kaasalainen M., Binney J., 1994, *MNRAS*, **268**, 1033
- Kalnajs A. J., 1991, in Sundelius B., ed., *Dynamics of Disc Galaxies*. p. 323
- Kapteyn J. C., 1922, *ApJ*, **55**, 302
- Kawata D., Baba J., Ciucă I., Cropper M., Grand R. J. J., Hunt J. A. S., Seabroke G., 2018, *MNRAS*, **479**, L108
- Kawata D., Baba J., Hunt J. A. S., Schönrich R., Ciucă I., Friske J., Seabroke G., Cropper M., 2021, *MNRAS*, **508**, 728
- Kawata D., et al., 2023, *arXiv e-prints*, p. [arXiv:2307.05666](https://arxiv.org/abs/2307.05666)
- Khachatryan T., Debattista V. P., Ghosh S., Beraldo e Silva L., Daniel K. J., 2022, *MNRAS*, **517**, L55
- Khanna S., et al., 2019, *MNRAS*, **489**, 4962
- Khoperskov S., Gerhard O., 2022, *A&A*, **663**, A38
- Khoperskov S., Di Matteo P., Gerhard O., Katz D., Haywood M., Combes F., Berczik P., Gomez A., 2019, *A&A*, **622**, L6
- Khoperskov S., Gerhard O., Di Matteo P., Haywood M., Katz D., Khrapov S., Khoperskov A., Arnaboldi M., 2020, *A&A*, **634**, L8
- van der Kruit P. C., 2019, *Jan Hendrik Oort: Master of the Galactic System*. Springer, [doi:10.1007/978-3-030-17801-7](https://doi.org/10.1007/978-3-030-17801-7)
- Kuijken K., Dubinski J., 1995, *MNRAS*, **277**, 1341
- Kuijken K., Gilmore G., 1991, *ApJ*, **367**, L9
- Kullback S., Leibler R. A., 1951, *The annals of mathematical statistics*, **22**, 79
- Kumar A., Ghosh S., Kataria S. K., Das M., Debattista V. P., 2022, *MNRAS*, **516**, 1114
- Kushniruk I., Bensby T., Feltzing S., Sahlholdt C. L., Feuillet D., Casagrande L., 2020, *A&A*, **638**, A154
- Landau L., 1946, *Zhurnal eksperimentalnoi i teoreticheskoi fiziki*, **16**, 574
- Laporte C. F. P., Minchev I., Johnston K. V., Gómez F. A., 2019, *MNRAS*, **485**, 3134
- Latham D. W., Stefanik R. P., Torres G., Davis R. J., Mazeh T., Carney B. W., Laird J. B., Morse J. A., 2002, *AJ*, **124**, 1144
- Leavitt H. S., Pickering E. C., 1912, *Harvard College Observatory Circular*, **173**, 1
- van Leeuwen F., 2007, *A&A*, **474**, 653
- Li Z.-Y., Shen J., 2012, *ApJ*, **757**, L7
- Li Z.-Y., Shen J., 2020, *ApJ*, **890**, 85
- Li Z., Gerhard O., Shen J., Portail M., Wegg C., 2016, *ApJ*, **824**, 13
- Li C., Siebert A., Monari G., Famaey B., Rozier S., 2023a, *MNRAS*, **524**, 6331
- Li X., Shlosman I., Heller C., Pfenniger D., 2023b, *MNRAS*, **526**, 1972
- Lindblad B., 1927, *MNRAS*, **87**, 553
- Lindgren L., et al., 2021, *A&A*, **649**, A4
- López-Corredoira M., Garzón F., Wang H. F., Sylos Labini F., Nagy R., Chrobáková Ž., Chang J., Villarroel B., 2020, *A&A*, **634**, A66
- Lumsden S. L., Hoare M. G., Urquhart J. S., Oudmaijer R. D., Davies B., Mottram J. C., Cooper H. D. B., Moore T. J. T., 2013, *ApJS*, **208**, 11
- Makino J., Taiji M., 1998, *Scientific Simulations with Special-Purpose Computers—the GRAPE Systems*
- Martinez-Medina L., Pérez-Villegas A., Peimbert A., 2022, *MNRAS*, **512**, 1574
- McKee C. F., Parravano A., Hollenbach D. J., 2015, *ApJ*, **814**, 13
- McMillan P. J., 2017, *MNRAS*, **465**, 76
- McMillan P. J., Binney J. J., 2008, *MNRAS*, **390**, 429
- Merritt D., Sellwood J. A., 1994, *ApJ*, **425**, 551
- Michtchenko T. A., Lépine J. R. D., Barros D. A., Vieira R. S. S., 2018a, *A&A*, **615**, A10
- Michtchenko T. A., Lépine J. R. D., Pérez-Villegas A., Vieira R. S. S., Barros D. A., 2018b, *ApJ*, **863**, L37
- Miki Y., Umemura M., 2017, *New Astron.*, **52**, 65
- Minchev I., Nordhaus J., Quillen A. C., 2007, *ApJ*, **664**, L31
- Minchev I., Boily C., Siebert A., Bienayme O., 2010, *MNRAS*, **407**, 2122
- Miyachi Y., Sakai N., Kawata D., Baba J., Honma M., Matsunaga N., Fujisawa K., 2019, *ApJ*, **882**, 48
- Monari G., Famaey B., Siebert A., 2015, *MNRAS*, **452**, 747
- Monari G., Famaey B., Siebert A., 2016a, *MNRAS*, **457**, 2569
- Monari G., Famaey B., Siebert A., Grand R. J. J., Kawata D., Boily C., 2016b, *MNRAS*, **461**, 3835
- Monari G., Famaey B., Siebert A., Duchateau A., Lorscheider T., Bienaymé O., 2017a, *MNRAS*, **465**, 1443

- Monari G., Kawata D., Hunt J. A. S., Famaey B., 2017b, *MNRAS*, **466**, L113
- Monari G., Famaey B., Fouvy J.-B., Binney J., 2017c, *MNRAS*, **471**, 4314
- Monari G., Famaey B., Siebert A., Wegg C., Gerhard O., 2019a, *A&A*, **626**, A41
- Monari G., Famaey B., Siebert A., Bienaymé O., Ibata R., Wegg C., Gerhard O., 2019b, *A&A*, **632**, A107
- Moreno E., Fernández-Trincado J. G., Schuster W. J., Pérez-Villegas A., Chaves-Velasquez L., 2021, *MNRAS*, **506**, 4687
- Morgan W. W., Keenan P. C., Kellman E., 1943, An atlas of stellar spectra, with an outline of spectral classification
- Morgan W. W., Sharpless S., Osterbrock D., 1952, *AJ*, **57**, 3
- Morgan W. W., Whitford A. E., Code A. D., 1953, *ApJ*, **118**, 318
- Muller C. A., Oort J. H., 1951, *Nature*, **168**, 357
- Nakanishi H., Sofue Y., 2016, *PASJ*, **68**, 5
- Nakasato N., 2012, *Journal of Computational Science*, **3**, 132
- Navarro J. F., Frenk C. S., White S. D. M., 1997, *ApJ*, **490**, 493
- Okamoto T., Isoe M., Habe A., 2015, *PASJ*, **67**, 63
- Okuda H., Maihara T., Oda N., Sugiyama T., 1977, *Nature*, **265**, 515
- Oort J. H., 1927, *Bull. Astron. Inst. Netherlands*, **3**, 275
- Oort J. H., 1928, *Bull. Astron. Inst. Netherlands*, **4**, 269
- Oort J. H., 1932, *Bull. Astron. Inst. Netherlands*, **6**, 249
- Oort J. H., Kerr F. J., Westerhout G., 1958, *MNRAS*, **118**, 379
- Palicio P. A., Recio-Blanco A., Poggio E., Antoja T., McMillan P. J., Spitoni E., 2023, *A&A*, **670**, L7
- Pérez-Villegas A., Portail M., Wegg C., Gerhard O., 2017, *ApJ*, **840**, L2
- Perryman M., 2023, *Contemporary Physics*, **64**, 65
- Perryman M. A. C., et al., 1997, *A&A*, **323**, L49
- Pfenniger D., 1990, *A&A*, **230**, 55
- Poggio E., et al., 2021, *A&A*, **651**, A104
- Portail M., Gerhard O., Wegg C., Ness M., 2017, *MNRAS*, **465**, 1621
- Portegies Zwart S. F., Belleman R. G., Geldof P. M., 2007, *New Astron.*, **12**, 641
- Quillen A. C., 2002, *AJ*, **124**, 722
- Quillen A. C., Minchev I., 2005, *AJ*, **130**, 576
- Quillen A. C., Minchev I., Sharma S., Qin Y.-J., Di Matteo P., 2014, *MNRAS*, **437**, 1284
- Quillen A. C., et al., 2018, *MNRAS*, **478**, 228
- Raha N., Sellwood J. A., James R. A., Kahn F. D., 1991, *Nature*, **352**, 411
- Ramos P., Antoja T., Figueras F., 2018, *A&A*, **619**, A72
- Rattenbury N. J., Mao S., Sumi T., Smith M. C., 2007, *MNRAS*, **378**, 1064
- Reid M. J., Brunthaler A., 2020, *ApJ*, **892**, 39
- Reid M. J., et al., 2014, *ApJ*, **783**, 130
- Reid M. J., et al., 2019, *ApJ*, **885**, 131
- Rich R. M., Reitzel D. B., Howard C. D., Zhao H., 2007, *ApJ*, **658**, L29
- Ruiz-Lara T., Gallart C., Bernard E. J., Cassisi S., 2020, *Nature Astronomy*, **4**, 965
- Sanders J. L., Smith L., Evans N. W., 2019, *MNRAS*, **488**, 4552
- Schönrich R., Binney J., 2012, *MNRAS*, **419**, 1546
- Schönrich R., Binney J., Dehnen W., 2010, *MNRAS*, **403**, 1829
- Scott D. W., 2015, *Multivariate density estimation: theory, practice, and visualization*. John Wiley & Sons
- Sellwood J. A., Carlberg R. G., 1984, *ApJ*, **282**, 61
- Sellwood J. A., Gerhard O., 2020, *MNRAS*, **495**, 3175
- Sellwood J. A., Sparke L. S., 1988, *MNRAS*, **231**, 25P
- Shapley H., 1918a, *PASP*, **30**, 42
- Shapley H., 1918b, *ApJ*, **48**, 154
- Shen J., Zheng X.-W., 2020, *Research in Astronomy and Astrophysics*, **20**, 159
- Shen J., Rich R. M., Kormendy J., Howard C. D., De Propris R., Kunder A., 2010, *ApJ*, **720**, L72
- Skowron D. M., et al., 2019, *Science*, **365**, 478
- Skrutskie M. F., et al., 2006, *AJ*, **131**, 1163
- Sofue Y., 2017a, *Galactic Radio Astronomy*, doi:10.1007/978-981-10-3445-9.
- Sofue Y., 2017b, *PASJ*, **69**, R1
- Sofue Y., Honma M., Omodaka T., 2009, *PASJ*, **61**, 227



- Sofue Y., Arimoto N., Iye M., eds, 2018, 祖父江 義明, 有本 信雄, 家 正則 [編] 銀河II 銀河系 [第2版] (シリーズ現代の天文学 第5巻) . 日本評論社
- Sormani M. C., Binney J., Magorrian J., 2015, *MNRAS*, **454**, 1818
- Sugimoto D., Chikada Y., Makino J., Ito T., Ebisuzaki T., Umemura M., 1990, *Nature*, **345**, 33
- Takada M., et al., 2014, *PASJ*, **66**, R1
- Tepper-García T., Bland-Hawthorn J., Freeman K., 2022, *MNRAS*, **515**, 5951
- Tremaine S., 1999, *MNRAS*, **307**, 877
- Tremaine S., Frankel N., Bovy J., 2023, *MNRAS*, **521**, 114
- Trick W. H., 2022, *MNRAS*, **509**, 844
- Trick W. H., Coronado J., Rix H.-W., 2019, *MNRAS*, **484**, 3291
- Tsukui T., Iguchi S., 2021, *Science*, **372**, 1201
- Urquhart J. S., Figura C. C., Moore T. J. T., Hoare M. G., Lumsden S. L., Mottram J. C., Thompson M. A., Oudmaijer R. D., 2014, *MNRAS*, **437**, 1791
- VERA Collaboration et al., 2020, *PASJ*, **72**, 50
- Vallée J. P., 2017, *The Astronomical Review*, **13**, 113
- Vasiliev E., 2019, *MNRAS*, **482**, 1525
- Vasiliev E., Belokurov V., 2020, *MNRAS*, **497**, 4162
- Virtanen P., et al., 2020, *Nature Methods*, **17**, 261
- Wada K., Baba J., Saitoh T. R., 2011, *ApJ*, **735**, 1
- Wang H. F., et al., 2020, *MNRAS*, **491**, 2104
- Wegg C., Gerhard O., 2013, *MNRAS*, **435**, 1874
- Wegg C., Gerhard O., Portail M., 2015, *MNRAS*, **450**, 4050
- Weinberg M. D., 1994, *ApJ*, **420**, 597
- Widmark A., Widrow L. M., Naik A., 2022, *A&A*, **668**, A95
- Widrow L. M., Dubinski J., 2005, *ApJ*, **631**, 838
- Widrow L. M., Pym B., Dubinski J., 2008, *ApJ*, **679**, 1239
- Widrow L. M., Gardner S., Yanny B., Dodelson S., Chen H.-Y., 2012, *ApJ*, **750**, L41
- Widrow L. M., Barber J., Chequers M. H., Cheng E., 2014, *MNRAS*, **440**, 1971
- Willett K. W., et al., 2013, *MNRAS*, **435**, 2835
- Williams M. E. K., et al., 2013, *MNRAS*, **436**, 101
- Yamada Y., Gouda N., Yoshioka S., 2015, in IAU General Assembly. p. 2254099